Steady and Unsteady Maneuvering Forces and Moments on Slender Bodies

Kenneth Granlund

Dissertation submitted to the faculty of the

Virginia Polytechnic Institute and State University

in partial fulfillment of the requirements for the degree of

Doctor of Philosophy in

Aerospace Engineering

Dr. Roger L. Simpson (Chair)

Dr. William J. Devenport

Dr. William H. Mason

Dr. Leigh S. McCue

Dr. Craig A. Woolsey

February 6, 2009

Steady and Unsteady Maneuvering Forces and Moments on Slender Bodies

Kenneth Granlund

(ABSTRACT)

Forces and moments have been measured on slender bodies in both static angle conditions as well as rapid time-dependent large amplitude maneuvers with the Dynamic Pitch Plunge Roll (DyPPiR) apparatus.

Lateral and transversal forces as well as all three moments have been measured at $Re_L = 4.5 \cdot 10^6 - 6 \cdot 10^6$ at static angles of attack and sideslip $-26° < [\alpha, \beta] < +26°$ or $-0.45 < [w', v'] < 0.45$ and unsteady pitch ramp maneuvers $-15° \rightarrow 0°$, $-15° \rightarrow +15°$ and $0° \rightarrow 15°$ at a fixed point of rotation at the quarter length of the body. The two bodies are the DARPA Suboff generic submarine shape and a non-Body-of-Revolution scalene ellipsoid with a constant cross-section midbody.

An analytical two-mode equation has been shown to accurately describe the normal force and pitch moment as well as side force and yaw moment for the ellipsoid body. It is based on the observation that the center of pressure for the cross-flow contribution is at a fixed location. For the Suboff body, this assumption is invalid.

Unsteady forces and moments can be measured to a very small magnitude of uncertainty and were found to differ from steady forces and moments at the time-instantaneous flow angle during the motion.

Contents

List of Figures

All figures and images not referenced are copyright of the author.

List of Tables

Nomenclature

α	Angle of attack
β	Angle of drift
η	Correction factor for cross-flow drag over finite cylinders
	compared to infinite cylinders
ν	Fluid kinematic viscosity
ψ	Roll angle of body in x-axis
ξ	Mass fraction of fiber to epoxy resin in composite structure
ζ	Non-dimensional length variable from bow to stern
$a_{1,yz}$	Calibration constant of loadcell 1 in local y_l-axis when loading z_l-axis
$b_{2,yz}$	Sensitivity of loadcell 2 in local y_l-axis when measuring voltage on z_l-axis
$c_{d,c}$	Cross-flow sectional drag coefficient
f_s	Sampling frequency
g	Gravity
l	Distance between loadcells and moment reference point
m	Model mass in kg
$p', q', r' = p, q, r(\frac{L}{U_\infty})$	Non-dimensional rotational velocity in x, y, z direction respectively
q_∞	Dynamic pressure
$t' = t\frac{U_\infty}{L}$	Non-dimensional time

$u', v', w' = u, v, w(\frac{1}{U_\infty})$	Non-dimensional velocity in x, y and z direction respectively
x, y, z	Body fixed coordinate system
y_l, z_l	Loadcell local coordinate system
$Aff1$	Suboff without sail or appendages
$Aff2$	Suboff with sail but witout appendages
$Aff8$	Suboff with sail and stern appendages
$K', M', N' = K, M, N\left(\frac{1}{q_\infty L^3}\right)$	Aerodynamic moment in in x, y, z direction respectively
L	Length of model
R	Radius of model
Re_c	Cross-flow Reynolds number
Re_L	Reynolds number based on length
S	Base area for separated flow in potential calculations
U_∞	Freestream velocity
$V_{1,y}$	Voltage output from loadcell 1 in local y_l-axis
$X', Y', Z' = X, Y, Z\left(\frac{1}{q_\infty L^2}\right)$	Aerodynamic force in in x, y, z direction respectively

Chapter 1

Introduction

For at least a century, engineers have had a desire to predict the motions of vehicles: aircraft, automobiles, airships, submarines, surface ships etc. to build faster, more agile, more stable, more comfortable and in general be able to fully understand what physical phenomena for the vehicle itself, as well as the medium it travels on or in, contribute to the maneuvering behavior. Researchers and engineers have always sought to expand the safe envelope of motion and maneuvering, as well as maintain a capability to an ever decreasing cost. In order to design and construct vehicles for a specific maneuvering goal, one must first be able to analytically, uniformly describe any motion such that it is understood by the community of researchers and engineers in that field.

In order to reliably make predictions on the capabilities of future vehicles, the computational tools themselves must be able to consistently make valid enough predictions about the tested geometries, both in constant motion as well as up to the predicted capability in maneuvering speed of the projected vehicle. In order to validate the computational tools, experiments must be performed as close to the actual maneuvering conditions of the vehicles.

The experiments that provide the foundation for this dissertation will be used to validate computations on new submarine geometries, as well as to give some insight on how these geometries behave in maneuvers.

1.1   Coordinate system definition

A vehicle motion can be described with three translations and three rotations of the body-fixed coordinate system with respect to the inertial coordinate system. This is referred to as a six degree of freedom motion. A right handed coordinate system can be oriented in essentially any way in a vehicle, although there are certain uniformly accepted orientations depending on whether the vehicle is an aircraft, automobile, surface ship, satellite or submarine. For submarines, in this case, the convention by Feldman [26] is used, where the x-axis is oriented forward, the y-axis is oriented in the starboard direction (or right side) and the z-axis is oriented downward as shown in Figure 1.1. The origin of the coordinate system is on the longitudinal line of symmetry and on the lengthwise position where the center of buoyancy is located.
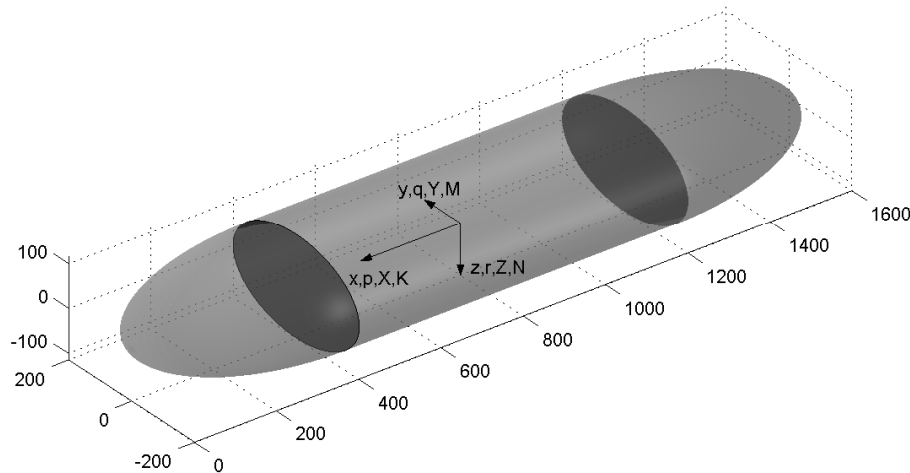
Figure 1.1: Model coordinate system

1.2 Vehicle motion

Any motion of the vehicle is described as a motion of the body-fixed coordinate system with respect to the inertial coordinate system. Translation of the body-fixed coordinate system is described with the velocities u, v and w in the x, y and z directions, respectively. Rotation of the body-fixed coordinate system is described with the rotational velocities p, q and r, respectively.

For vehicles with a forward motion velocity much higher than the two other translational velocities, the six states are usually reduced to five by taking the freestream velocity U_∞ as constant and using two angles alpha α and beta β to describe the translational states. This is normally done for heavier-than-air vehicles such as airplanes which require a significant forward velocity to stay airborne. However, this assumes that the free-stream velocity stays constant. For large amplitude maneuvering, the free-stream velocity may not stay constant [63] and for maneuvers such as the famous 'Cobra maneuver' usually performed with the Sukhoi Su-27 as an agility demonstration during airshows, the purpose is to rapidly pitch the aircraft up more than 90° from level flight and back while significantly reducing forward velocity without losing altitude [74].

To properly define the motion of a vehicle with respect to an inertial coordinate system, one must also take into account any translational and rotational motion of the surrounding fluid with respect to the inertial coordinate system. In the following discussion of motion and maneuvering, the fluid is considered to have no relative motion to the inertial coordinate system.

1.3 Forces and moments

All external forces and moments from the surrounding fluid on the vehicle are denoted X, Y and Z for the forces and K, M and N moments in the x, y and z directions respectively. These definitions are used in naval engineering. A slightly different notation is used in aeronautical engineering, where the force D is used for the aerodynamic drag and L is used for lift.

1.4 Equations of motion

The external forces and moments from the surrounding fluid at every instant in time balance the internal inertial forces and moments as in the equations of motion 1.1 for a simple symmetric body where the center of buoyancy and mass coincide and are aligned at the intersection of the longitudinal- lateral and transversal plane of symmetries.

$$
\begin{bmatrix}
m_B & 0 & 0 & 0 & 0 & 0 \\
0 & m_B & 0 & 0 & 0 & 0 \\
0 & 0 & m_B & 0 & 0 & 0 \\
0 & 0 & 0 & I_{xx} & 0 & 0 \\
0 & 0 & 0 & 0 & I_{yy} & 0 \\
0 & 0 & 0 & 0 & 0 & I_{zz}
\end{bmatrix}
\begin{bmatrix}
\dot{u} \\ \dot{v} \\ \dot{w} \\ \dot{p} \\ \dot{q} \\ \dot{r}
\end{bmatrix}
=
\begin{bmatrix}
X \\ Y \\ Z \\ K \\ M \\ N
\end{bmatrix}
\tag{1.1}
$$

In the body coordinate system, the forces and moments in the three axes are the independent variables and the translations and rotations, also called the states, are the dependent variables. To relate the dependent forces and moments to the independent states, a first-order Taylor expansion was initiated by Bryan [10] with the assumption that all forces and moments are dependent on all states. For example, the normal force Z' and pitching moment

4

M', for any motion constrained in the vertical plane with w' and q', would be expanded as

$$Z' = Z'_{q'}q' + Z'_{w'}w' \tag{1.2}$$

$$M' = M'_{q'}q' + M'_{w'}w' \tag{1.3}$$

As advances to maneuverability of the vehicles progressed, linear dependence of forces and moments to the states were no longer adequate, but extended to include nonlinear dependencies of states, such as higher order terms and cross–dependencies.

The sensitivity coefficients in these equations are normally given as constants from a look-up table in a particular steady-state motion such as a straight and level motion or a constant banking turn. The partial derivatives depending on translational motions are easy to obtain from measurements with the body at an angle of attack α or sideslip β in a wind tunnel. The other derivatives depending on rotational motions are a bit more troublesome to obtain because of the need to achieve constant curvilinear motion. The early experiments were done in vertical wind tunnels dedicated for analyzing spin-motion of aircraft. Later experimental studies have in the past been done with curved or rolling test sections in wind tunnels such as described by Lutze [54]. Present technology for hydrodynamic testing is a rotating arm in a large basin as described by Feldman [27]. Another approach is by Chang and Purtell [12] who conducted an experimental conformal mapping approach by transforming the problem of a curved flow over a straight body to a curved body in uniform flow. This novel approach is not practical since several unique wind tunnel models with different curvature need to be constructed for a single geometry.

1.5 Characterising motion of vehicles

Vehicle motion can be characterized into four different categories

Steady(-state) motion In this case, the vehicle is undergoing a motion where all state variables are held constant and the macroscopic flow behavior is independent of time. Examples of this would be a straight and level flight of an aircraft at some altitude with an angle of attack. Another example could be a constant turn where the vehicle keeps a constant yaw rate, sideslip and angle of attack in order to continue a path forming a circle.

Quasi-steady motion Here, a vehicle is undergoing a time-dependent motion but the states are varying so slowly that the forces and moments depending on the state derivatives are much smaller than those depending on the states themselves. Because of the much smaller contribution, the unsteady terms are neglected. The forces and moments are thus only seen as dependent on the instantaneous states. An example would be the relatively slow 'short-period' and 'phugoid' motions of aircraft in straight and level flight according to Etkin [23]. Regular maneuvering of commercial aircraft, such as take-off, landing and direction change, also falls into this category.

Unsteady motion In unsteady motions of vehicles, a full account is needed for the instantaneous motion of the vehicle with respect to all states and all orders of state derivatives. Some dependencies can be simplified, linearized or neglected depending on the vehicle and the motion. For vehicles that depend on the surrounding fluid for maneuvering such as aircraft and underwater vehicles, the vorticity generated at an instant in time is convected downstream. For subsonic flow, flow property information from the downstream convected fluid is transferred back upstream. Therefore the past history of the motion of the vehicle is needed to determine the instantaneous states

of the vehicle. What complicates things are that vorticity generated in the boundary layer and shed into the freestream convects with significantly different magnitudes of velocity in the inner part and outer part of the boundary layer, as well as outside of the boundary layer.

Quasi-unsteady motion Although not a formally adopted definition in vehicle dynamics, this is defined by the author as a special case of unsteady motion where the motion is oscillatory and therefore periodic. The unsteady aerodynamic states are defined with the motion frequency and amplitude to have instantaneous unsteady properties with the implicit assumption of a time history effect from the periodic motion. A well studied case is modeling the aerodynamics of a rotating helicopter blade. In experiments the airfoil is usually undergoing a pitch-oscillating motion in freestream flow.

1.6   Slender bodies

Investigations in the aerodynamics and maneuvering of slender bodies started with the introduction of airships in the 1920s. Munk [61] summarizes the knowledge on potential flow on rectilinear and curvilinear motion for small angles as well as the use of 'apparent added mass' to predict gust response. Munk concludes that potential flow theory is adequate for predicting forces but overpredicts moments compared to wind tunnel tests, even at small angles. Munk addresses the fact that real viscous fluid produces vortices at the rear of the body that increase local lift and decrease the unstable moment [62]. Potential flow calculations were also used to predict surface pressure forces concerning airship hull structural rigidity concerns. Upson and Klikoff [80] showed that the discrepancy of the calculated pitching moment from Munk's theory to measured moment was due to the bluntness of the bow, thereby locally invalidating the small disturbance assumption.

The discrepancy of normal force and pitching moment at larger angles was recognized by Munk and Upson and Klikoff as viscous contributions. When a slender body is at an angle to the free stream flow, the boundary layer is subjected to a favorable pressure gradient by being accelerated over the blunt bow from the stagnation point. At some location further downstream, the body starts to taper off and the boundary layer will be subjected to an adverse pressure gradient when slowing down. If the adverse pressure gradient is large enough, the boundary layer will separate.

For a circle in 2D uniform flow, the separation location will cause a stagnation point on the surface where there will be a recirculation region on the downstream side. For the case of a cylinder in 3D flow at moderate angles just large enough to cause separation, the boundary layer will still have a predominantly axial flow component that feeds momentum in on the lee side of the separation side such that there will be no stagnation location and also no recirculation region. The flow topology phenomena is called an 'open separation' and is characterized by the boundary layer flow on the lee side, coming from over the centerline part of the bow, is forced outward towards the separation location. The boundary layer fluid is ejected into the outer layer fluid, transported further downstream on the lee side and then back down towards the surface to fill in for the loss in centerline flow further upstream of the body. As the process continues downstream of the body, more fluid will be circulated and transported downstream such as it will be rolled up into a large vortex, one on each side on the lee part of the body and also counter-rotating with respect to each other.

The problem was simplified by Allen [4] by dividing the flow over a slender body at an angle of attack into axial- and transversal components based on the idea of Jones [51] for infinitely long cylinders in oblique flow. Allen made the assumption that the cross-flow velocity

$$w = U_\infty sin\alpha \tag{1.4}$$

could be used to calculate a cross-flow drag (or normal force) component over a circular cross-section

$$Z = 2Rc_{d,c}q_\infty sin^2\alpha \tag{1.5}$$

with the cross-flow drag coefficient $c_{d,c}$ for a cylinder at the cross-flow Reynolds number

$$Re_c = \frac{2RU_\infty sin\alpha}{\nu} \tag{1.6}$$

with a later correction η for finite cylinders. The normal force could then be written as

$$Z = 2R\eta c_{d,c}q_\infty sin^2\alpha = 2R\eta c_{d,c}q_\infty w'|w'| \tag{1.7}$$

for which the normal force has a quadratic dependency on angle of attack. This is essentially the form of equations defined as 'Standard Submarine Equations' by Gertler and Hagen [29]. They were later revised and extended by Feldman [26] by introducing several other higher order states and corresponding coefficients, although without any clear reference to any physical basis in flow structures. The main issue with this form of equations and the underlying physics is the assumption of superposition of solutions from axial and lateral flow components, especially at very small angles of attack – an assumption that was disputed by McCroskey [57]. Equation 1.7 explains the cross-flow velocity component producing a force that is affected by the Reynolds number based on the cross-flow velocity Re_c. A small angle

of attack would therefore have a small Re_c, indicating laminar boundary layer separation and a large cross-flow drag force coefficient $c_{d,c}$. A larger angle of attack would have a larger cross-flow Re_c indicating a turbulent boundary layer and a smaller cross-flow drag-force coefficient $c_{d,c}$. However, if the free stream Reynolds number Re_L for a slender body is large enough for the boundary layer over the mid- and aft body to always be turbulent, it will obviously not undergo any laminar cross-flow separation at small angles of attack and turbulent cross-flow separation at larger angles of attack. At an infinitesimal angle of attack the boundary layer will be subjected to an infinitesimally small circumferential adverse pressure gradient. This infinitesimally small adverse pressure gradient may not undergo separation until the angle of attack has reached some value to produce an adverse pressure gradient large enough to cause separation. Turbulent boundary layers also resist separation in adverse pressure gradients to a greater extent than laminar boundary layers.

In order to characterize the separation location topology, Wetzel et al. [84] used several different methods for quantifying the separation line position and concluded that a minima in skin friction is the best method. Experiments on a 6:1 prolate spheroid by Chesnakas and Simpson [13] as well as Wetzel and Simpson [83] were conducted to reveal the location of the cross-flow separation lines, as well as giving detailed statistical information on the turbulent flow structures in the boundary layer and the large rolled up vortices on the lee side to aid and validate computational simulations. Hosder and Simpson [49] also provided skin friction and separation location information on the Suboff geometry using unidirectional hotfilm sensors. In the aforementioned research on separation location and flow structures, a measurable difference was observed between different pitch rotation maneuvers and the corresponding steady angle of attack conditions. The flow stays attached for some measurable time longer than what a time-instantaneous steady-state solution would predict. Hosder and Simpson successfully applied a first-order lag-model adapted from Goman and Khrabrov [40] to local

separation location, but it is unclear whether this information can be used for maneuvering force and moment predictions as well.

For slender body geometries with a non-1:1 cross section aspect ratio the studies of the flow over the elliptic forebody by Schmitt and Chanetz [70] and Chanetz and Délery [11] provided extensive information on the boundary layer and the vortical separation region with oilflows, LDV and five-hole pressure probe measurements. However, no force measurements were done.

1.6.1 Computational simulations

To address the shed vorticity on slender bodies at higher angles of attack, computational predictions were performed by Mendenhall and Lesieutre [58] as potential flow calculations with added vortex shedding at the location of separation. Despite the quite accurate predictions on submarine maneuvering by Mendenhall and Perkins [59], a priori information on the location of cross-flow separation is needed which precludes it from being an initial tool in submarine engineering.

Recent CFD calculations have been produced from several different research groups, such as the U-RANS simulation of the forces and moments on a pitching 6:1 prolate spheroid by Rhee and Hino [67], maneuvering predictions of a prototype submarine by Racine and Paterson [66], and the LES investigation of the turbulent boundary layer flow of a maneuvering Suboff by Alin et al. [22]. Rhee and Hino used a simple eddy viscosity turbulence model on a relatively coarse grid and concluded that the computations show the correct trend of the data, both in magnitude and time-lag, but that viscous dissipation in the vortical wake is overpredicted and therefore underpredicts all results. Racine and Paterson used overset

grids and a more advanced turbulence model with partial success to predict hydrodynamic coefficients and motion stability of a prototype submarine. The work by Alin et al., has been concentrated on developing computational methods for accurately predicting the turbulent boundary layer and vortical wake structures rather than the implicit method of adjusting the equations to obtain the correct forces and moments. Physical models for the flow are still needed for validation of simulations on these slender bodies - especially unsteady maneuvers. In strong cross-flow separations there is little correlation between the flow-gradient angle and shear-stress angle within the turbulent shear flow, as reported by Chesnakas and Simpson [13], meaning that simple boundary layer models based on eddy-viscosity do not work very well there. Advances in dynamic performance can be made if the complex turbulent separation flow phenomena can be understood, modeled and then included in the design process of future underwater vehicles.

A present, there are no computers fast enough to predict maneuvering in real time from a full flow high fidelity solution over a submarine. To do that, one must use a reduced order six degree-of-freedom model based on state derivative coefficients. Automatic vehicle control systems can take advantage of the increased information from reduced order unsteady aerodynamic models to achieve higher maneuverability. Real-time motion simulators can also achieve higher fidelity. Still, there is no clear consensus on how to treat and predict unsteady motions of either aircraft, surface ships and submarines with reduced order models.

1.7 Analytical models for unsteady motions

Unsteady fluid mechanics phenomena started with analyzing neutrally buoyant vehicles such as airships and submarines with extending the Taylor expansion of forces and moments in Equations 1.2 and 1.3 by also including the partial derivatives of forces and moments with

respect to the different state derivatives as in Equations 1.5 and 1.6.

$$Z' = Z'_{q'}q' + Z'_{w'}w' + Z'_{\dot{q}'}\dot{q}' + Z'_{\dot{w}'}\dot{w}' \tag{1.8}$$

$$M' = M'_{q'}q' + M'_{w'}w' + M'_{\dot{q}'}\dot{q}' + M'_{\dot{w}'}\dot{w}' \tag{1.9}$$

Forces due to the change in displaced fluid around the body from translational and rotational motions are named 'added mass' and 'added inertia' terms. These have historically been calculated with inviscid assumptions since the vehicles in application have been slender, such as airships and submarines, the motions have usually been very close to straight and level and the perturbations from the initial motions have been small. With these assumptions, these force terms are linearly dependent on the transversal and rotational accelerations. Because of this, the resulting forces and moments are shifted to appear as additional terms in the system matrix from Equation 1.1 to be the new system matrix shown in Equation 1.10. Hence the name – '(apparent) added mass' and '(apparent) added inertia'.

$$\begin{bmatrix} m_B - X_{\dot{u}} & 0 & 0 & 0 & 0 & 0 \\ 0 & m_B - Y_{\dot{v}} & 0 & 0 & 0 & -Y_{\dot{r}} \\ 0 & 0 & m_B - Z_{\dot{w}} & 0 & -Z_{\dot{q}} & 0 \\ 0 & 0 & 0 & I_{xx} - K_{\dot{p}} & 0 & 0 \\ 0 & 0 & -M_{\dot{w}} & 0 & I_{yy} - M_{\dot{q}} & 0 \\ 0 & -N_{\dot{v}} & 0 & 0 & 0 & I_{zz} - N_{\dot{r}} \end{bmatrix} \tag{1.10}$$

One issue with this approach is that it assumes that the 'added mass' and 'added inertia' terms are assumed to be constant. Slender bodies at large angles of attack and sideslip produce lift with large lengthwise vortices on the leeward side. Even with the inviscid theory that lies behind the original assumption of added mass and inertia one can quickly

13

reason that, with a similar calculation for the lift-producing body, the added mass and inertia for that state would not necessarily give the same answer as for the straight and level case. Therefore, added mass and inertia can depend on the states of the slender body. A qualitative analysis is still possible by adding vortices to strip theory calculations. From global flowfield knowledge, or separation location information, one can draw qualitative conclusions on how added mass and inertia vary with crossflow from sideslip or angle of attack as shown by Granlund and Simpson [42]. The analysis can only be used to predict the qualitative behavior of the trend – the fact that the 'added mass' coefficient term is reduced as the cross-flow separation moves more to the lee side at a higher local angle of attack.

1.7.1 Indicial functions

A notable issue with the unsteady added mass and -inertia terms is that they are time-invariant. It is a well known fact that vorticity, generated on the wall in the boundary layer under the action of pressure gradient and viscosity, separates and rolls up in vortices on the lee side and finally convected downstream in the wake. Thus, the flow condition at any instant in time should depend on the entire past history of the flow over the body. This concept of time-history effects was introduced by Tobak [78] as the indicial functions approach by assuming that any unsteady force or moment contribution could be taken as the integral sum of impulse steps of the relevant states.

$$C_L(t) = C_L(\alpha(t=0)) + \int_0^\tau C_{L\alpha}(\tau)\dot{\alpha}(t-\tau)d\tau \tag{1.11}$$

$$C_L(t) = C_L(\alpha(t=0)) + \int_0^\tau F(\alpha(\tau), t=\tau, q=0)\dot{\alpha}(t-\tau)d\tau \tag{1.12}$$

The linear kernel stability derivative in Equation 1.11 was successively extended to nonlinear functions as in Equation 1.12 via different kernels such as described by Klein et.al [64].

$$F_1(\alpha, t) = C_{L\alpha}e^{-b(\alpha)t} \tag{1.13}$$

$$F_2(\alpha, t) = a(\alpha)C_{L\alpha}e^{-b(\alpha)t} \tag{1.14}$$

$$F_1(\alpha, t) = C_{L\alpha}e^{\int_\tau^t(-c(\alpha(\zeta))d\zeta} \tag{1.15}$$

$$C_{L\alpha} = d_1 + d_2(\alpha - \alpha_1) + d_3(\alpha - \alpha_1)^2 \tag{1.16}$$

There are several problems with this approach. The first is the increasing complexity of the kernel with more and more constants to determine, some of them possibly even with questionable physical meaning. Just because an aerodynamic property can be written as a mathematical function does not necessarily mean that there are any physical phenomena that justify that function. The second one is that the state and kernel function can be represented as a vector and matrix in a linear relationship inside the integral. Whether the indicial function approach even can be extended to a multivariate relationship either in linear or some nonlinear form is questionable. The third objection is whether a single time constant τ can be used to represent all unsteady features of the flow structures, such as delayed separation, vortex burst etc., or if several time constants are needed.

1.7.2   Time-lead/lag equations

Models predicting unsteady dynamics of motion with time lead/lag have proved useful for a number of different experimental studies involving airfoils, delta wings and entire aircraft. These models predict fluid phenomena by using internal state variables. These states are allowed to have time leads or lags showing the behavior of vortex burst and/or separation location off an airfoil that in turn affect the global forces and moments. Goman and

Krabrov [40] used the internal state variable x_v as a monotonic single-variable function to describe the chordwise separation location as a function of angle of attack α.

$$\tau_1 \frac{dx_v}{dt} + x_v = x_{v,0} \left(\alpha - \tau_2 \alpha^*\right) \tag{1.17}$$

$$C_L = C_{L0} + \frac{\partial C_L(x_v)}{\partial \alpha}\alpha + \frac{\partial C_L(x_v)}{\partial \hat{q}}\hat{q} \tag{1.18}$$

$$C_m = C_{m0} + \frac{\partial C_m(x_v)}{\partial \alpha}\alpha + \frac{\partial C_m(x_v)}{\partial \hat{q}}\hat{q} \tag{1.19}$$

Fan and Lutze [24] showed that for an F-18 aircraft model, one can use the non-dimensionalised internal state variable x_v of the vortex burst location and two different time constants with the external state variables for angle of attack α and pitch rate q as in Equation 1.19. The time constants in the differential equation will modify the location of separation or burst location during a maneuver with non-zero state derivatives. The modified location will describe a different lift or pitching moment during an unsteady maneuver from the steady state separation or burst location.

For a slender body, such as a submarine, airship or a torpedo, these fluid phenomena are a bit more complex. As opposed to the leading edge of a delta wing, the separation location is no longer fixed. It also can not be parameterized as a monotonic function of a single variable for chordwise, spanwise or circumferential angle location. The flow exhibits cross-flow separation which can be characterized by a circumferential angle position that varies all along the entire middle and aft portion of the body shown by both Wetzel and Simpson [83] and Hosder and Simpson [49]. For example, when maneuvering in pitch and/or heave, the separation location would most likely not change uniformly across the entire lee side. The vortex burst phenomena also does not occur within any normal maneuvering envelope for slender bodies in use today.

1.7.3   Previous experiments

Previous work has mainly focused on sharp edge separation from airfoils, delta wings and also coned forebodies of missiles. Blunt-nosed slender bodies have more complex flow phenomena since the separation on the leeward side is three-dimensional [13] and the location is also not fixed.

The early attempts to determine unsteady effects were done with coning motion rigs such as the work by Tobak and Schiff [79] and Ericsson [21]. These experiments consisted of oscillations in no less than five state variables - α, β, p, q and r. Smith and Nunn [75] reduced the variations to two states by oscillating in one plane, but they were still continuously variable during one motion test. The difficulties in constructing analytical models for these unsteady motions are tremendous since the unsteady contributions from the different state variables are difficult, if not impossible to separate out.

Subsequent research were small amplitude oscillation in one plane - either in pitch-, yaw- or roll plane using constrained oscillatory motion devices. Small amplitude oscillation were performed at some nominal angle of attack and/or sideslip to give some information on dynamic state derivative coefficients. The phenomena of delta wing vortex breakdown were investigated with pitch oscillation and roll oscillation at angle of attack. The unsteady pitch oscillation of a NACA 0015 airfoil was investigated by Goman and Khrabrov [40] in an attempt to extend the knowledge of helicopter blade aerodynamics. Greenwell [44], also extended the model to include the delay in vortical separation from delta wings. The time lag concept has been extended to several other geometries such as complete aircraft such as vortex burst causing wing drop on the F-18 by Fan and Lutze [24]. A thorough review of recent unsteady aerodynamic modeling has been done by Greenwell [45].

During the 1990s, investigations in so called 'super maneuverability' of combat aircraft were conducted after the analysis of the Su-27 'Cobra maneuver' [74]. These air combat maneuvers performed were characterized by rapid, short-duration changes in aircraft direction at lower speeds. Research in analytically investigating these post-critical angles of attack at high pitch rates has been conducted as bifurcation analysis such as the work by Sibilski [72]. However, to accurately be able to predict maneuvering dynamics of vehicles, one needs to have an accurate analytical representation of the physics of the problem. According to Nelson and Pelletier [63], bifurcations only arise when the flow structure changes modes, such as the onset of a separation or vortex burst. Time lags also only occur from bifurcations. In the scope of this research, only the flow physics matters. For other aeronautical problems, such as aeroelastcity, the aerodynamic interaction with structure deformation is of interest.

One problem persists though - most experiments done in previous research are either small amplitude oscillations in one or more state variables or large amplitude in only one state variable. McCroskey [57] raised the point that it is debatable whether these single-state variable small amplitude oscillations can be extended via superposition to multi-state large amplitude motions that are more similar to actual operational maneuvers. The problem with the oscillatory tests are that the wake of convected vorticity generated from the oscillatory motion influences the flowfield over the body, and therefore the pressure distribution and forces and moments at any instant in time – at least in subsonic flow. This makes oscillatory tests 'quasi-unsteady' in the respect that they are attributed properties of a time–dependent unsteady motion whereas the motion is instead continuously repeatable. For this reason, model oscillation testing should only be used when the real motions of the vehicles themselves are oscillatory.

1.8 This research contribution

This research seeks to extend the knowledge of forces and moments over non-body of revolution slender bodies for fixed angles of attack as well as for unsteady pitch ramp maneuvers. For steady angles of attack, the presence and extent of the linear range from attached flow to the nonlinear range with separated flow will be investigated and quantified for at least two different geometries. Attempts to construct reduced order models will also be made from the experimental data.

Short duration, unsteady pitch-ramp maneuvers will be performed to investigate how, and which different analytical models can be used to predict maneuvering forces and moments from the states of the motion. The unsteady datasets will also be used as a database reference set for non-body of revolution geometries to validate computational flow simulations.

Chapter 2

Equipment

To accurately obtain hydrodynamically similar forces and moments on slender bodies in static and dynamic conditions in air, several pieces of equipment need to meet certain conditions. First, since air is less dense than water, Reynolds number will not be matched but must be kept high enough to invoke similar flow conditions over the model as for a full size vehicle. This implies a large model and high freestream velocity. To achieve dynamic maneuvering similarity a mechanism needs to be able to accurately adjust the position of the model at a similar rate corresponding the rate of fluid passing over the model versus for the real size vehicle. The higher the freestream velocity and the smaller the model, the larger the model maneuvering rate.

The higher the maneuvering rate of the model, the larger the extent of the model mass will affect the measurements. Mass of the model needs to be kept as low as possible while at the same time keeping the model structurally stiff and not deform during maneuvering. Force transducers need to be sensitive only to the inertial- and aerodynamic loads in the desired directions as well as have a long fatigue life.

2.1 Models

Three models are built for wind tunnel tests. They are of similar construction as the Suboff model previously built by Whitfield [85] and used by Granlund and Simpson [43]. To increase the signal-to-noise ratio in dynamic tests, the models need to be as lightweight as possible and lighter than the previously built Suboff model to reduce inertial forces. To accomplish this, the vinyl foam core and aluminum stringers are replaced by Nomex honeycomb. The surface gelcoat from the Suboff model built by Whitfield is also no longer employed. Gelcoat on composite structures such as boats and aircraft is mainly used to protect the fibers and polymer matrix from degrading by ultraviolet radiation from the sun. A secondary purpose is to provide a hard surface that can have a different color than the composite structure. Neither of these properties are necessary for a wind tunnel model since it is stored indoors away from sunlight and is handled carefully to avoid dents while being transported between storage and wind tunnel testing. Surface coloring with red pigment may be a desired property for laser based flow measurements such as DGV, LDV or PIV to avoid surface scatter of laser light to the receiving optics or a black surface for oil flow visualization, but it can be achieved with spray paint after the model is built.

For the ellipsoid model, paper templates for every 2" position of the curved bow and stern are printed out and glued on to 2" thick sheets of extruded polystyrene wall insulation sheets. The sections are then cut out with a scroll saw as shown in Figure 2.1. The constant cross-section midbody part is cut out with a hot-wire saw with wood end templates. The wood templates are constructed the same way as with paper templates glued to the wood boards.

The different sections forming the plug are glued together with 3M Spray Adhesive 6070 [65] and stacked using clamps shown in Figure 2.2. After the stacked slices make up a curved bow

section, they are sanded down, first with a coarse shaving then 120 grit and finally 400 grit sand paper. The sanding pattern is crosswise as in Figure 2.3 in order to avoid producing flat spots. To achieve the correct surface curvature, the plug can be held up and rotated slightly so that it reflects the light. Non-smooth curvatures can easily be spotted in the reflecting light and corrected with the sanding block. After the plug parts have been sanded down to the correct shape, the bow/stern and midbody are glued together. Plugs for other submarine-like models have been CNC machined from polyurethane foam by Vectorworks Marine [1].

The plug is then covered with a thin 4 Oz/Sq Yd. Fiberglass Surfacing Fabric [31] and epoxy [76] to create a hard surface and protect the Styrofoam from the organic solvents of the finishing material. If the plug is machined out of a block of polyurethane foam, there is no need for a fiberglass surface. It is instead prepared with a mix of epoxy and glass microspheres [34] that is applied smoothly over the surface before the surface finishing material. Bondo Automotive Body Filler [8] is applied and sanded down to give a smooth surface with 220 and 400 grit sandpaper. After that, in order to take care of pinhole spots, Bondo Spot Putty [9], shown in Figure 2.5, is applied and sanded down with 800 grit sandpaper. To complete finishing the surface, it is sprayed with automotive filler primer that is sanded down with 800 followed by 1600 grit sandpaper. To complete the surface, several coats of automotive lacquer [20] are applied and sanded down with 1600 grit wet sandpaper.

To prepare for making a mold from the plug it is glued on to a backing board on a flat surface. Gaps between the plug and the backing surface are sealed using an oil-based clay [35] shown in Figure 2.6. Excess clay is removed to get a square edge. The plug and backing board is then waxed four times with a carnauba wax that is suitable for epoxy molds. In order to ease the release of the mold from the plug and backing board, it is spray coated

with a PVA release film [38]. It is essential to cover a substantial part of the backing board with wax and release film to be able to create a mold edge.

The first part of the mold is the epoxy surface coat [33] that is brushed on to the mold shown in Figure 2.7. This surface coat helps provide longevity for the mold surface so that it can be used repeatedly to create several models without degradation. A 10 cm edge on the backing board is applied to create the edge for the mold. The surface coat is also mixed with pigment in order to achieve a contrasting surface for the subsequent layers of fiberglass and epoxy. With a contrasting color, it is easier to see if there are any air bubbles trapped in the epoxy that locally weakens the structure. The second part is four layers of the Surfacing Fabric [31], which are draped over the surface coat when it has started to cure. It is important to wet the fabric thoroughly with epoxy before adding the next layer to avoid voids that will make the mold surface brittle. The third part is a total of eight layers of 20 Oz/Sq Yd. Fiberglass Tooling Fabric [31] to build thickness. Again, it is important to wet each layer with epoxy before adding the next. Finally, add two shaped blocks of 2" Styrofoam sheet to stiffen the mold and to provide a level support. When the epoxy has cured after several hours, the plug can be released from the mold. The mold then needs to be polished inside to a smooth surface since the PVA release film produces an 'orange peel' texture.

When the two model halves are produced, the Hexcel HRH-10-F35-2.5 over expanded honeycomb core [46] used in the center section and HRH-36-F50-2.0 Flexcore [47] for the double curvature surfaces of the bow and stern first needs to be positioned in the mold and cut to the correct shape. Then the two sheets of Fibre Glast 3K 2x2 twill weave carbon fiber fabric [30] are cut. Finally, the vacuum bag [37], Nylon release film [36] and breather cloth [32] are cut to shape. To begin the process, the sealant tape [39] is first attached around the entire outer edge of the mold with the top paper protection still in place. Then the vacuum

bag is positioned in place attached to half the side of the mold. In the vacuum bag, mount one or two hose attachments depending on the mold size. The final preparation of the mold is four coats of waxing and buffing and finally a coat of PVA release film.

The process is started by positioning one layer of carbon fiber fabric in the mold. Epoxy is mixed in a cup-sized batch and then poured on the weave. The liquid needs to be thoroughly worked in to completely wet the fabric by using both a roller and a squeegee. With an excess of epoxy it is easier to completely wet the fabric. The excess epoxy is then removed with squeegee and scraped back up in the mixing cup. When working in the epoxy into the weave, it is relatively easy to shift the weave. The fibers need to be completely straight in order not to weaken the structure. When the fabric is completely wet and all the excess is scraped off, position the honeycomb in the mold and close the vacuum bag. Before completely closing the bag, place a swatch of Nylon release film and a quadruple folded piece of breather cloth underneath each vacuum hose fitting. The breather cloth spreads the load so that the fitting does not deform the honeycomb material. The Nylon release film makes sure that the breather cloth does not get glued to the material with the epoxy. Finally, apply vacuum and check the bag for leaks.

When the epoxy has cured completely, one removes the bag gently in order not to damage it, but leaves half the bag attached to the mold and sealant tape for the second part of the model. Complete the second layer of carbon fiber fabric by completely wetting it with epoxy. Excess epoxy is not a problem since it will be soaked up during curing. This time, use a fully covering layer of Nylon release film and a fully covering layer of breather cloth in order to wick up any excess of epoxy. The layers are shown in Figure 2.10. Also place quadruple folded pieces of breather cloth under the vacuum fittings to avoid soaking up too much epoxy. Complete another vacuum cycle until the epoxy has cured completely. After

the curing cycle, remove the vacuum bag and breather cloth. With the model half still in the mold, apply a mix of epoxy and glass microspheres to the edge and sand it down squarely after curing. Then repeat the entire process for the second half to produce two symmetric halves shown in Figure 2.11. The model geometry uncertainties are kept below $0.5mm$ in order not to affect the measurement uncertainties according to a study by Makovec [55]. No dynamic structural analysis was done on the construction of the models. Since the models have been subjected to much larger accelerations, without permanent damage, by the DyP-PiR than those of the motions where aerodynamic data is obtained, it is believed that any deformations of the model are negligible.

Since a sandwich construction is too weak to transfer point loads to loadcells, rings machined out of 25.4mm thick aluminum block to an inner 3.175mm ring are used to transfer the load. Two rings are used, one at the front most, and one at the rearmost points of the constant cross-section midship part. The aluminum rings are glued with epoxy to the inside of the model. They incorporate mounting points for the two front and single rear loadcells. One half of the model is cut in three pieces in order to create a removable hatch of the mid body section. When the hatch is mounted to the model, clay [35] is used to seal the gaps.
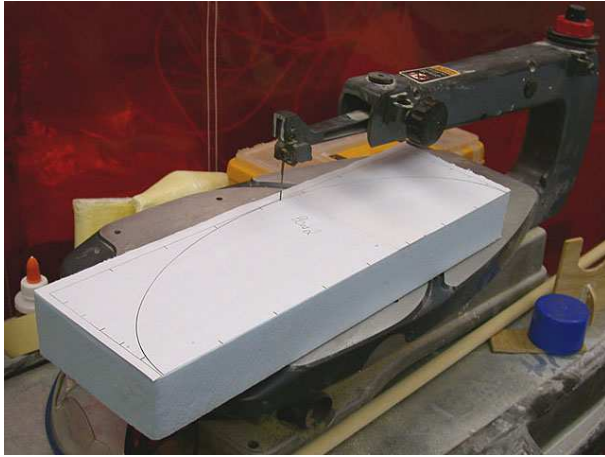
Figure 2.1: Cutting 2" Styrofoam segments

Figure 2.2: Gluing segments together

Figure 2.3: Sanding the curved surface

Figure 2.4: Reinforcing the surface with fiberglass cloth and epoxy

Figure 2.5: Smoothing the surface with spot putty

Figure 2.6: Attaching the plug to a backing surface

Figure 2.7: Waxing the surface glossy

Figure 2.8: Mold epoxy surface coat

Figure 2.9: Layers of fiberglass cloth plus 2" Styrofoam stiffeners

Figure 2.10: Model surface construction

Figure 2.11: Two shell halves created

Figure 2.12: Aluminum ring inserted

2.1.1   Mass and moment of inertia

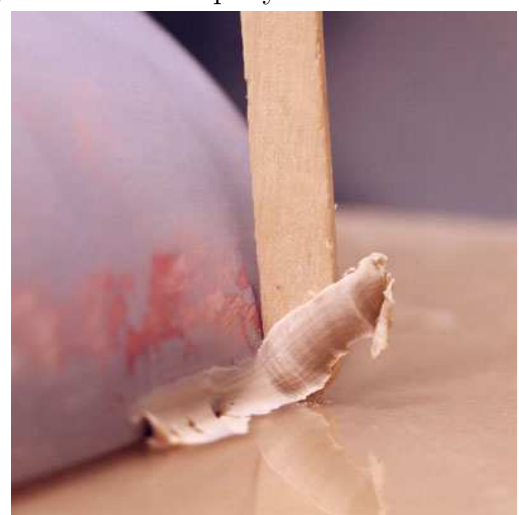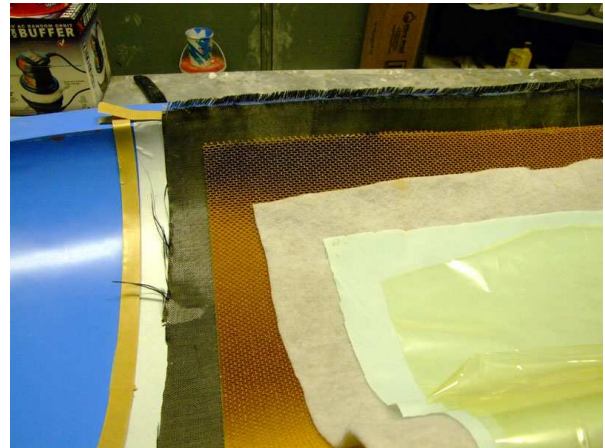The mass and moment of inertia of the models need to be measured or calculated for the inertial loads to be subtracted from the total loads during dynamic tests. Because of the low weight of the model, experiments would need to be performed in vacuum to measure the inertia without including the effects of still air. This is also the reason why dynamic maneuvers cannot be performed as 'wind on maneuver' minus 'wind off maneuver'.

Since the models are built as a sandwich shell structure with thin walls, it is easier to use area density in the calculations. The equations for calculating the mass, center of gravity and moment of inertia are

$$m = \int dm = \rho_a \int dA \tag{2.1}$$

$$x_m = \int x dm \tag{2.2}$$

$$y_m = \int y dm \tag{2.3}$$

$$z_m = \int z dm \tag{2.4}$$

$$I_{xx} = \int \left(y^2 + z^2\right) dm \tag{2.5}$$

$$I_{yy} = \int \left(x^2 + z^2\right) dm \tag{2.6}$$

$$I_{zz} = \int \left(x^2 + y^2\right) dm \tag{2.7}$$

and the area densities for the materials are

$$\rho_{a,weave} = 0.19326 \frac{kg}{m^2}$$

$$\rho_{a,epoxy} = 0.359664 \frac{kg}{m^2}$$

$$\rho_{a,honeycomb} = 0.27057 \frac{kg}{m^2}$$

The area is numerically integrated by summing area elements tangentially round the x-axis and then in x-direction. An area element consists of four defined points on the body.

$$\vec{r}_1(x, \theta)$$

$$\vec{r}_2(x, \theta + d\theta)$$

$$\vec{r}_3(x + dx, \theta)$$

$$\vec{r}_4(x + dx, \theta + d\theta)$$

The mass is calculated at the linear geometric center of the area element

$$\vec{r}_c(x, \theta) = \frac{(\vec{r}_1 + \vec{r}_2 + \vec{r}_3 + \vec{r}_4)}{4} \tag{2.8}$$

The area of the element, shown in Figure 2.13, is calculated as four triangles, each with two corner points and the center point as the third. This enables a more accurate calculation of area of highly skewed elements.
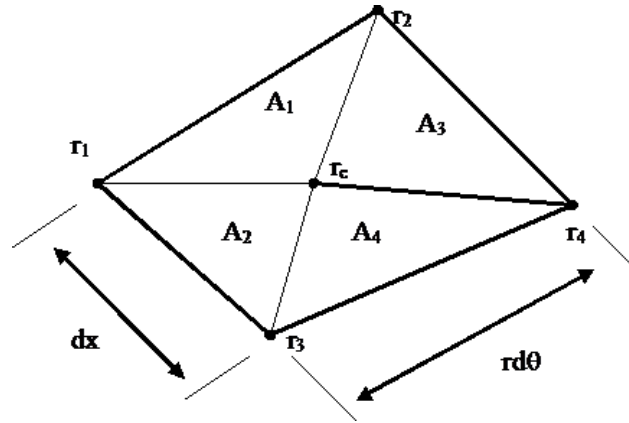

Figure 2.13: Integration area element

29

$$A_1 = \frac{1}{2} abs \left[(\vec{r}_1 - \vec{r}_c)(\vec{r}_2 - \vec{r}_c) \right] \tag{2.9}$$

$$A_1 = \frac{1}{2} abs \left[(\vec{r}_1 - \vec{r}_c)(\vec{r}_3 - \vec{r}_c) \right] \tag{2.10}$$

$$A_1 = \frac{1}{2} abs \left[(\vec{r}_2 - \vec{r}_c)(\vec{r}_4 - \vec{r}_c) \right] \tag{2.11}$$

$$A_1 = \frac{1}{2} abs \left[(\vec{r}_3 - \vec{r}_c)(\vec{r}_4 - \vec{r}_c) \right] \tag{2.12}$$

$$A = A_1 + A_2 + A_3 + A_4 \tag{2.13}$$

Since the body consists of three layers of material, an outer and inner layer of carbon fiber reinforced epoxy, and a middle layer of Nomex honeycomb, the integration is done in three parts, one for each layer. The only unknown, or adjustable parameter, is ξ in calculating the thickness of epoxy in the faces of the shell structure

$$\rho_{a,face} = (\xi \rho_{a,weave} + \rho_{a,epoxy}) \tag{2.14}$$

A grid independence study concludes that for mass to be determined $\leq 1g$ uncertainty for square area elements, dx and $d\theta$ need to be smaller than according to Table 2.1. The weight

dx	$\leq 0.005m$
$d\theta$	$\leq 3°$

Table 2.1: Grid independence requirements

and moment of inertia of the aluminum support rings are calculated in AutoCAD [6]. With the aforementioned conditions and the following calculations, a $\xi = 0.87$ is achieved in the manufacturing process. This means that there is a slight excess of epoxy in the structure.

2.1.2 Suboff

The Suboff geometry, first tested by Roddy [68], is a widely used slender body configurable as unappended, with sail, stern appendages or with both. The exact geometrical shape of the Suboff geometry is included in the Appendix.

Due to an unfortunate event, the Suboff model previously used in tests by Whitfield [85] and Granlund [41] was destroyed. A new model was built with uniform core material that enables the mass properties to be determined. The properties of the aluminum support rings are given in Table 2.2.

m_{ring}	0.3746 kg
I_{xx}	0.00178287 kgm^2
I_{yy}	0.003283 kgm^2
I_{zz}	0.004850 kgm^2

Table 2.2: Suboff aluminum support ring properties

The measured mass of the model with the support rings is $m_{suboff} = 2.749kg$. In the calculations, ξ is adjusted for the calculated weight to match the measured weight of the model shell. The model shell properties are given in Table 2.3.

m_{shell}	1.9992 kg
$x_{m,shell}$	1.0618 m
I_{xx}	0.0300 kgm^2
$I_{zz} = I_{yy}$	2.9401 kgm^2

Table 2.3: Suboff shell properties

The inertial properties of the entire model are calculated at the center of gravity via

$$x_m = \frac{1}{m_{tot}} \left(m_{shell} x_{m,shell} + m_{ring} \left(x_{m,frontring} + x_{m,rearring} \right) \right) \quad (2.15)$$

$$\begin{aligned}
I_{xx,model} &= I_{xx,body} + 2I_{xx,ring} && (2.16) \\
I_{yy,model} = I_{zz,model} &= I_{yy,shell} - m_{shell}x_{m,shell}^2 \\
&\quad + I_{yy,ring} + m_{ring}\left(x_m - 0.5334\right)^2 \\
&\quad + I_{zz,ring} + m_{ring}\left(x_m - 1.70352\right)^2 && (2.17)
\end{aligned}$$

$m_{barebody}$	2.7484 kg
$x_{m,shell}$	1.0772 m
I_{xx}	0.0133 kgm^2
$I_{zz} = I_{yy}$	0.489 kgm^2

Table 2.4: Suboff model mass properties

2.1.3 Ellipsoid body

The ellipsoid is chosen for a generic non-body of revolution shape. The body is similar to the one studied experimentally by Schmitt and Chanetz [70].

$$\left(\frac{x}{a}\right)^2 + \left(\frac{y}{b}\right)^2 + \left(\frac{z}{c}\right)^2 = 1 \tag{2.18}$$

A scalene ellipsoid with $a = 400mm$, $b = 200mm$ and $c = 115.5mm$ axes lengths and $n_1 = n_2 = n_3 = 2$ is used for the bow and stern. An 800mm long constant elliptical cross-section is inserted in the middle of the longest axis. This produces a body, depicted in Figure 2.14 with half the size of the model used by Schmitt and Chanetz. The geometry used in these experiments is more like a submarine-like body, since the aforementioned body by Schmitt and Chanetz was only the front half of the body in this work.
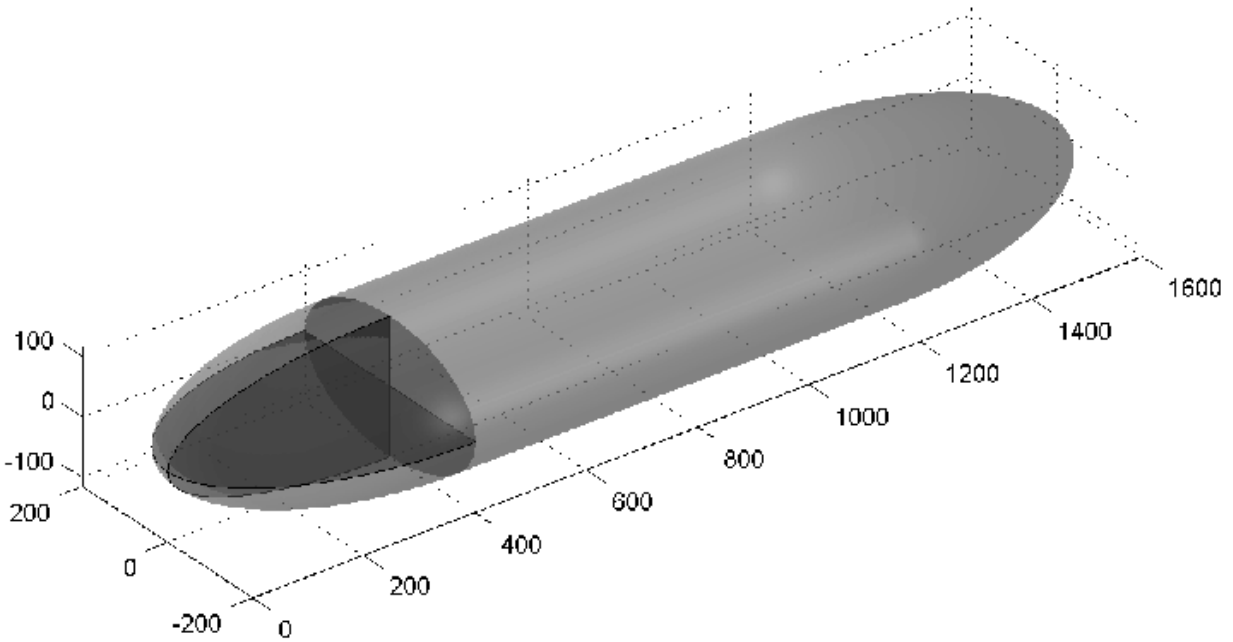
Figure 2.14: Ellipsoid body (dimensions in mm)

The use of elliptic shapes is motivated by the study of separation locations. Elliptic surfaces have no curvature discontinuities, and thus no pressure gradient discontinuities that can promote separation at fixed locations. This should therefore be of a particular challenge to computational simulations.

The inertial properties of the ellipsoid body are computed the same way as for the Sub-off. First the properties of the aluminum support rings are calculated in AutoCAD to the properties in Table 2.5.

	Rear	Front
m_{ring} [kg]	0.411	0.360
I_{xx} [kgm^2]	0.00679	0.00877
I_{yy} [kgm^2]	0.00324	0.0145
I_{zz} [kgm^2]	0.00373	0.0736

Table 2.5: Ellipsoid aluminum support ring properties

With the same ζ ratio as for the Suboff, the calculated mass of the ellipsoid body agrees within 5 grams of the measured mass. The ellipsoid model has the mass properties in Table 2.6.

$m_{ellipsoid}$	2.5636 kg
$x_{m,shell}$	0.8061 m
I_{xx}	0.0301 kgm^2
I_{yy}	0.227 kgm^2
I_{zz}	0.265 kgm^2

Table 2.6: Ellipsoid model properties for $x/L = 0.5$

2.1.4 NNEMO

The Newport News Experimental MOdel is a concept design model for a new submarine. It is a twin propulsor design with roughly 1:2:6 height:width:length ratio, thus also making it a non-body of revolution. The actual geometry is ITAR restricted and thus cannot be published openly. The scaled wind tunnel model is built to a length of 2.43m. The model has the following inertial properties for $\frac{x_{rp}}{L} = 0.5$

$m_{barebody}$	0.0 kg
$\zeta_{m,shell}$	0.0 m
I_{xx}	0.057 kgm^2
I_{yy}	0.299 kgm^2
I_{zz}	0.3026 kgm^2

Table 2.7: NNemo model mass properties

2.1.5 Boundary layer trips

For the wind tunnel model to simulate the flow conditions over a large full-scale submarine, the Reynolds number ideally needs to be the same. Even though on a full scale submarine $Re_L \approx 10^9$ it is not achievable in a wind tunnel, the main concern is still that the boundary layer is fully turbulent before cross-flow separation on the lee side. This is ensured with trips on the bow. According to Ahn and Simpson [2], there exists a critical Reynolds number of $Re_L \approx 2.5 \cdot 10^6$ for the 6:1 prolate spheroid with the post trips where the boundary layer will be turbulent at cross-flow separation. Above this Reynolds number, the separation topology dependence on Reynolds number is small compared to the dependence on angle of attack.

The location of the trips is taken from the study by Fussell and Simpson [28] and De-Moss [16]. Essentially, there are criteria that need to be fulfilled. First, the trips need to be in a location downstream enough to produce a momentum thickness change of $\Delta Re_\theta > 800$ so that flow relaminarization cannot occur at any angular portion to the flow within the test range. Second, they need to be in a location upstream enough where the boundary layer is not subjected to an adverse pressure gradient, when in any test angular position. This is taken as the location where the tangent to the surface is parallel to the freestream for all orientations of the model. For all three bodies; the ellipsoid, NNEMO and Suboff, the location is $x/L = 0.05$ as shown in Figure 2.15.

The trips are two rows of 1.6 mm (1/16") diameter cylinders with a height of 1.14 mm (0.045") with 4.75 mm (3/16") separation shown in Figure 2.16. Eight layers of masking tape with 1/16" hole punch are used as a disposable mold for a mix of epoxy and microballoons to create the trips directly on the surface on the model.

Figure 2.15: Boundary layer trip location on the model bow

Figure 2.16: Boundary layer trips

2.2 Wind tunnel

The experiments are performed in the Stability Wind Tunnel at Virginia Tech which is a closed return, subsonic facility with provision for installing different types of test sections. The test section is a 1.8m x 1.8m cross section with 7.3m length. The maximum speed is 45m/s with the DyPPiR installed. Free stream turbulence is $< 0.03\%$ according to Choi and Simpson [14].
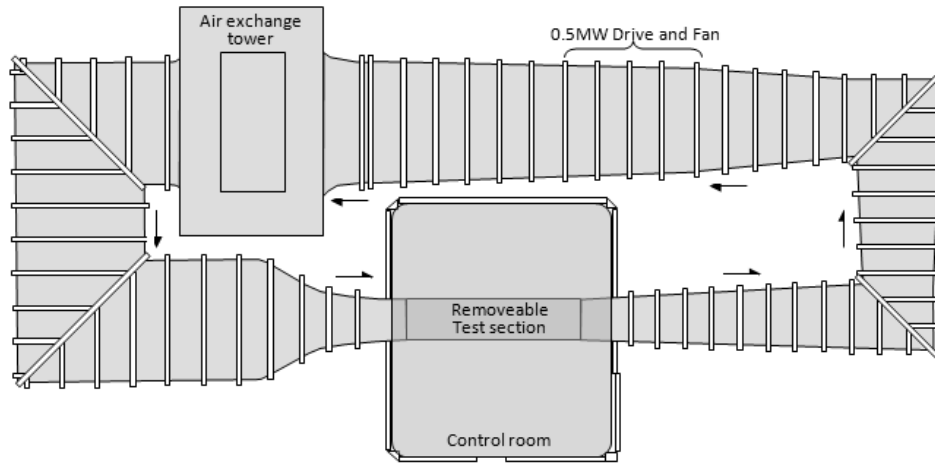

Figure 2.17: Stability Wind Tunnel schematic (from [77])

Slotted walls were used in the tests to reduce the blockage effects of large wind tunnel models. A study done by Willet [86] concluded an optimum open air ratio is 37.4%. This is achieved with installing lengthwise boards on all walls as shown in Figure 2.19 and also in the motion video analysis in Section 4.3. The boards are 25mm thick 'oriented strand board'. Three center boards have a width of 150mm and the four outer on each side are 75mm slats. The spacing between each slat is 75mm. Whitfield [85] and Granlund [41] concluded that the forces and moments measured on the Suboff are within the uncertainties measured by Roddy [68]. No studies have been done on whether there are any dynamic blockage effects on the model during maneuvers.
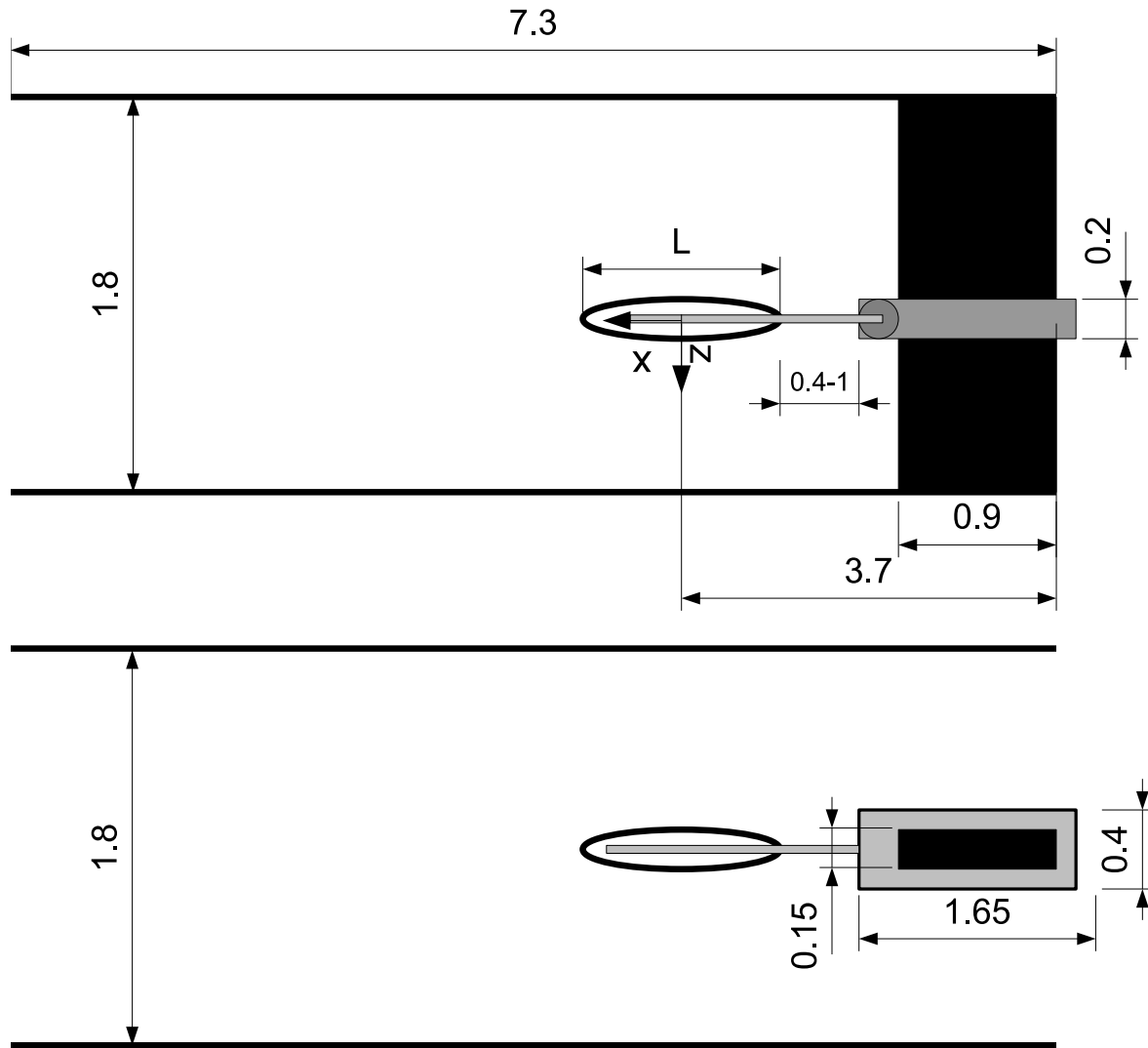
Figure 2.18: Test section with DyPPiR and model installed (dimensions in meter)
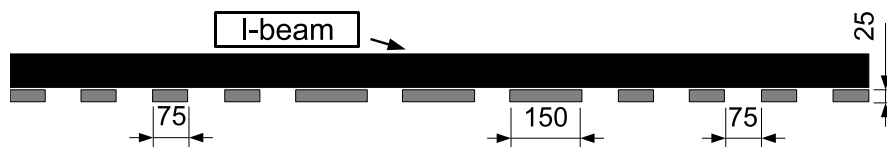

Figure 2.19: Slotted wall schematic of upstream/downstream view (dimensions in mm)

The dynamic pressure fluctuations reported by Larssen and Devenport [53] and further investigated by Granlund [41] have been addressed since they can promote or delay the onset of separation on the body. During the Ellipsoid drag measurements by DeMoss [16], an attempt was made to remove the fluctuations by suction via a high-capacity air blower and an upstream facing 30 cm tube inserted in the diffuser. Unfortunately, this produced no change whatsoever on the pressure fluctuations. Reversing the tube and blowing in air had no effect on the fluctuations either.
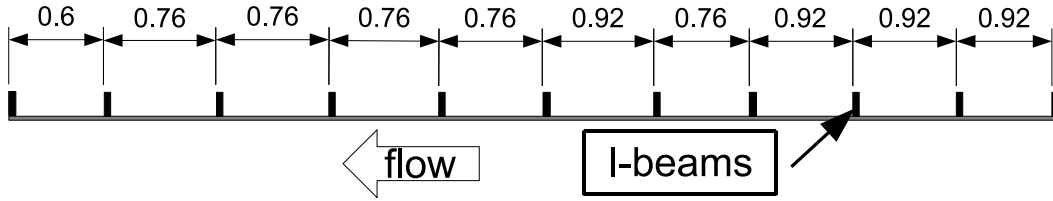

Figure 2.20: Slotted wall beam side schematic (dimensions in meter)

A further investigation revealed that the wavelength λ computed from dividing the free stream velocity by the measured Pitot tube pressure fluctuation frequency by Granlund [41] coincided reasonably well with twice the distance between test section wall panel support I-beams. By adding support boards mounted on the outside of the slats between the I-beams, the amplitude of the fluctuations appeared to be reduced, although this effect was never quantified with measurement equipment. Additionally, by opening the wind tunnel test section door, the frequency of the fluctuations doubled. Unfortunately, due to the DyPPiR hydraulic system restrictions, the test section door is not permitted to be open with the hydraulic pressure on.
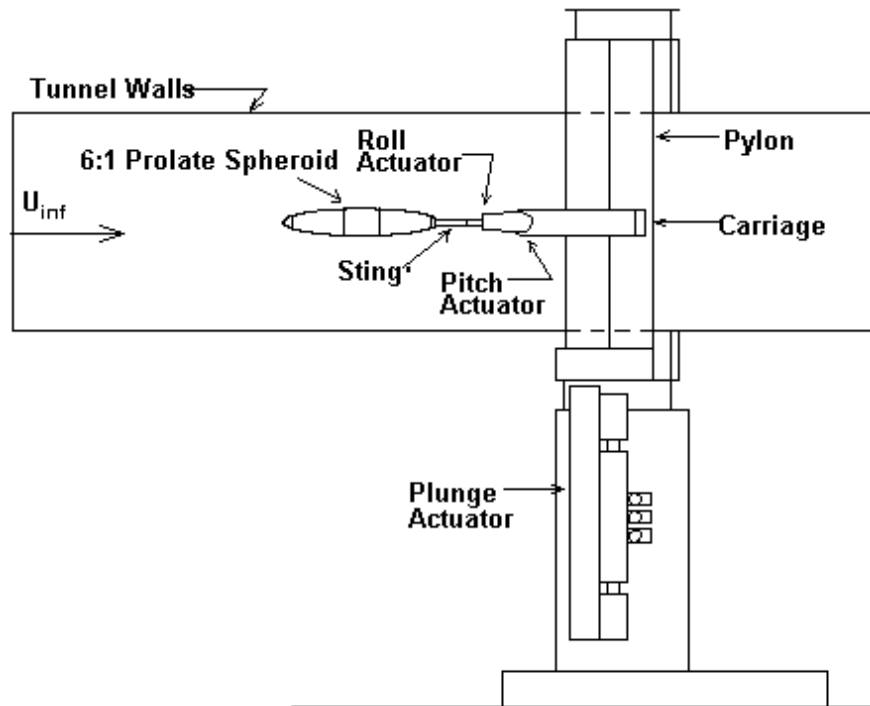
2.3 DyPPiR

Figure 2.21: DyPPiR schematic (from [77])

The Dynamic Plunge Pitch Roll apparatus (DyPPiR) in Figure 2.21, described in detail by Ahn [3] ans Simpson [73], is used for the dynamic tests. It is is a 3-degree of freedom hydraulically operated arm. It is rated to carry a model weighing no more than 50kg. It is capable of vertically actuating ± 650 mm at $9m/s$, pitching $\pm 45°$ at $120°/s$ and rolling the model $\pm 140°$. Model commanded- as well as actual position in vertical and pitch direction are at all times available and also digitized and recorded with loadcell data. According to the DyPPiR manual [82], position uncertainties are $\pm 0.65mm$ in plunge and $\pm 0.63°$ in pitch. Repeatability uncertainties during motions are $0.5mm$ in plunge and $0.1°$ in pitch acquired from recorded motion data in Section 4.3.

2.4 Sting

The sting used in the tests is a carbon-fiber reinforced epoxy tube with steel inserts to mount the sting to the DyPPiR and loadcell supports. The sting has a length of 1700mm, a weight of approximately 10kg and is described in more detail by Whitfield [85]. A single sting is used for the Ellipsoid and Suboff tests and mounted directly to the roll actuator.

The eigenfrequency of the entire model–loadcell–sting–DyPPiR is measured to be 53Hz for the single-sting setup by both Granlund [41] and Whitfield [85]. This is significantly higher than the frequency range of useful motions. Sting deformations were not taken into account, as needed by Fan and Lutze [25], because of the stiffer sting with higher eigenfrequency.

2.5 Loadcells

The loadcells are custom made, two-axis force loadcells of the same geometry as designed by Whitfield [85]. They are constructed as a 7075-T7 aluminum cantilever beam with a ball joint end for a moment-free installation shown in Figure 2.22. The flexures are equipped with two sets of Vishay TK-13-S076K-45C straingages in full bridge configuration with two straingages each on opposite side of the flexure. Three loadcells are mounted in the model to register loads in local y_l- and z_l-axes only.

Two loadcells are mounted to the front aluminum ring at the junction of the bow and constant cross-section midbody and a single loadcell is mounted to the rear aluminum ring at the junction of the midbody and stern according to Figures 2.23 and 2.24. With these three loadcells, forces in y- and z-axes and moments in all axes can be measured. Since the loadcells are oriented in the model x-direction, axial force X cannot be registered.
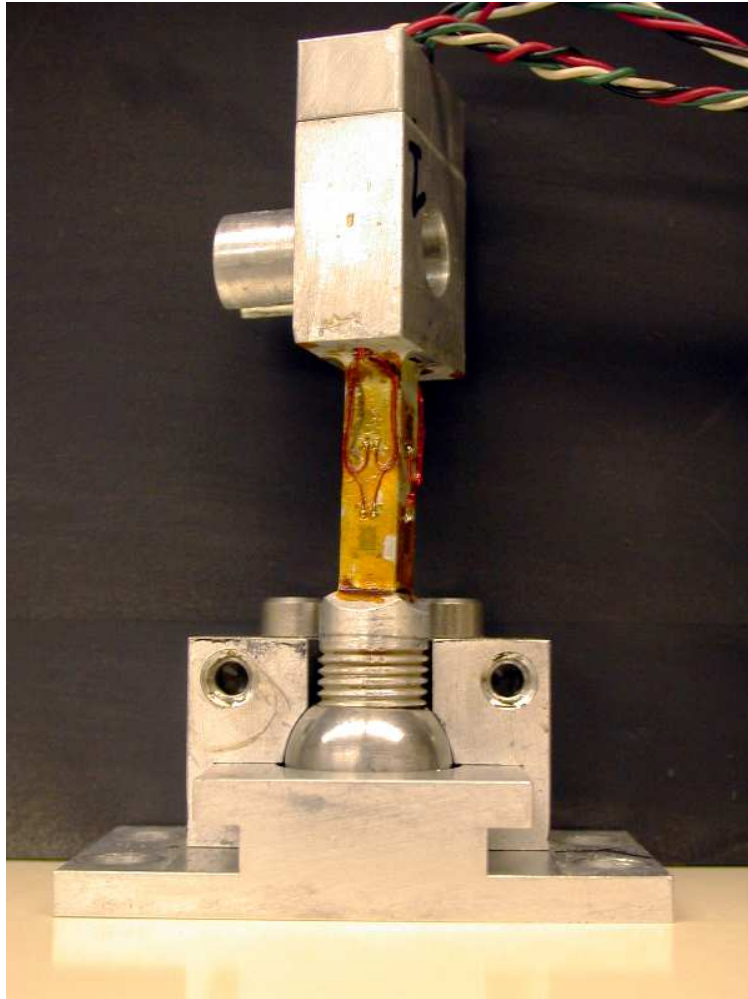
Figure 2.22: Loadcell with half of the base cap removed to expose the ball and socket joint
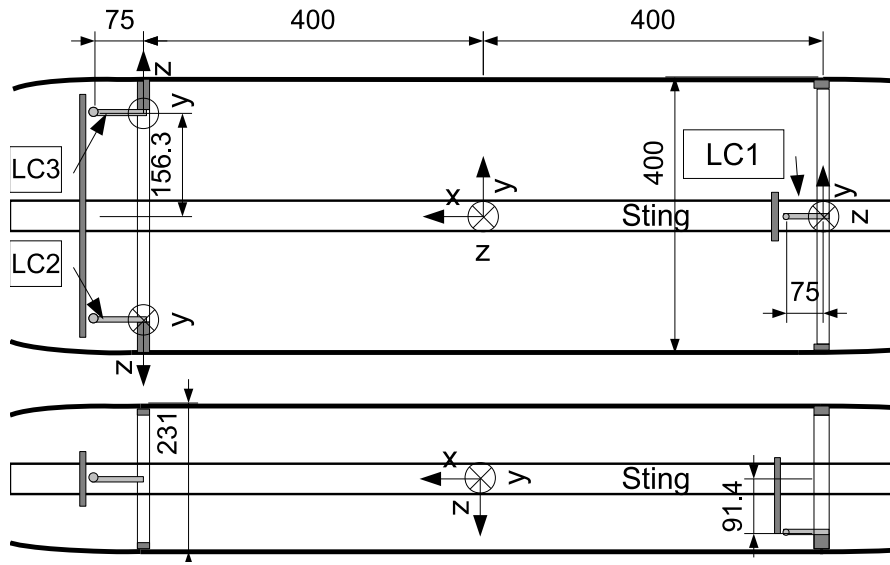
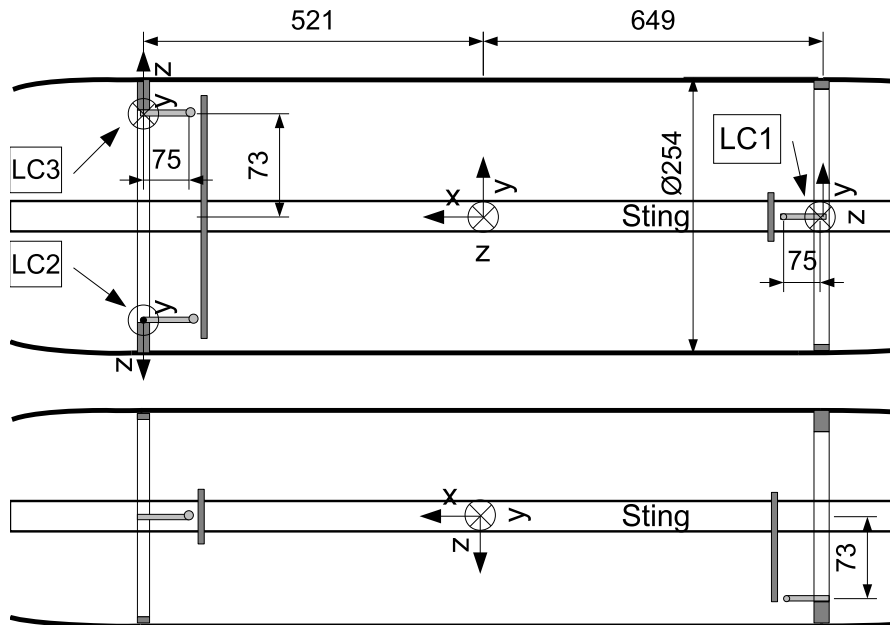Figure 2.23: Loadcell location in ellipsoid model (dimensions in mm)

Figure 2.24: Loadcell location in Suboff model (dimensions in mm)

43

The loadcell mount to the model aluminum ring has also been slightly redesigned for more durability from what used by Whitfield. The previous version used two 1/8" steel dowel pins in cutouts between the loadcell head and model ring hole as shown in Figure 2.25. This caused slight deformation of the material and play which was one source of excessive vibrations as measured by Granlund [41]. The improved construction consists of two ramps on the model aluminum ring forming a notch holding the entire square loadcell head as shown in Figure 2.26. The old loadcells can still be used with the new design.
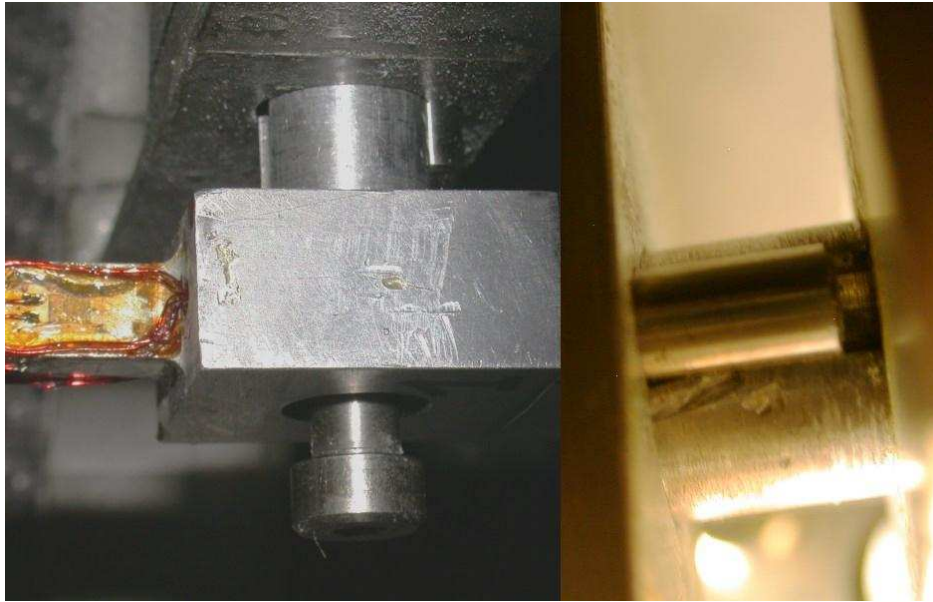

Figure 2.25: Older style loadcell mount with dowel pin

Figure 2.26: New style loadcell mount with ramp integrated in ring

New loadcells have been constructed of 1018 grade steel for heavier models. The dimensions of the loadcells are exactly the same as those made from aluminum, but the steel has a modulus roughly three times higher and thus have one-third the sensitivity. To match the temperature coefficient of expansion of steel, new Vishay TK-06-S076K-45C/DP straingages were selected with the otherwise same properties as those mounted on the aluminum flexures.
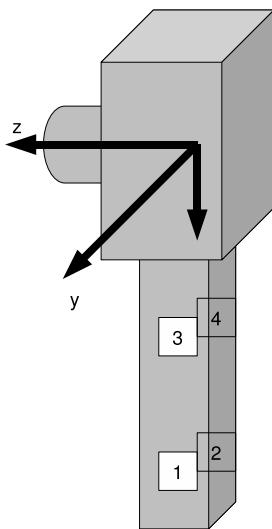

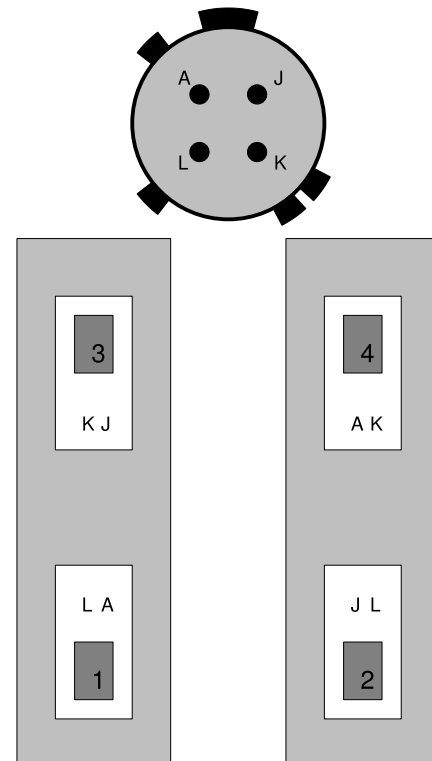Figure 2.27: Loadcell coordinate system and straingage numbering

Figure 2.28: Loadcell wiring diagram for straingages and connector

2.5.1 Loadcell calibration

The loadcells can register a wide range of frequencies, from DC to several kHz. The actual frequency response has not been tested, nor analyzed, but since the frequency of the motion of the wind tunnel tests is $< 10Hz$ which is very low, there is no reason to believe that the static calibration would be different from the low-frequency dynamic one. Each loadcell is calibrated in-situ connected to the same cables, amplifiers and external filters as in actual wind tunnel tests. To correctly align the applied force, a special calibration rig designed by John Fussell is used that is described in more detail in Granlund [41].

Calibrated weights are hung so as to load the ball end of the flexure at such a range so that the loadcell amplifiers register a voltage from 0 to maximum of 10V. With the amplifier gain setting at 1000, this set corresponds to a force from 10.26 to 113 N. Note that the amplifier does not need to be adjusted to 0 V at 0 N load. Only the slope is necessary information. A Labview script records the mean and standard deviation of a fixed set of samples.

Starting with straingage bridge y_l. The forces are transformed to the coordinate system of the loadcell according to Figure 2.29. There are problems with friction at very low forces in the calibration rig, so the smallest forces with nonlinear sensitivity are rejected. For every set (i.e. measurement angle), a linear least squares fit of data is employed. The data are then shifted in voltage as for the linear fit to have zero intercept (through the origin). The procedure is shown in Figure 2.30.
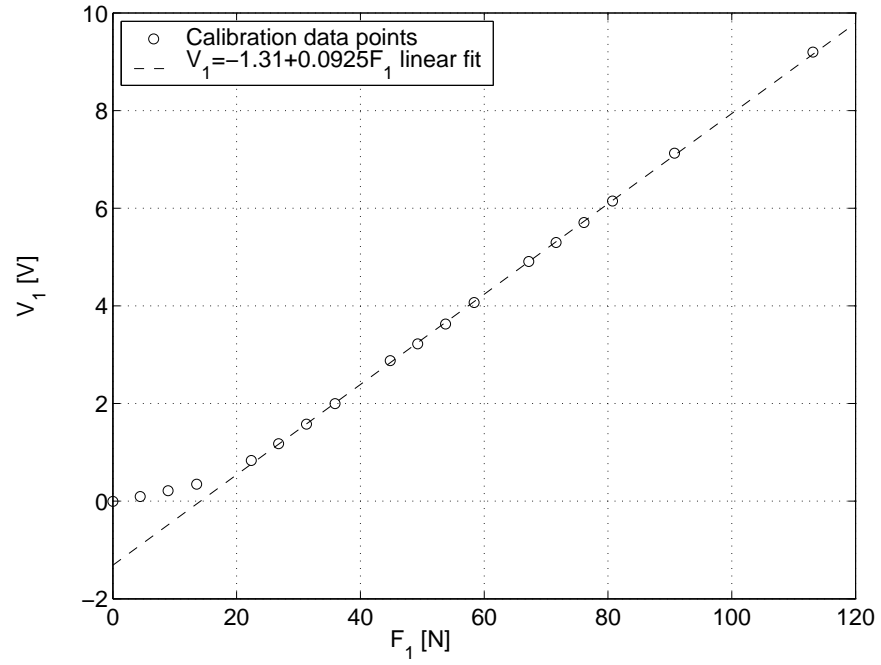
Figure 2.29: Raw calibration data with nonlinear points from calibration rig stick-slip friction
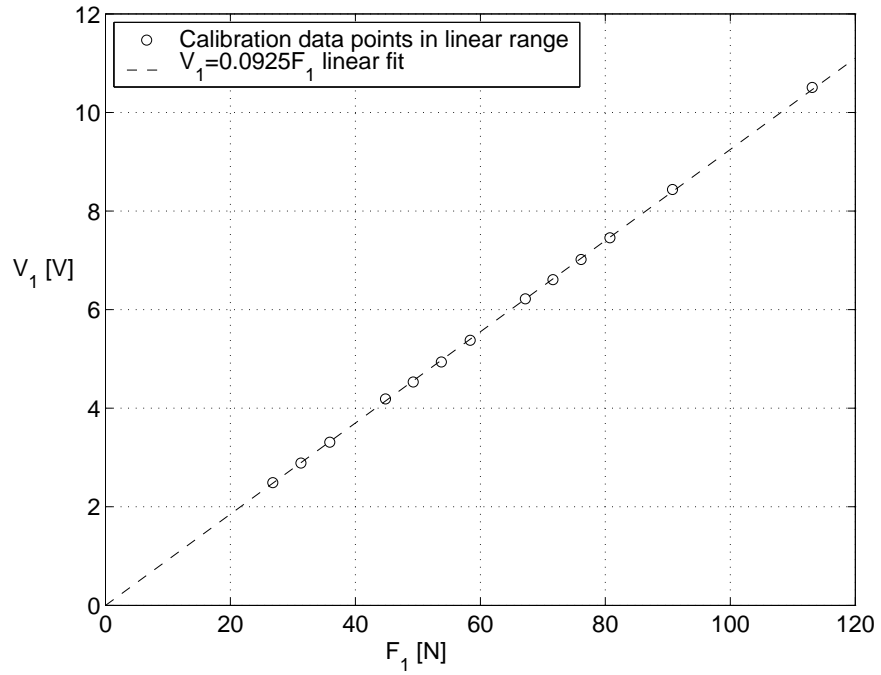

Figure 2.30: Cropped data with zero voltage bias

The six sets with forces in the y_l-direction are then plotted in the same window. According to Figure 2.31, there should be six linear sets of data, all positive definite. From this set, another linear least squares fit is employed according to Figure 2.31. This is the calibration coefficient of the y_l-axis bridge to y_l-axis load a_{yy}.
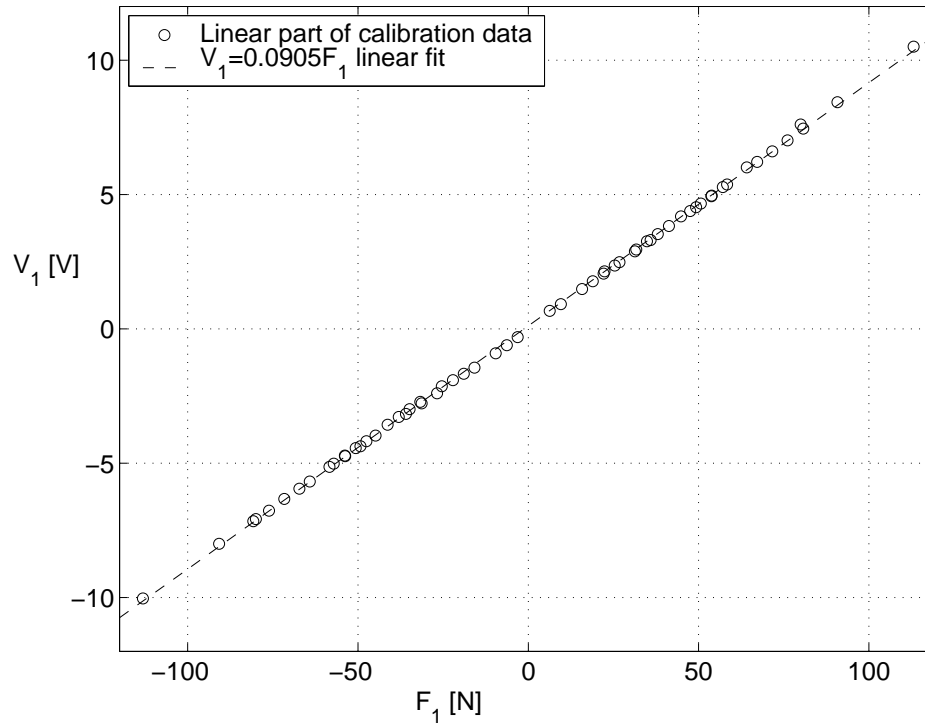

Figure 2.31: Combined data for tests on one bridge

Since the data points are individually recorded as mean and standard deviation, we can compute the variance of the calibration curve slopes as

$$Var\left[a_{yy}\right] = \sum_i \frac{Var\left[v_{yy,i}\right]}{F_{y,i}^2} \tag{2.19}$$

For the two sets with force applied in the z_l-axis direction and voltage registered on the y_l-direction bridge, the same procedure is repeated as above to obtain a_{yz}. and $Var(a_{yz})$

The same procedure is then totally repeated with the z_l-axis voltages to obtain a_{zz}, a_{zy}, $Var(a_{zz})$ and $Var(a_{zy})$. Now the calibration system of the whole loadcell is known as

$$\begin{bmatrix} v_y \\ v_z \end{bmatrix} = \begin{bmatrix} a_{yy} & a_{yz} \\ a_{zy} & a_{zz} \end{bmatrix} \begin{bmatrix} F_y \\ F_z \end{bmatrix} \tag{2.20}$$

Since the sensitivities of the loadcells are the most useful parameter, Equation 2.20 is inverted instead to

$$\begin{bmatrix} F_y \\ F_z \end{bmatrix} = \frac{1}{a_{yy}a_{zz} - a_{yz}a_{zy}} \begin{bmatrix} a_{zz} & -a_{yz} \\ -a_{zy} & a_{yy} \end{bmatrix} \begin{bmatrix} v_1 \\ v_2 \end{bmatrix} = \begin{bmatrix} b_{yy} & b_{yz} \\ b_{zy} & b_{zz} \end{bmatrix} \begin{bmatrix} v_1 \\ v_2 \end{bmatrix} \tag{2.21}$$

The variances of the measured forces are then for b_{yy}

$$Var\left[b_{yy}\right] = Var\left[a_{yy}\right]\left(\frac{\partial b_{yy}}{\partial a_{yy}}\right)^2 + Var\left[a_{yz}\right]\left(\frac{\partial b_{yy}}{\partial a_{yz}}\right)^2 \tag{2.22}$$

$$+ Var\left[a_{zy}\right]\left(\frac{\partial b_{yy}}{\partial a_{zy}}\right)^2 + Var\left[a_{zz}\right]\left(\frac{\partial b_{yy}}{\partial a_{zz}}\right)^2 \tag{2.23}$$

And similarly for b_{yz}, b_{zy} and b_{zz}. Where the partial derivatives are

$$\frac{\partial b_{yy}}{\partial a_{yy}} = \frac{-a_{zz}^2}{(a_{yy}a_{zz} - a_{yz}a_{zy})^2} \approx \frac{-1}{a_{yy}^2} \tag{2.24}$$

$$\frac{\partial b_{yy}}{\partial a_{yz}} = \frac{(-a_{zz})(-a_{zy})}{(a_{yy}a_{zz} - a_{yz}a_{zy})^2} \approx \frac{a_{zy}}{a_{yy}^2 a_{zz}} \tag{2.25}$$

$$\frac{\partial b_{yy}}{\partial a_{zy}} = \frac{(-a_{zz})(-a_{yz})}{(a_{yy}a_{zz} - a_{yz}a_{zy})^2} \approx \frac{a_{yz}}{a_{yy}^2 a_{zz}} \tag{2.26}$$

$$\frac{\partial b_{yy}}{\partial a_{zz}} = \frac{a_{yy}a_{zz} - a_{zz}a_{yy}}{(a_{yy}a_{zz} - a_{yz}a_{zy})^2} = 0 \tag{2.27}$$

$$\frac{\partial b_{yz}}{\partial a_{yy}} = \frac{a_{yz}a_{zz}}{(a_{yy}a_{zz} - a_{yz}a_{zy})^2} \approx \frac{-a_{yz}}{a_{yy}^2 a_{zz}} \tag{2.28}$$

$$\frac{\partial b_{yz}}{\partial a_{yz}} = \frac{-a_{yy}a_{zz} + a_{yz}a_{zy}}{(a_{yy}a_{zz} - a_{yz}a_{zy})^2} \approx \frac{-1}{a_{yy}a_{zz}} \tag{2.29}$$

$$\frac{\partial b_{yz}}{\partial a_{zy}} = \frac{a_{yz}(-a_{yz})}{(a_{yy}a_{zz} - a_{yz}a_{zy})^2} \approx \frac{-a_{yz}^2}{a_{yy}^2 a_{zz}^2} \tag{2.30}$$

$$\frac{\partial b_{yz}}{\partial a_{zz}} = \frac{a_{yz}a_{yy}}{(a_{yy}a_{zz} - a_{yz}a_{zy})^2} \approx \frac{a_y z}{a_{yy}a_{zz}} \tag{2.31}$$

$$\frac{\partial b_{zy}}{\partial a_{yy}} = \frac{a_{zy}a_{zz}}{(a_{yy}a_{zz} - a_{yz}a_{zy})^2} \approx \frac{a_{zy}}{a_{yy}^2 a_{zz}} \tag{2.32}$$

$$\frac{\partial b_{zy}}{\partial a_{yz}} = \frac{a_{zy}(-a_{zy})}{(a_{yy}a_{zz} - a_{yz}a_{zy})^2} \approx \frac{-a_{zy}^2}{a_{yy}^2 a_{zz}^2} \tag{2.33}$$

$$\frac{\partial b_{zy}}{\partial a_{zy}} = \frac{-a_{yy}a_{zz} + a_{zy}(-a_{yz})}{(a_{yy}a_{zz} - a_{yz}a_{zy})^2} \approx \frac{-1}{a_{yy}a_{zz}} \tag{2.34}$$

$$\frac{\partial b_{zy}}{\partial a_{zz}} = \frac{a_{zy}a_{yy}}{(a_{yy}a_{zz} - a_{yz}a_{zy})^2} \approx \frac{a_{zy}}{a_{yy}a_{zz}^2} \tag{2.35}$$

$$\frac{\partial b_{zz}}{\partial a_{yy}} = \frac{a_{yy}a_{zz} - a_{yy}a_{zz}}{(a_{yy}a_{zz} - a_{yz}a_{zy})^2} = 0 \tag{2.36}$$

$$\frac{\partial b_{zz}}{\partial a_{yz}} = \frac{(-a_{yy})(-a_{zy})}{(a_{yy}a_{zz} - a_{yz}a_{zy})^2} \approx \frac{a_{zy}}{a_{yy}a_{zz}^2} \tag{2.37}$$

$$\frac{\partial b_{zz}}{\partial a_{zy}} = \frac{(-a_{yy})(-a_{yz})}{(a_{yy}a_{zz} - a_{yz}a_{zy})^2} \approx \frac{a_{yz}}{a_{yy}a_{zz}^2} \tag{2.38}$$

$$\frac{\partial b_{zz}}{\partial a_{zz}} = \frac{-a_{yy}^2}{(a_{yy}a_{zz} - a_{yz}a_{zy})^2} \approx \frac{-1}{a_{zz}^2} \tag{2.39}$$

Since a_{yy}, $a_{zz} \gg a_{yz}$, a_{zy}, only the partial derivatives of variables with respect to the same indices are left. The variances of the sensitivities are thus

$$Var\left[b_{yy}\right] = Var\left[a_{yy}\right]\left(\frac{\partial b_{yy}}{\partial a_{yy}}\right)^2 \tag{2.40}$$

$$Var\left[b_{yz}\right] = Var\left[a_{yz}\right]\left(\frac{\partial b_{yz}}{\partial a_{yz}}\right)^2 \tag{2.41}$$

$$Var\left[b_{zy}\right] = Var\left[a_{zy}\right]\left(\frac{\partial b_{zy}}{\partial a_{zy}}\right)^2 \tag{2.42}$$

$$Var\left[b_{zz}\right] = Var\left[a_{zz}\right]\left(\frac{\partial b_{zz}}{\partial a_{zz}}\right)^2 \tag{2.43}$$

The variances in the forces are thus

$$
\begin{aligned}
Var\left[F_1\right] &= Var\left[b_{yy}\right]v_1^2 + Var\left[b_{yz}\right]v_2^2 + b_{yy}^2 Var\left[v_1\right] + b_{yz}^2 Var\left[v_2\right] \\
&= Var\left[a_{yy}\right]\frac{1}{a_{yy}^4}v_1^2 + Var\left[a_{yz}\right]\frac{1}{a_{yy}^2 a_{zz}^2}v_2^2 + b_{yy}^2 Var\left[v_1\right]
\end{aligned} \tag{2.44}
$$

and

$$
\begin{aligned}
Var\left[F_2\right] &= Var\left[b_{zy}\right]v_1^2 + Var\left[b_{zz}\right]v_2^2 + b_{zy}^2 Var\left[v_1\right] + b_{zz}^2 Var\left[v_2\right] \\
&= Var\left[a_{zy}\right]\frac{1}{a_{yy}^2 a_{yy}^2}v_1^2 + Var\left[a_{zz}\right]\frac{1}{a_{zz}^4}v_2^2 + b_{zz}^2 Var\left[v_2\right]
\end{aligned} \tag{2.45}
$$

The loadcell calibration constants are located in Appendix B.

2.6 Data acquisition system

Every axis of the loadcells is connected to a Vishay 2310 loadcell conditioning amplifier [81] — in total six. The output signals are first low pass filtered with an active circuit built into the loadcell amplifier to remove large amplitude noise before conversion to digital signals. Initially a National Instruments PCI-MIO-16XE-10 card was used for conversion, but as this ISA-based PC card stopped functioning in 2006, a National Instruments SCXI-1600 USB-based digital-to-analog conversion unit was used instead. The loadcell- and DyPPiR position command and feedback data are recorded in the PC with custom made LabView [50] scripts. Data are recorded at $f_s = 1000Hz$ for the duration of a motion with the DyPPiR. For steady, fixed-position tests, data are recorded for 10 seconds. An automated LabView script for reducing steady loadcell data to mean and standard deviation while recording does exist, but it is not used.

Wind tunnel dynamic- and static pressure, temperature as well as DyPPiR commanded and actual positions are recorded simultaneously together with loadcell data as described by Granlund [41].

2.6.1 Loadcell amplifier filter modification

The built-in filter in the amplifiers is of a Sallen-Key [69] design in Figure 2.32 with fixed resistor values and capacitors selectable via push-buttons on the amplifier front panel. The transfer function of each filter stage is given by

$$f_c = \frac{1}{2\pi\sqrt{R^2 C_1 C_2}} \qquad (2.46)$$

$$Q = \frac{\sqrt{R^2 C_1 C_2}}{(R_1 + R_2)C_1} = \sqrt{\frac{C_2}{4C_1}} \qquad (2.47)$$
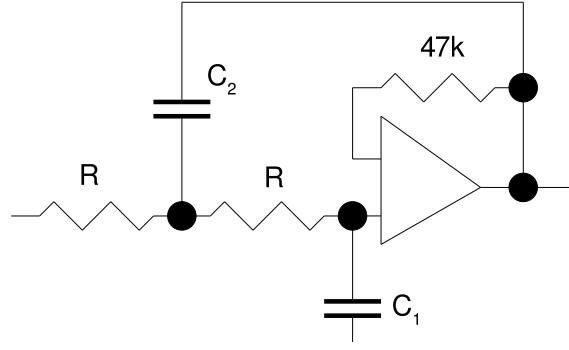
Figure 2.32: Vishay 2310 built–in filter circuit diagram

$$H \quad = \quad \frac{1}{\frac{1}{2\pi f_c^2}s^2 + \frac{1}{2\pi f_c Q}s + 1} \qquad (2.48)$$

Initially, the built-in amplifier filter was a second order low-pass Butterworth type active

R (Ω)	$22.6k$
$C_{1,10}$ (F)	0.5μ
$C_{2,10}$ (F)	1μ
$C_{1,100}$ (F)	0.05μ
$C_{2,100}$ (F)	0.1μ
$C_{1,1k}$(F)	0.005μ
$C_{2,1k}$ (F)	0.01μ
$C_{1,10k}$(F)	0.0005μ
$C_{2,10k}$ (F)	0.001μ

Table 2.8: Vishay 2310 original filter component values

circuit with the selectable frequency of 10, 100, 1000 or 10000 Hz. The filter circuit consists of a single Sallen-Key [69] stage in Figure 2.32 with component values in Table 2.8. The operational amplifier is a National Semiconductor LM741 [71]. The filter parameters for the second order 10 Hz filter turn out to be

$$f_c \quad = \quad \frac{1}{2\pi\sqrt{33k^2 \cdot 1\mu \cdot 0.5\mu}} = 9.95 Hz \qquad (2.49)$$

$$Q \quad = \quad \frac{\sqrt{R^2 C_1 C_2}}{(R_1 + R_2)C_1} = \sqrt{\frac{C_2}{4C_1}} = \sqrt{\frac{1\mu}{4 \cdot 0.5\mu}} = 0.707 \qquad (2.50)$$

$$H \ = \ \frac{1}{\frac{1}{R^2 C_1 C_2} s^2 + \frac{1}{2RC_1} s + 1} = \frac{1}{22.6k^2 \cdot 1\mu \cdot 0.5\mu s^2 + 2 \cdot 22.6k \cdot 0.5\mu s + 1}$$

$$(2.51)$$

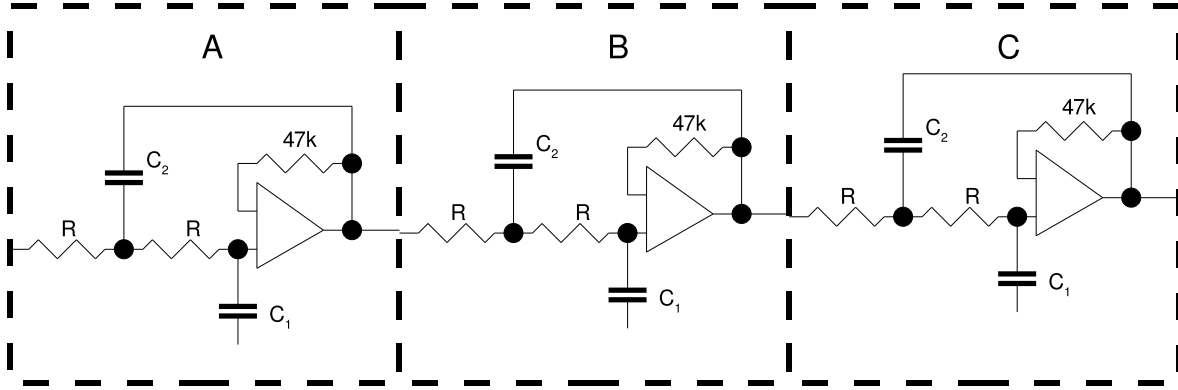The filtering circuit was upgraded to a sixth order low-pass Butterworth filter by adding

Figure 2.33: Vishay 2310 modified filter circuit diagram

components on the circuit board for cascading three second order stages shown in Figure 2.33. The new modified filter has the selectable cutoff frequencies of 5, 50, 500 and 5000 Hz. Components were primarily selected for a 5Hz cutoff frequency instead of the original 10Hz becuse of a need to filter out DyPPiR maneuver induced noise near and above 7 Hz. As an added benefit, one can now filter out 60Hz electric power noise with the 50Hz filter. The resistors and capacitors used all have 1% tolerance for more accurate control of the filter characteristics in the post-processing of data. The components of the three filter stages were selected initially from the Analog Devices Interactive Filter Design Java Applet [17] and then adjusted to standard component values. A $100pF$ capacitor was chosen for $C_{2c,5k}$ to keep the filter capacitance larger than the input capacitance of the operational amplifier to avoid instability.

A Monte-Carlo simulation of the modified filter with the component values and uncertainties in a seed of $n = 10,000$ different combinations was performed to investigate the uncertainties.
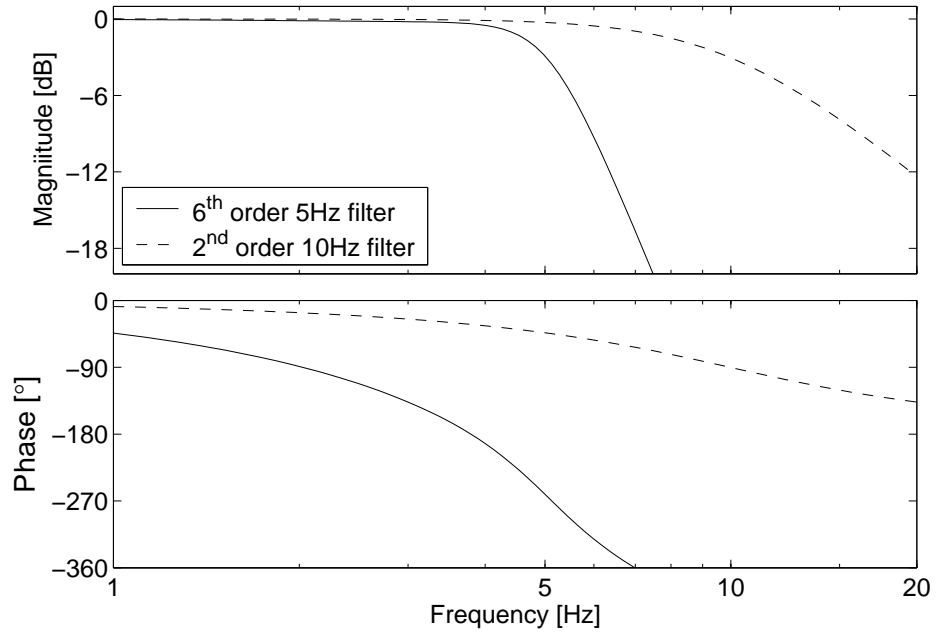
Figure 2.34: Vishay 2310 modified and unmodified filter magnitude response comparison

	A	B	C
R (Ω)	$33k$	$45k$	$124k$
$C_{1,5}$ (F)	$2x0.47\mu$	0.47μ	0.068μ
$C_{2,5}$ (F)	$2x0.47\mu$	$2x0.47\mu$	$2x0.47\mu$
$C_{1,50}$ (F)	0.1μ	0.047μ	$6.8n$
$C_{2,50}$ (F)	0.1μ	0.091μ	0.1μ
$C_{1,500}$ (F)	0.01μ	0.0047μ	$0.68n$
$C_{2,500}$ (F)	0.01μ	0.091μ	0.01μ
$C_{1,5k}$ (F)	0.001μ	0.0005μ	$100p$
$C_{2,5k}$ (F)	0.001μ	0.001μ	0.001μ

Table 2.9: Vishay 2310 modified filter component values
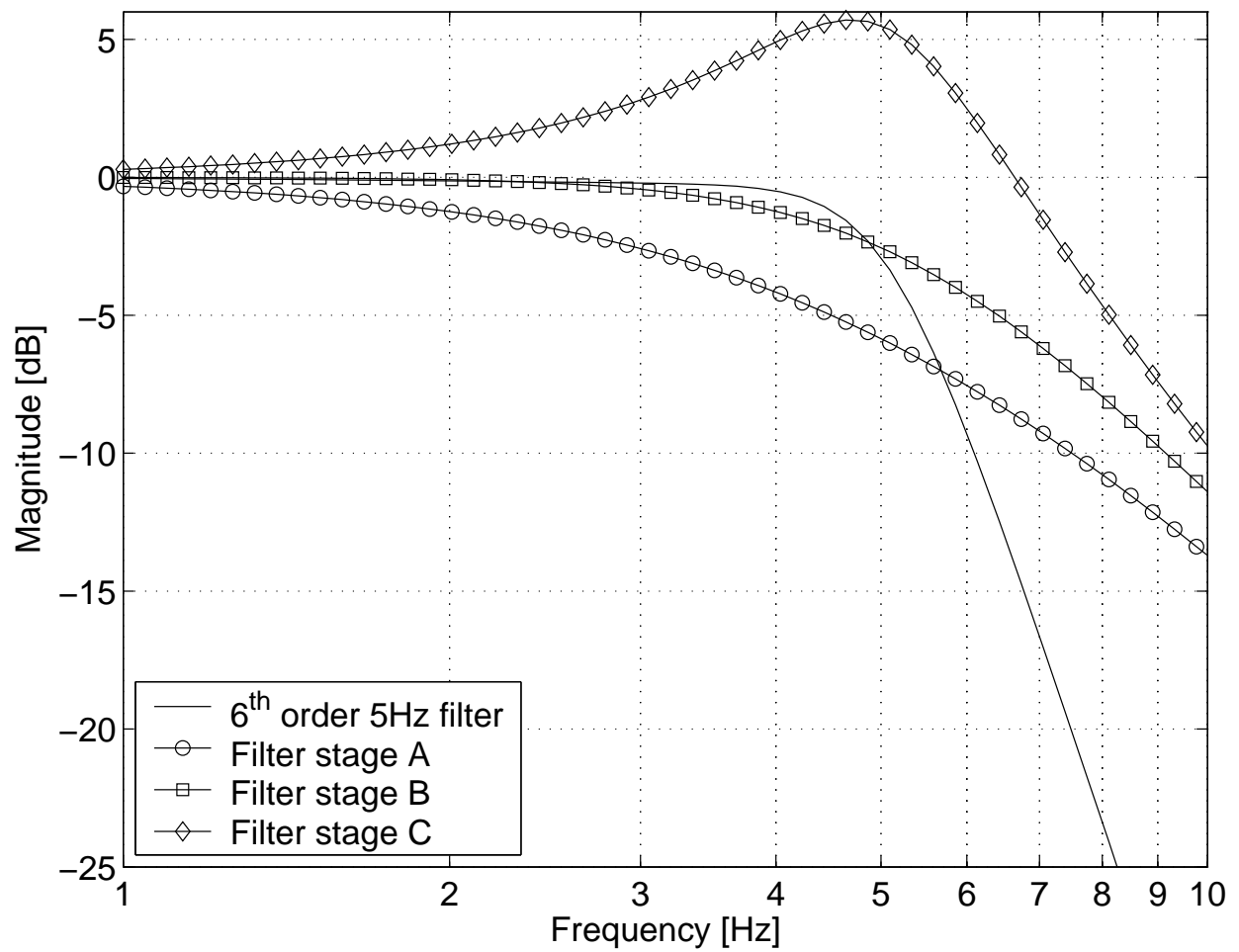
Figure 2.35: Vishay 2310 separate stage filter magnitude response
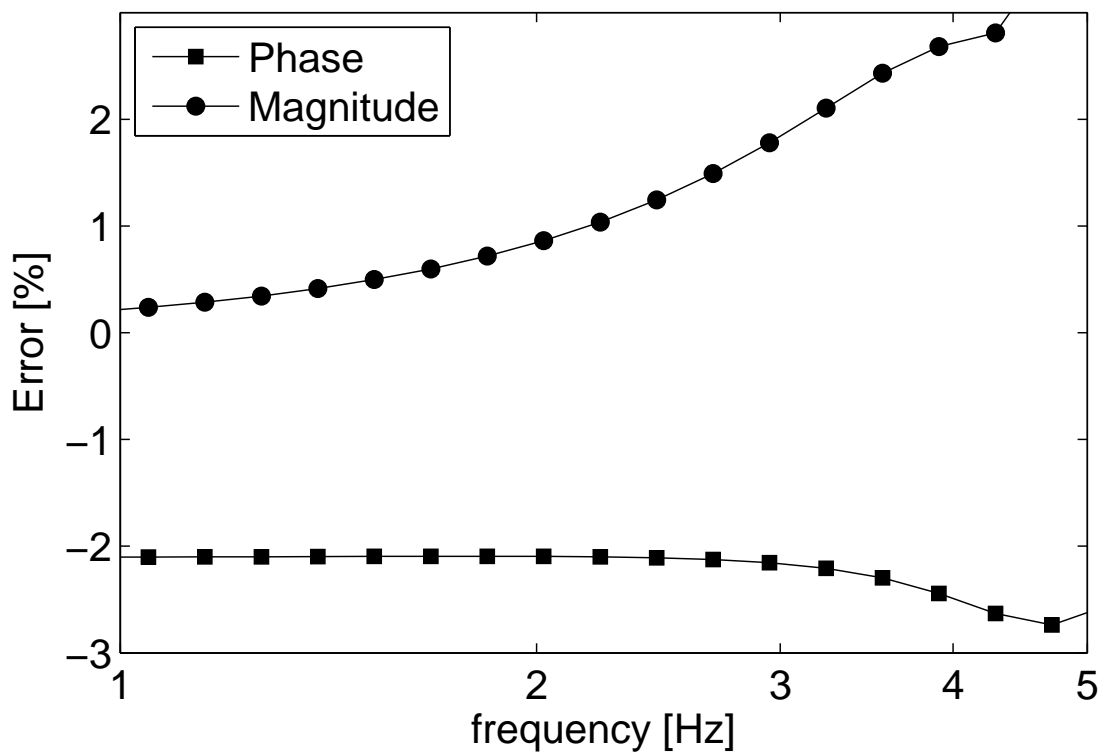
Figure 2.36: Filter modification error magnitudes

From Figure 2.36 we can observe that the modified filter has a magnitude uncertainty of well below 1% for frequency components up to $2Hz$ and $< 0.2\%$ under $1Hz$. Regular dynamic motions are pitch and/or plunge ramps for $\approx 0.25s$ which can be seen as a half-wave. The fundamental frequency of the motion is then on the order of $2Hz$. According to Figure 2.36 the filter magnitude uncertainties are lower than the calibration and repeatability uncertainties.

For the phase uncertainty contributions we can observe that the phase uncertainties are a constant 2% in the useful frequency range $< 2Hz$. If we assume a linear phase response, for a simplified uncertainty calculation purpose, the phase delay at $2Hz$ is $-90°$. This means that a $2Hz$ sinewave with a $0.5s$ period would be delayed $0.125s$ through the filter. A 2% phase response uncertainty would then mean a $\pm 2.5ms$ uncertainty in time. This corresponds to a non-dimensionalized time error $t'_{error} \approx 0.07$ which is significantly less than what can be observed in the qualitative analysis of the unsteady vs. quasi-steady results.

2.6.2 External filter modules

Optional Krohn-Hite 3202 external filter modules can be inserted in the signal chain before digital conversion of the signals, but were not used in these experiments. Each channel can be configured in either low-, band or high-pass configuration with Butterworth response. For the low- and high-pass configurations, the eight-pole circuit give a 48dB/octave cutoff slope. In band-pass configurations, each side has four poles producing a 24 dB/octave slope. However, these only have $\pm 5V$ input range and a lowest cutoff frequency of 20 Hz and therefore would not be useful unless there still is excessive noise at high frequencies left after the Vishay 2310 built-in filters.

Chapter 3

Postprocessing

During the experiment, the measured data is modified in different ways to improve the signal properties before being recorded and later processed into useful measurable quantities that are relevant for the experiment.

3.1   Filtering signals

In experiments, very seldom does the transducer produce a directly useful signal that only contains the mesured signal at an amplitude that can be recordable for later analysis. When working with time- and ensemble dependent signals, one often needs to reject parts of the data that for one reason or another should not be represented in the final results. For ensembles of data, one can generally justify removing a data point not following the general trend if justified by the Chauvenet's Criterion[48]. For recorded time-dependent data, one generally wants to remove unwanted ranges of frequencies. This can be done in different stages in the data acquisition process.

During unsteady wind-tunnel testing, one only wants to record frequency-bandwidth of signals that are correlated with the motion itself. For force- and moment measurements, only the macroscales of the flow such as the separation, vortical structures etc. are correlated with global forces on the body. The high frequency microscale turbulence of the flow is not correlated and is filtered out.

The eigenfrequency of any of the structural parts in the system also needs to be substantially larger than the fundamental frequency of the unsteady motion itself. The need for a substantial bandwidth of the unsteady motion is that the loadcells need to be able to pick up transients from fluid mechanics phenomena during the unsteady motion that occur at a much smaller timescale than the motion itself. An example is the vortex burst occuring over delta wings. The uncorrelated signals can be removed by either low-pass filtering or obtaining information on the model acceleration through accelerometers or feedback information of the pitch and plunge actuator position.

3.1.1 Filtering history

At first, Whitfield [85] recorded data with the Vishay 2310 amplifier built-in 2-pole Butterworth 100Hz setting. This proved to be inadequate since the eigenfrequency of the model-loadcell-sting package was analyzed to be 53Hz. This proved to be inadequate for two reasons; the first being that the loadcells overranged in dynamic tests which makes it quite impossible to accurately reduce the individual loadcell signals to full model forces and moments. The second problem was that the loadcell signals contained too much high frequency information - most notably the eigenfrequency of the physical setup. Attempts were made by Granlund [41] to conduct the signal processing entirely in software in order to better understand the frequency content of the loadcell signals. The motivation for this was

that the three accelerometers have an electric circuit with an unknown transfer function and better time-correlation between the loadcell- and accelerometer data would be the result. Unfortunately, this proved not to be the case since the accelerometer data could not be used in the data reduction process. The linear and rotational accelerations of the model could not be extracted from the very noisy data. Through frequency content analysis, a latter attempt via low-pass software filtering turned out to be successful in reducing the loadcell signals to observe a statistical difference with low-uncertainty of similar maneuvers with small differences [43].

3.2   Analog filtering

Since the signals recorded from the loadcells contain high-frequency high-amplitude noise, it is preferred to filter these signals before Analog-to-Digital (A/D) conversion to be able to use the full range of the A/D converter. For example; if the noisy signal is $10V_{pp}$, which is the same range of the A/D converter and the clean part of the signal is only $5V_{pp}$, digitizing the noisy signal and then performing digital filtering will reduce the resolution and increase the uncertainty of the final signal. Therefore, it is desirable to identify the highest useful frequency information in the signal and low-pass filter out the noise in combination with increasing the gain on the amplifiers to use the full range of the A/D converter for the desired signal.

3.3 Effects of filtering

The main reason for filtering is the attenuation of undesired frequency ranges of the signal. The other, and often neglected effect is a time lag of the signals. The frequency response of the built-in second order Butterworth 10Hz low-pass filters of the loadcell amplifiers is shown in Figure 3.1.
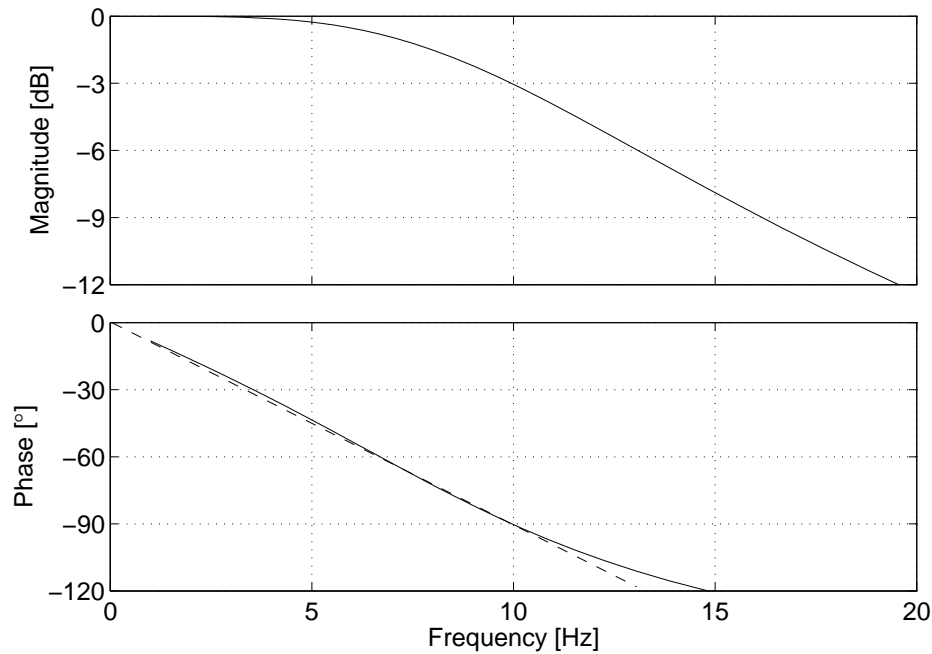
Figure 3.1: Bode plot of 2310 amplifier 2nd order 10Hz filter with linear phase approximation

One can observe that the phase response is almost linear and $-90°$ at 10Hz. This means that a sine wave at 10Hz taking 0.1s for a full period will be delayed one-quarter period as shown in Figure 3.2. The group delay is thus 0.025s for this filter meaning that all samples digitized by the A/D converter will be 25ms late. This signal needs to be shifted back in time to coincide with unfiltered recorded signals such as DyPPiR position feedback signals.
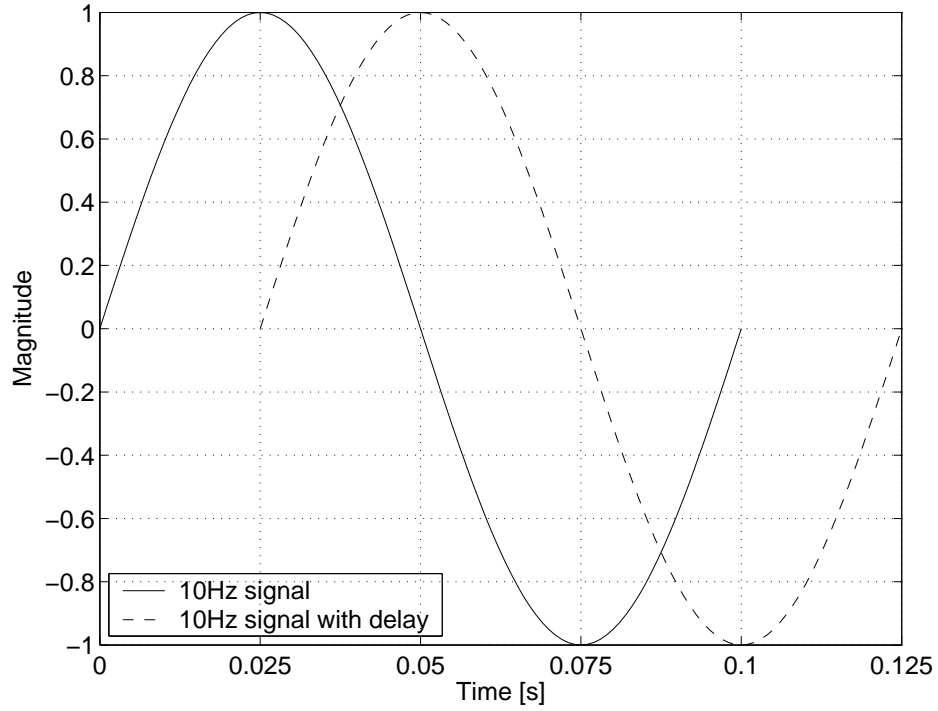
Figure 3.2: Phase delayed signal for 2310 2nd order 10Hz filter

During tests, external Krohn-Hite filter modules can also be connected between the 2130 amplifies and the DAQ system, altough they were not used in these experiments. The Krohn-Hite filters are fourth order Butterworth set to minimum filtering frequency 20Hz. This produces the total filter in Figure 3.3 with a nearly linear phase response of $-168°$ at $10Hz$. The group delay for this combination of filters will be 47ms.
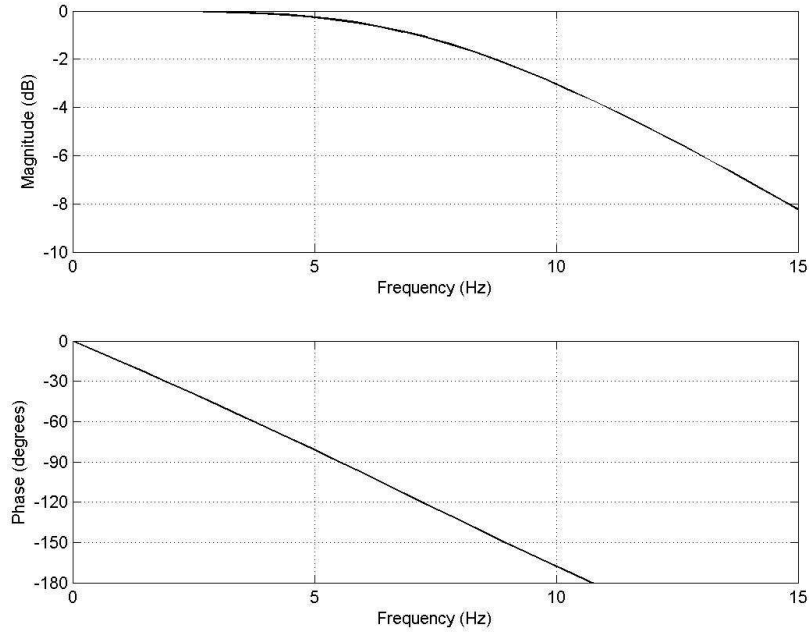
Figure 3.3: Bode plot of 2310 10Hz + K-H 20Hz LP filters

3.3.1 Filtering correction

There exists one problem with using the external filters. The inputs on the Krohn-Hite filters are only rated $5V_{pp}$ which is half the range of the amplifier inputs. This has the effect of producing much larger slope uncertainties of the loadcells than if the external filters are not connected and the full $10V_{pp}$ amplifier input range is available. The lowest cutoff frequency for the external filters is 20Hz which puts some boundaries on the reasonable use of them. The difference in frequency response between the use of only the built-in 10Hz filter and both the builtin and the external filter is shown in Figure 3.3. There is no difference between 10Hz and 20Hz. Only if noise at frequencies over 20Hz does it make sense to use the external filters. Otherwise one will simply have an increased magnitude of uncertainty.

3.4   Linear vs. nonlinear phase filters

For reducing large noise amplitudes, higher order filters are needed if one wants to preserve the same passband. Higher order hardware filters have more phase distortion. For the load-cell amplifier filter modification, the higher order filter no longer has an approximate linear phase response as shown in Figure 3.4. If left untreated, this would have some undesirable consequenses of the data in the passband. Any frequency component $f < f_c$ would no longer have the same time delay as another frequency component. The delay is dependent on the frequency and will cause phase distortion of the signals which can give a false indication of unsteady flow phenomena. Another problem with the linear phase filter is that the stopband cutoff is not as sharp as for the nonlinear phase filters. One can observe more attenuation in the passband and less in the stopband for frequencues near the cutoff.
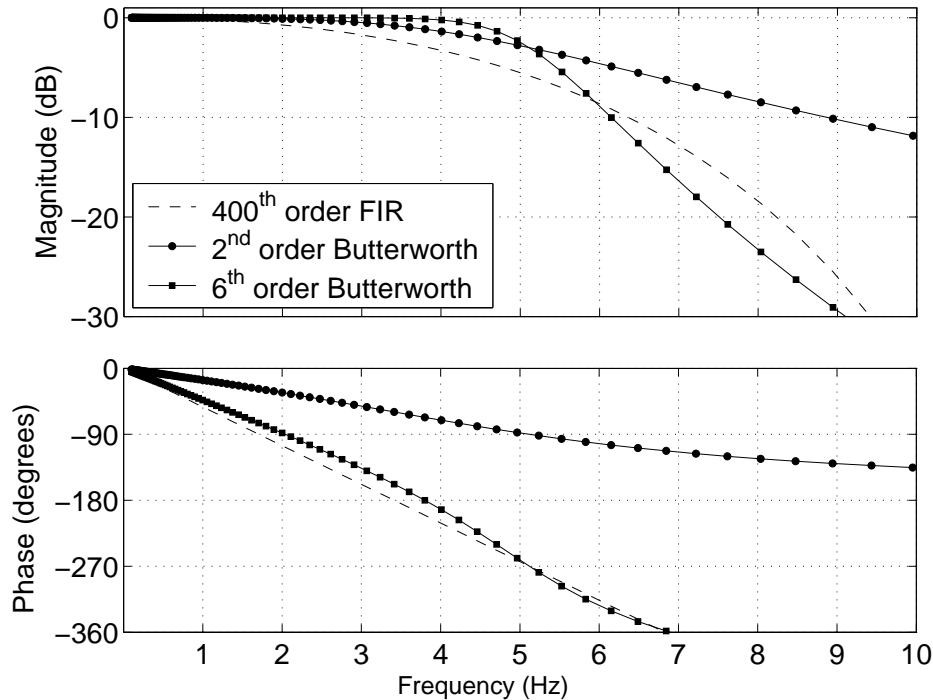
Figure 3.4: Bode plot of comparison between FIR and IIR filters

An advantage of the lower order and linear phase filters is that they produce less ringing from filtering out impulses as shown in Figure 3.5. A Finite Impulse Response filter with linear phase response will simply time delay the signal half the number of samples of the order of the filter. Even though this is a very desirable trait, there would be considerable difficulty constructing such a hardware filter, not only because of the difficulty in selecting the discrete components that matches the filter parameters, but the sheer number of components in the filter will make the uncertainties increase tremendously.
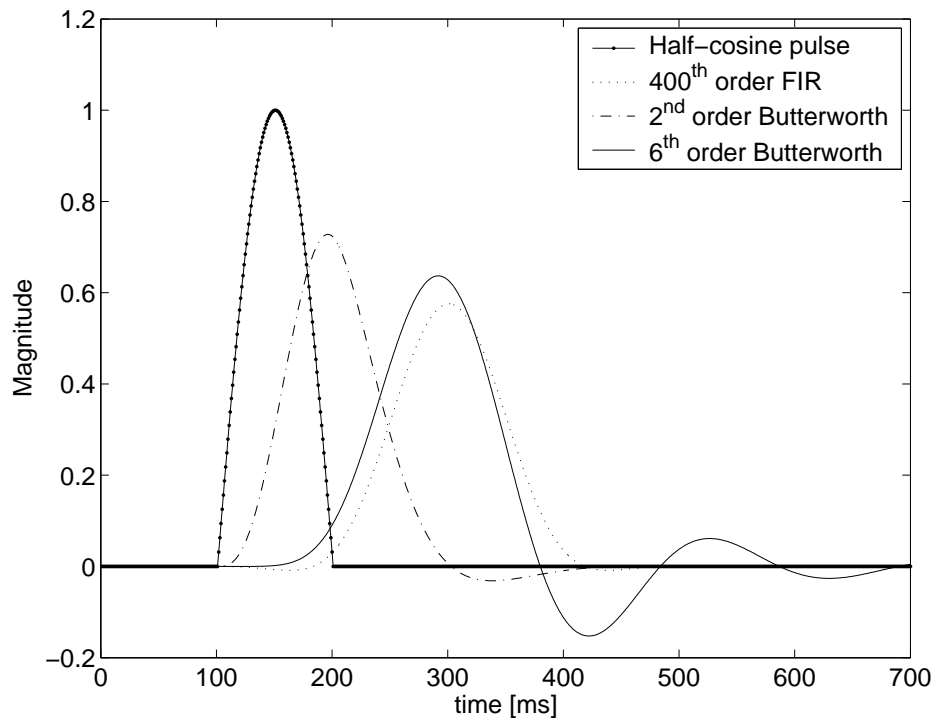
Figure 3.5: Ringing comparison between FIR and IIR filters for pulse response

One way of correcting the phase distorted signals is to feed them through a inversed filter of the same kind. However, if the hardware filter is recreated in software and the time dimension of the recorded signals is reversed, all phase distortions will be completely corrected and the filter will order be doubled.

3.5 Data reduction

Loadcell data are reduced to global forces and moments in the same way as in Granlund [41] with a few exceptions. Raw loadcell data are first filtered in reverse time with the amplifier filter recreated in software as described above to obtain the useful frequency content $f < 5Hz$. The voltage signals are then converted to forces using the calibration system of functions in Appendix B.

$$\begin{bmatrix} F_1 \\ F_2 \end{bmatrix} = \begin{bmatrix} b_{11} & b_{12} \\ b_{21} & b_{22} \end{bmatrix} \begin{bmatrix} F_1 \\ F_2 \end{bmatrix} \tag{3.1}$$

For steady tests, all signals are reduced to mean and variance.

$$F = \frac{1}{N} \sum_i^N F(t_i) \tag{3.2}$$

$$Var\,[F] = \frac{1}{N} \sum_i^N (F(t_i) - F)^2 \tag{3.3}$$

The individual loadcell forces are summed up into model global forces and moments with respect to the moment reference point given in the Appendix.

In order to make sure that the filtering process maximizes the reduction of the noisy parts and minimizes any adverse effects on the low frequency part of the signal that contains the information of the aerodynamic contributions. Figure 3.6 shows how a fictional, but similar to the performed unsteady maneuvers, electric signal from a loadcell is modified during the filtering process. The loadcell attached to the model is rotated via a linear ramp motion starting from, for example, $-15°$ negative angle of attack, corresponding to a $-5V$ signal and to a final $+15°$ angle corresponding to a $+5V$ signal, respectively. The model, and loadcell is subjected to a maneuver start impulse and also an ending impulse. Since the impulse

enters the data prior to the hardware amplifier and filter, it is created from observing how the raw digitized recorded signal, with the impulse noise, looks like after being filtered. The figure shows how the raw impulse signal from the loadcell starts out with a large amplitude and dampens out during the motion. At the end of the motion, when the model is stopped, a similar impulse occurs. After the signal passes through the filter, the high frequency oscillations are attenuated and most notably, the entire signal is delayed a significant amount before recorded and converted to digial format. In order to correct for the delay/phase shift, the recorded signal is reversed in time, fed through the reproduced filter in software and finally reversed back. In close observation, the phase corrected signal will actually have slightly larger oscillations in the middle of the motion than the signal that is only hardware filtered. The reason for this is because an impulse or oscillation that is filtered is 'smeared out' forward in time while it is attenuated. In this case, it is the motion ending impulse that is smeared out back into the motion time window during the time-backward filtering process.

To further reduce the oscillations from the recorded loadcell data signals, they are filtered a second time. The second filtering process is done via Matlab's built in *filtfilt* zero-phase filtering module with a sixth order $-30dB$ Chebyshev2 filter to achieve a sharper magnitude rolloff at the expense of stopband ringing. As is evident in a qualitative analysis in Figure 3.7, it is important to choose the cutoff frequency of the second filter properly. If the cutoff frequency is chosen at $6Hz$, which is higher than the previous cutoff frequency of $5Hz$, not much will happen with the oscillations. They will only be attenuated a very minor amount and mostly, the peaks will shift a little bit in time. Using the same $5Hz$ cutoff frequency in both parts, one can observe that the filtered signal follows the original ramp signal correctly in magnitude and trend in the middle part of the motion. In the beginning and end of the motion, the magnitude exceeds the correct value by a noticable amount because
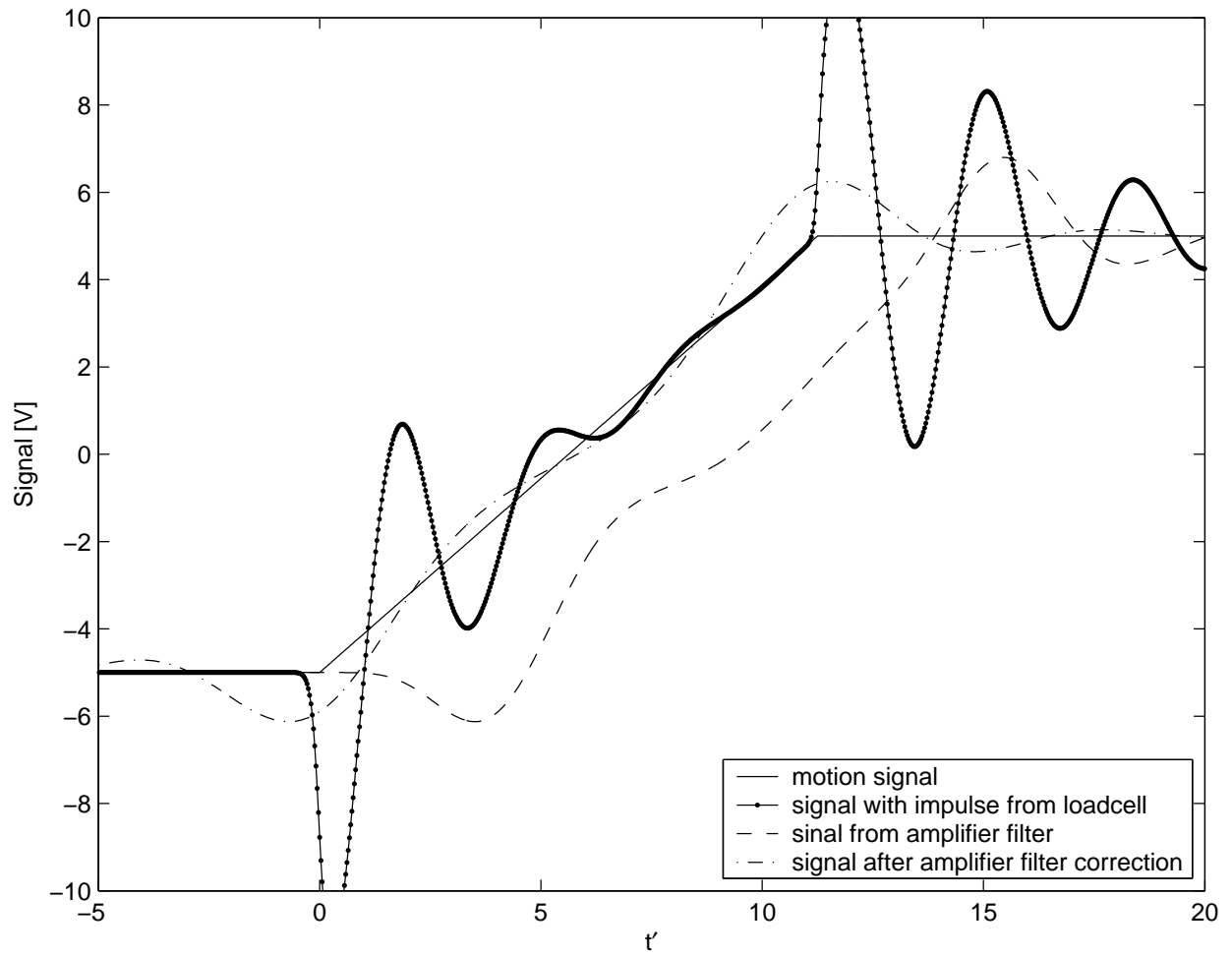
Figure 3.6: Example of how a loadcell electric signal is modified during the various filtering stages
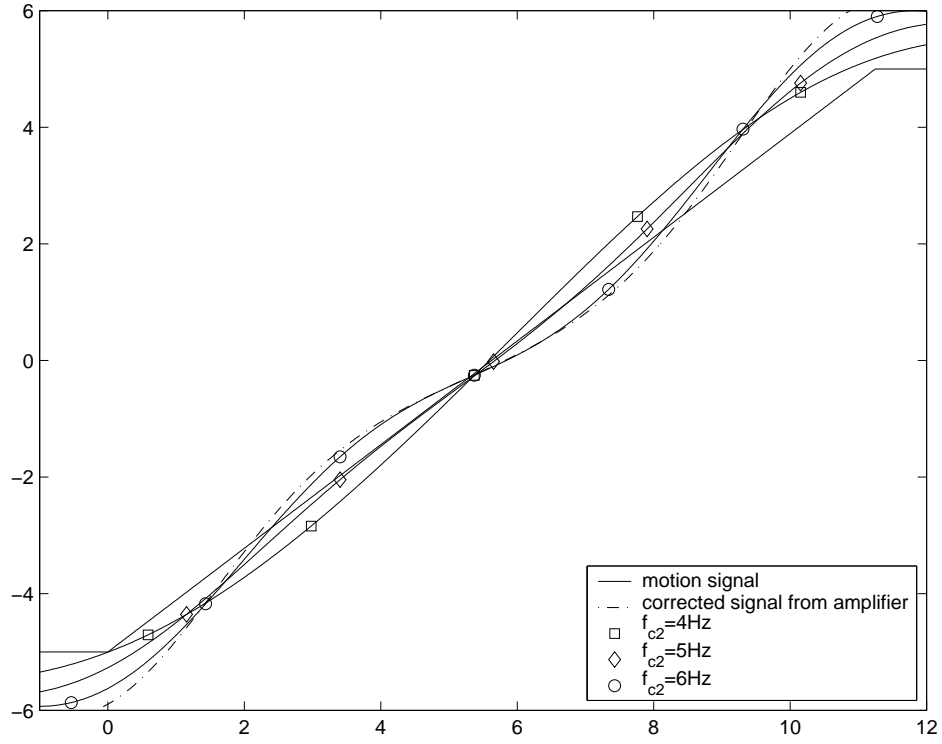
Figure 3.7: Loadcell signal effect on variation on second filtering frequency

of the presence of the impulse noise there. If the cutoff frequency of the second filtering is reduced to $4Hz$, the initial and end parts of the signal approach the correct magnitudes. However, the middle part of the motion now shows an incorrect slope.

Chapter 4

Experimental results

Experimentally obtained data are presented in figures with mean values and 95% confidence limit (or 20:1 odds) uncertainties calculated according to Granlund [41]. Reduced data are corrected in pitch angle position to have zero force and moment at zero angle for the symmetric ellipsoid and Suboff barebody geometries. Since there are non-uniform flow in the test section, reduced data are also corrected with a $\psi = -2°$ roll angle that minimizes the out-of-plane forces and moments. All data are taken at $Re = 2.8 \cdot 10^6$ per meter. Steady data are taken with 1° increment for $-26° < \theta < 26°$ with additional 0.5° increments near $5° < |\theta| < 8°$ to reliably identify linear and quadratic regions. Steady data are recorded for 10 seconds at $f_s = 1kHz$ and unsteady maneuvers are repeated 20 times to reduce measurement uncertainties.

4.1 Ellipsoid steady data

4.1.1 Angle of Attack

From Figure 4.1 one can observe that for small translation velocities (or angles of attack), $|\alpha| < 5°$ or $w' = sin(\alpha) < 0.09$, there is a linear response of the normal force Z' according to Equation 4.1. In this region, the flow is believed to be completely attached without cross-flow separation according to Allen and Perkins [5] and computations by Bensow [7].
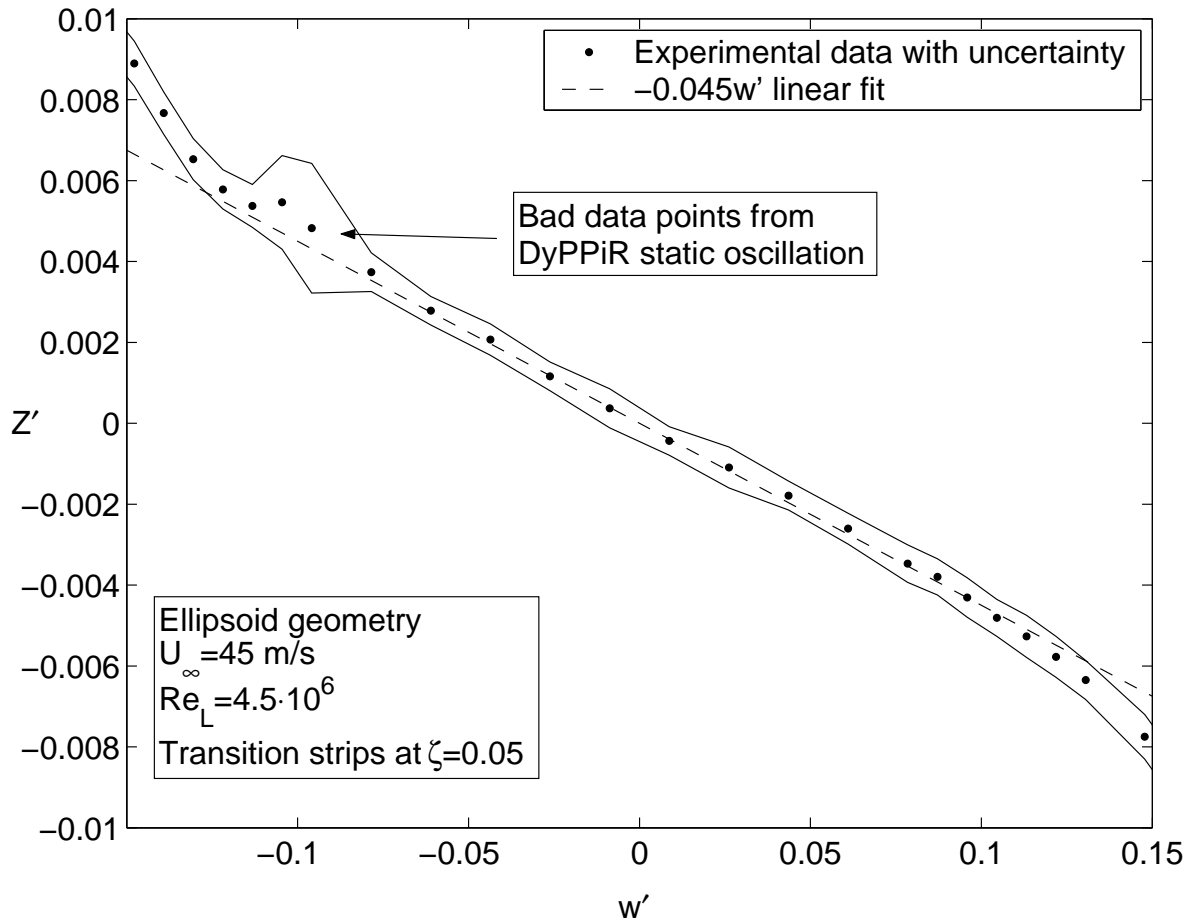
Figure 4.1: Ellipsoid linear fit to normal force

$$Z'_{att} = -0.045w' \tag{4.1}$$

73

For larger translation velocities $|w'| > 0.09$ the response in Figure 4.2 is quadratic according to Equation 4.2.
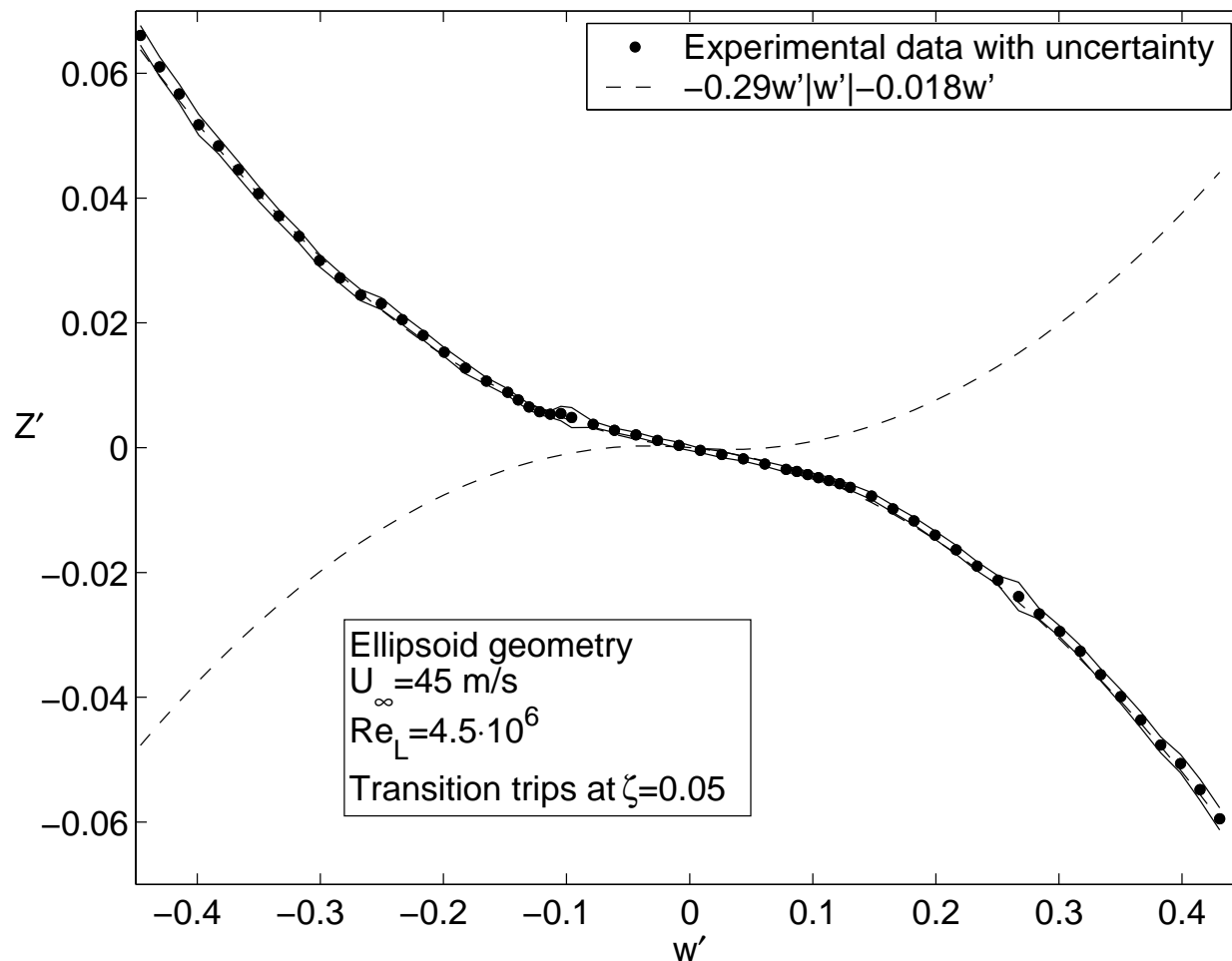
Figure 4.2: Ellipsoid quadratic fit to normal force

$$Z'_{vor} = -0.29w'|w'| - 0.018 \tag{4.2}$$

Since cross-flow separation and vortical lift do not occur until the pressure gradient is adverse enough from an angle of attack of the body, we have to use a function that 'turns on' at a certain angle of attack. In order to have a function that approximates linear propor-

tionality at low angles and quadratic at higher angles, an approximate $tanh(w')$ function in Equation 4.3 is used where $k \approx -100$ depending on the sharpness of the 'knee' between the two piecewise polynomials. The linear positive part that appears with the quadratic part is the reduction in attached lift from the small angle linear proportionality.
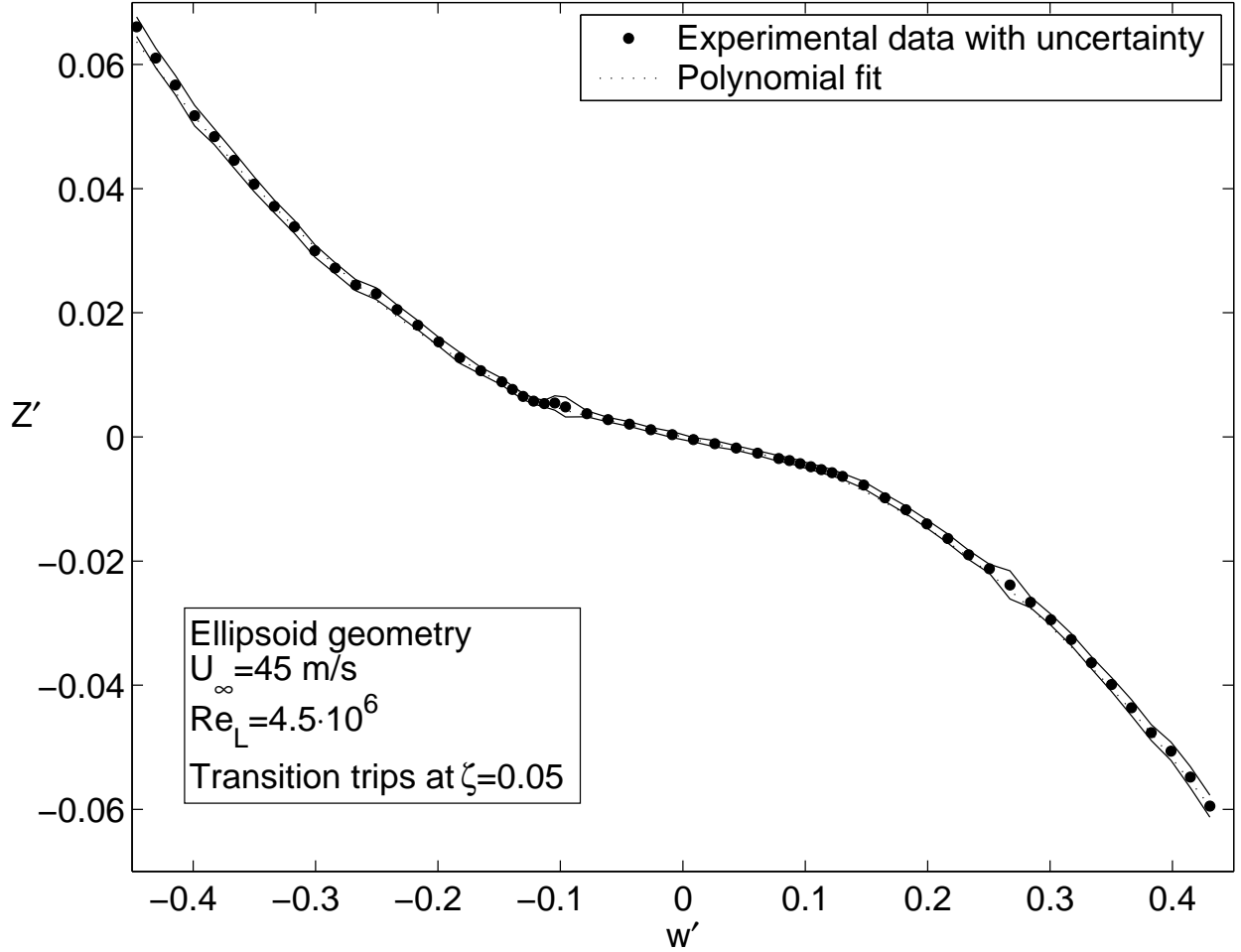
Figure 4.3: Ellipsoid normal force

$$Z' = Z'_{att} + Z'_{vor} = -0.045w' + \frac{1}{1 + exp(-k|w'| - 0.09)}(0.29w'|w'| + 0.027w') \qquad (4.3)$$

The results by Bensow [7] indicate a smoother transition between the fully attached flow and the advent of cross-flow separation than what experiments do in Figure 4.3. The difference between the experiments and the computations is probably due to the centerline sting which could be affecting the flow at small angles of attack and cause a different separation than what the geometry would do without the sting. If the exponential 'switching on' part is not used as in Equation 4.4, there will be a significant difference in predicted versus measured normal force for small angles as in Figure 4.4.
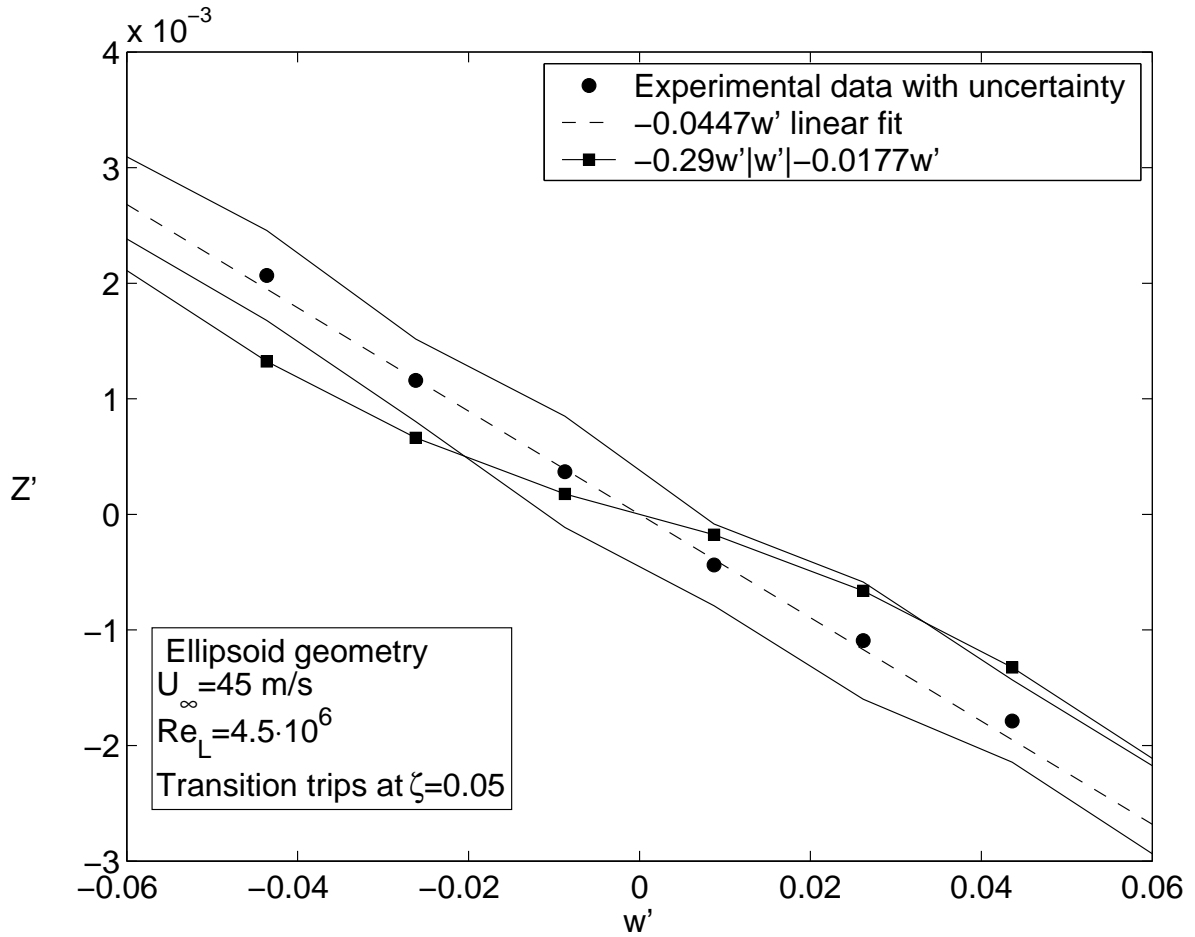
Figure 4.4: Ellipsoid normal force with wrong linear fit

$$Z' = -0.045w' - 0.29w'|w'| + 0.027w' = -0.018w' - 0.29w'|w'| \qquad (4.4)$$

The same observation for the pitching moment can be observed in Figures 4.5 where the response is also linear as in Equation 4.5. This behavior is explained by the CFD simulations by Bensow [7] where for $\alpha < |5°|$ there are no lee side vortices and the flow is fully attached.
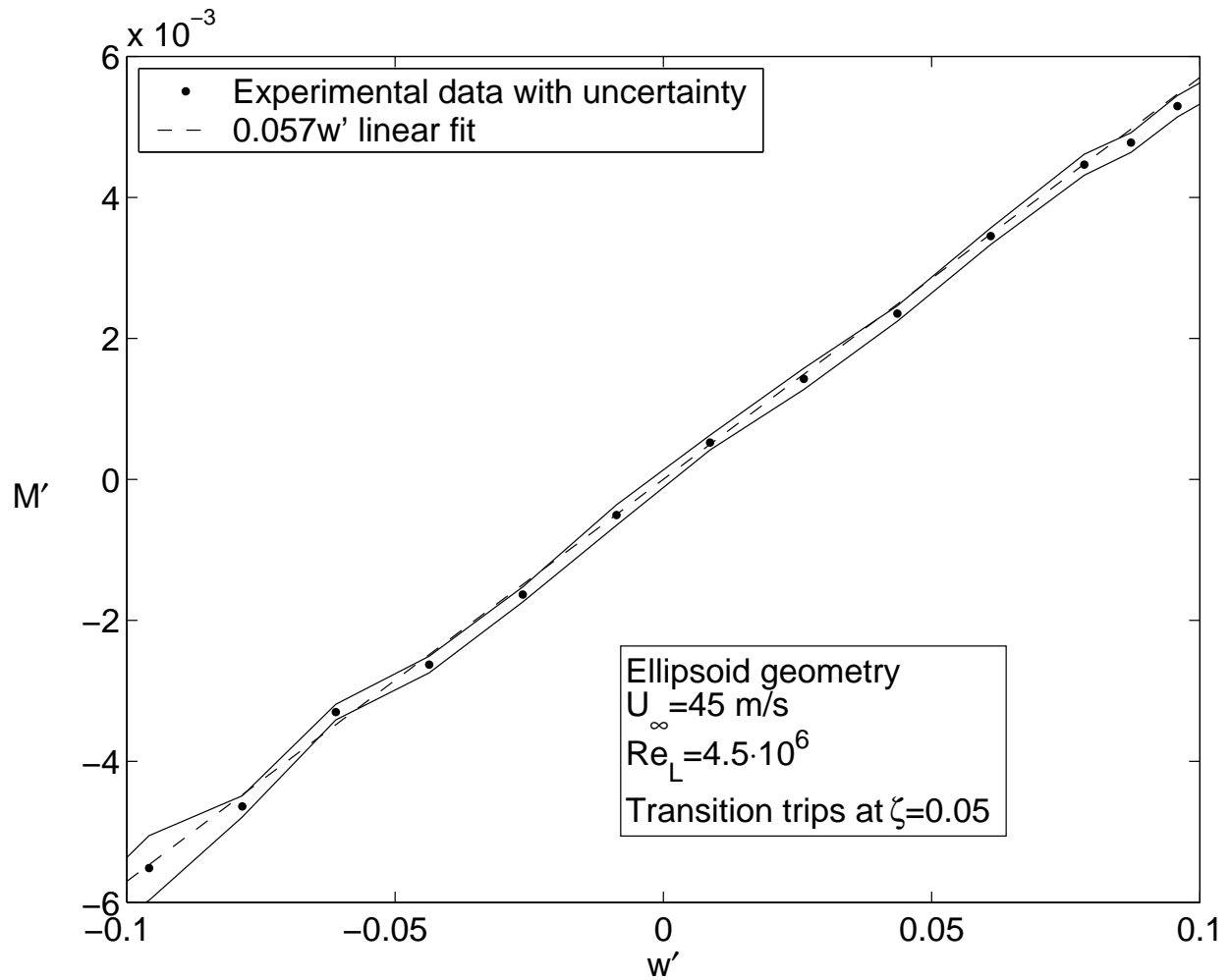
Figure 4.5: Linear fit to pitching moment

$$M'_{att} = 0.057w' \tag{4.5}$$

For higher angles of attack, the pressure gradient from the normal velocity becomes high enough to invoke cross-flow separation starting from the stern. The question here is exactly how this cross-flow separation vortical lift is distributed. At some point upstream on the body, there is no separation, as shown by Hosder [49]. The separation also grows from the stern, indicating that lift forces would be distributed increasing from zero somewhere on the midbody to maximum on the stern. The simplest function is a linearly increasing lift from zero at $\zeta = 0.5$ to max at $\zeta = 1$. The center of pressure from the vortical lift is then at $\zeta_{vor} = 5/6 = 0.833$.

$$
\begin{aligned}
M' &= M'_{att} + M'_{vor} = 0.057w' + (\zeta_{vor} - \zeta_M)\frac{Z'_{vor}}{1 + exp(-k|w'| - 0.09)} \\
&= 0.057w' + \frac{1}{1 + exp(-k|w'| - 0.09)}(-0.105w'|w'| + 0.00945w')
\end{aligned}
\tag{4.6}
$$

Figure 4.6 shows that, with a small modification in vortical lift center of pressure, the polynomial approximations of the normal force and pitching moment agree to within the experimental measurement uncertainties.
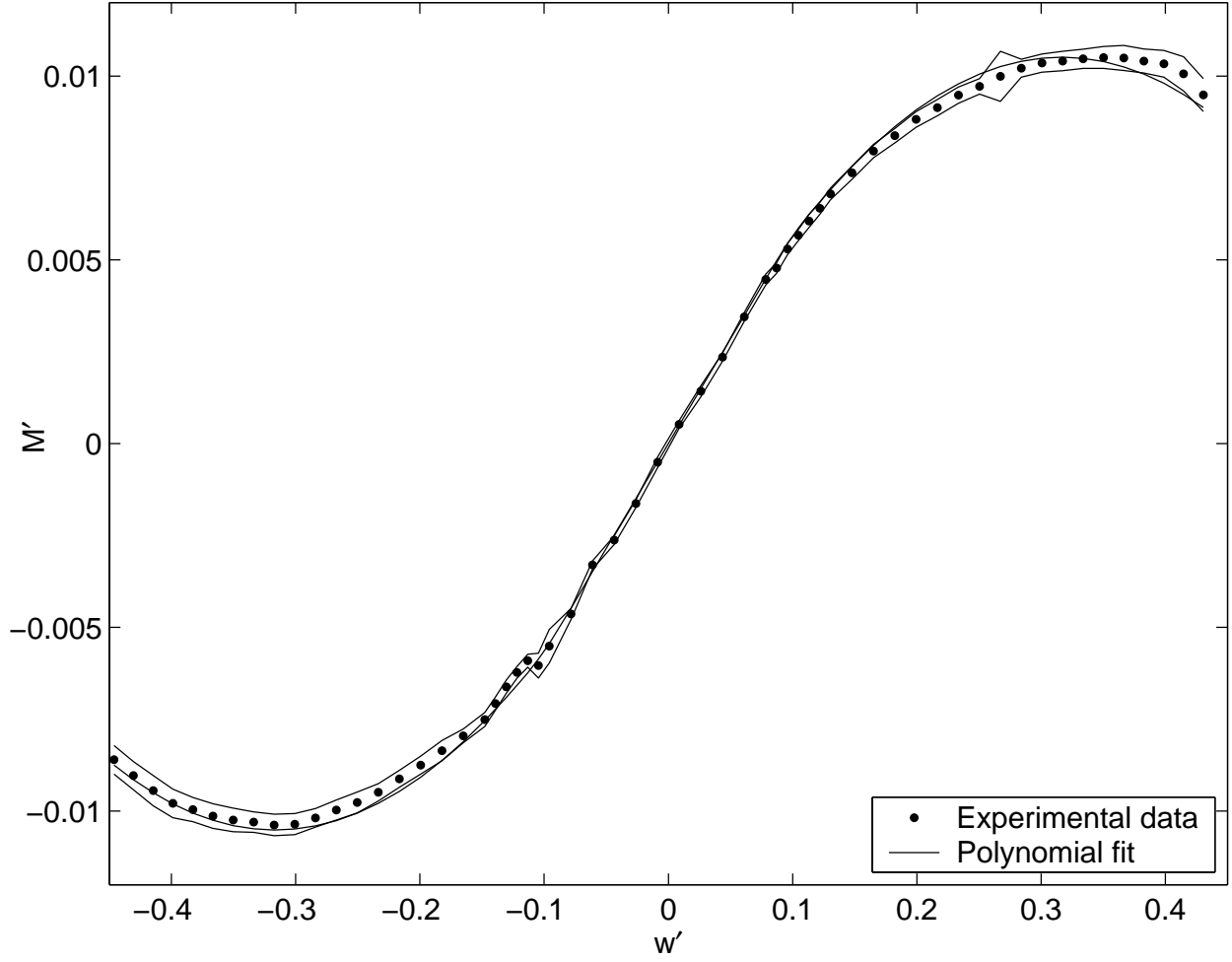
Figure 4.6: Ellipsoid pitching moment

4.1.2 Center of pressure

$$\zeta_{cp} = \zeta_M + \frac{M'}{Z\prime} = 0.5 + \frac{0.057}{-0.0447} = -0.775 \tag{4.7}$$

According to Equation 4.7 the center of pressure for the linear response, attached flow, the center of pressure is in front of the bow making it very unstable in pitch. It comes from the fact that the center of pressure for the lee side is on the front half of the body and on the

rear half for the windward side.

$$\zeta_{cp} = 0.5 + \frac{-0.105w'|w'| + 0.665}{-0.3w'|w'| - 0.018} \tag{4.8}$$

For the case when crossflow separation exists, lift is being produced mainly from the aft part of the body. This moves the center of pressure on the lee side of the body aft and gradually limits the unstable pitching moment as evident in Figure 4.7. This is also supported by the results by Allen and Perkins [5] that show a more aft position of the center of pressure for slender bodies at higher angles of attack.
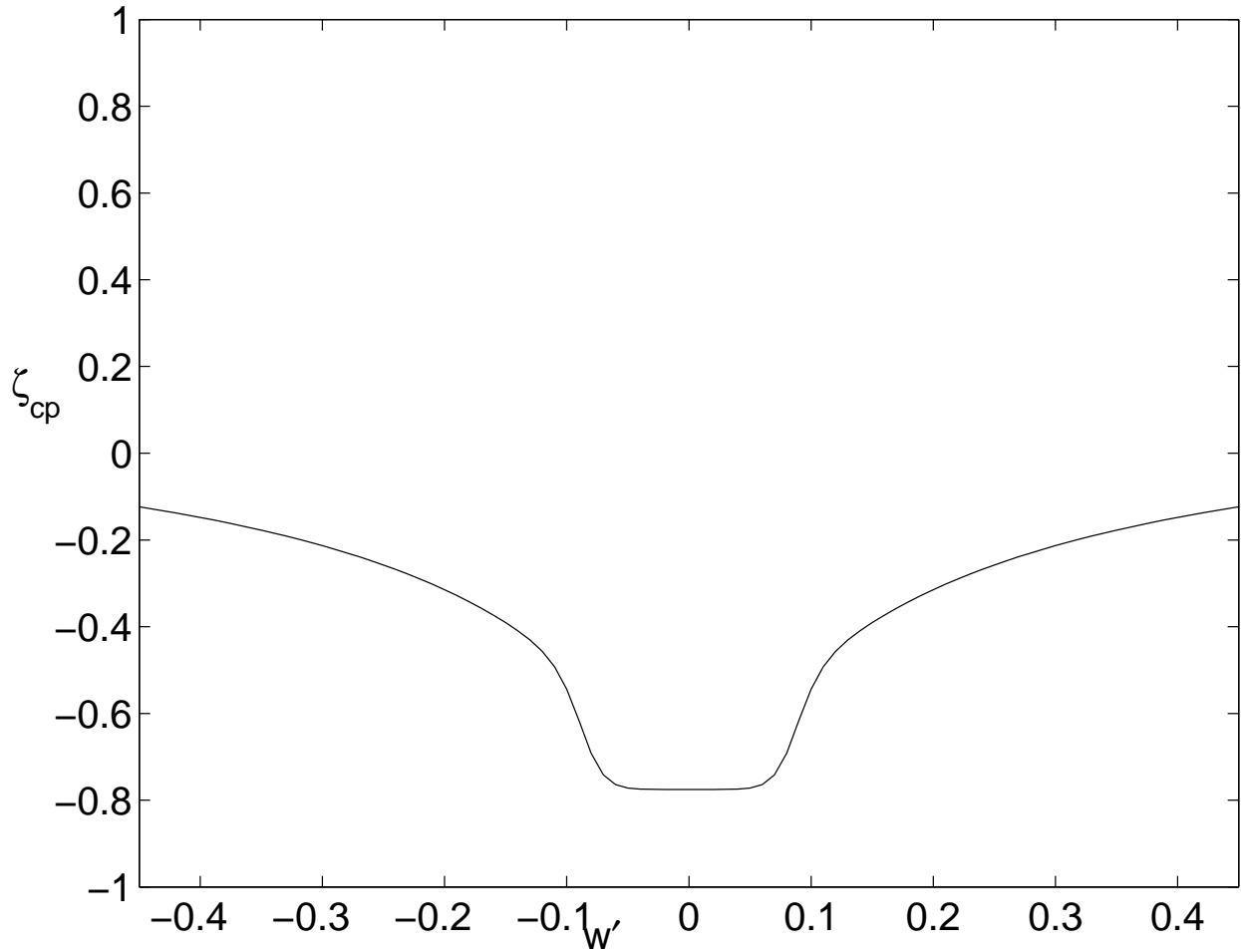
Figure 4.7: Ellipsoid vertical center of pressure

4.1.3 Sideslip

For smaller angles of sideslip, $|\beta| < 3.5°$ or $v' = sin(\beta) < 0.06$, the flow is believed to be completely attached. However, the uncertainties in side force measurement in Figure 4.8 prevents making any certain fit of data. Since the uncertainty limits incorporate $Y' = 0$, for symmetry of data (of a symmetric body), this will be used.
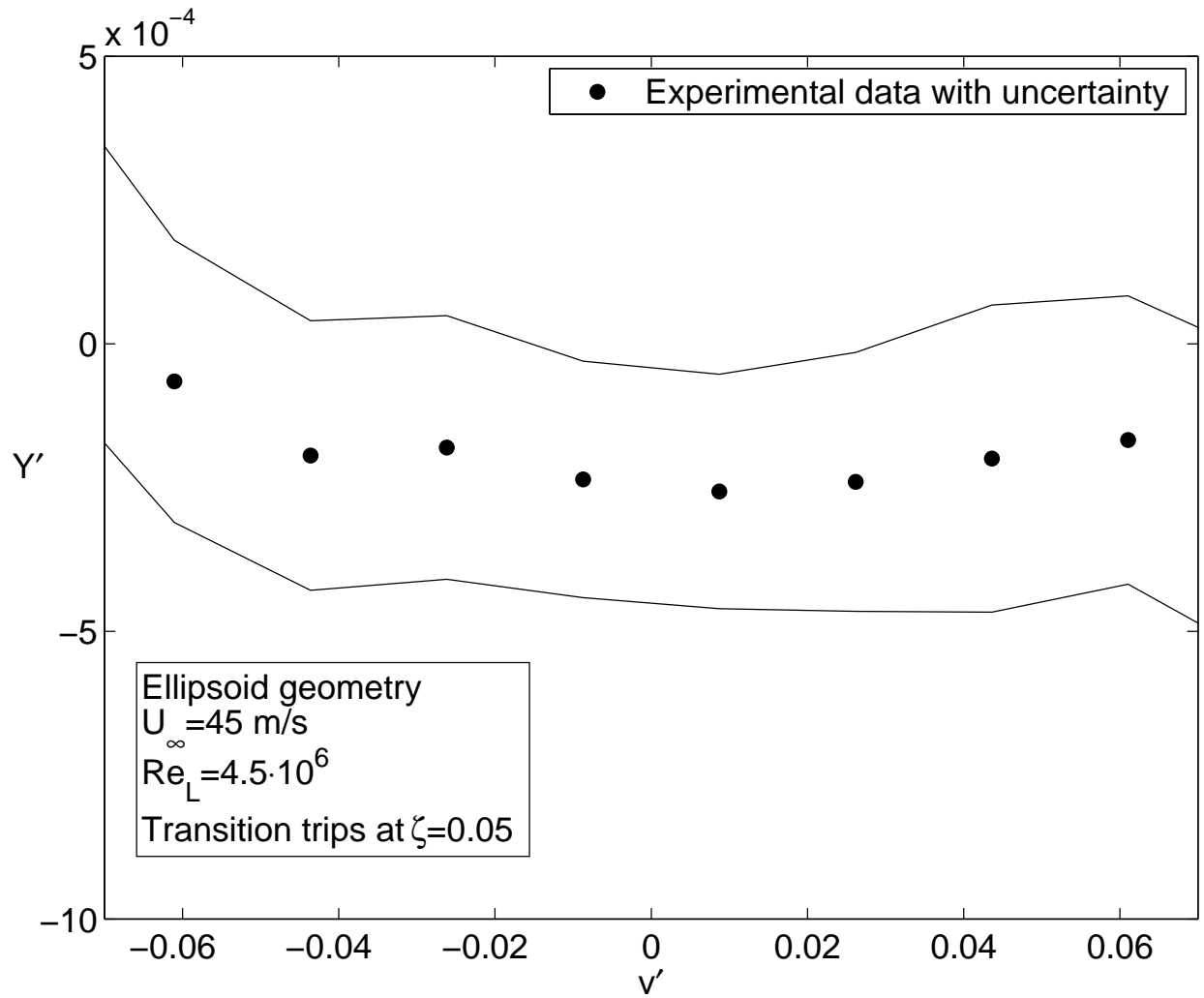
Figure 4.8: Ellipsoid linear fit to yaw force

From Figure 4.9 one can observe the same quadratic dependency of yaw force Y' on sway v' as the normal force Z' on heave w' in Figure 4.2.
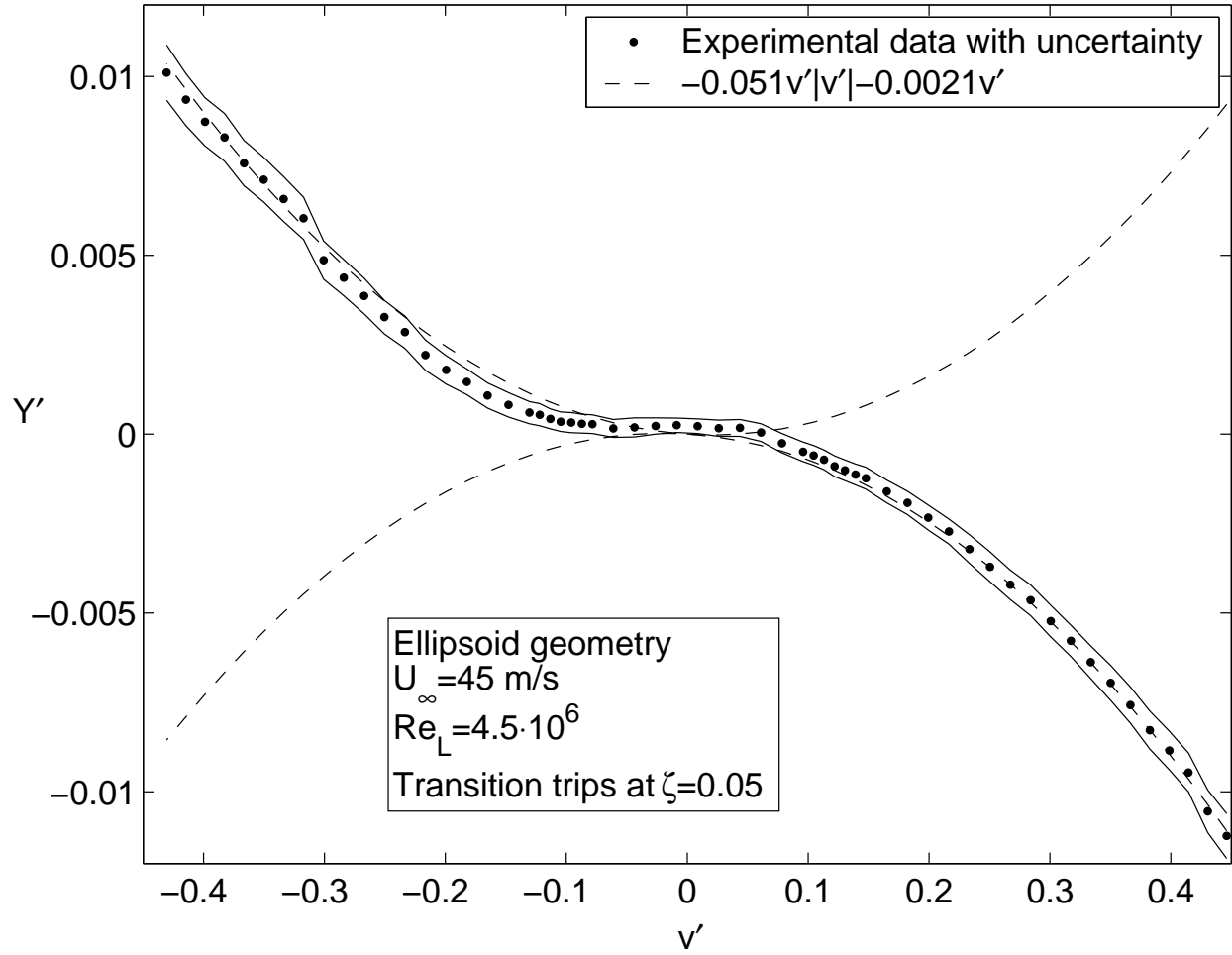
Figure 4.9: Ellipsoid quadratic fit to yaw force

Due to the oval cross section, cross-flow from a sideslip will encounter a separation triggering adverse pressure gradient at a smaller angle than from an angle of attack. The function for the yaw force Y' on sway v' is then

$$Y' = \frac{1}{1 + exp(-k|v'| - 0.06)}(-0.053v'|v'| + 0.0021v')$$ (4.9)

where $k \approx -100$.
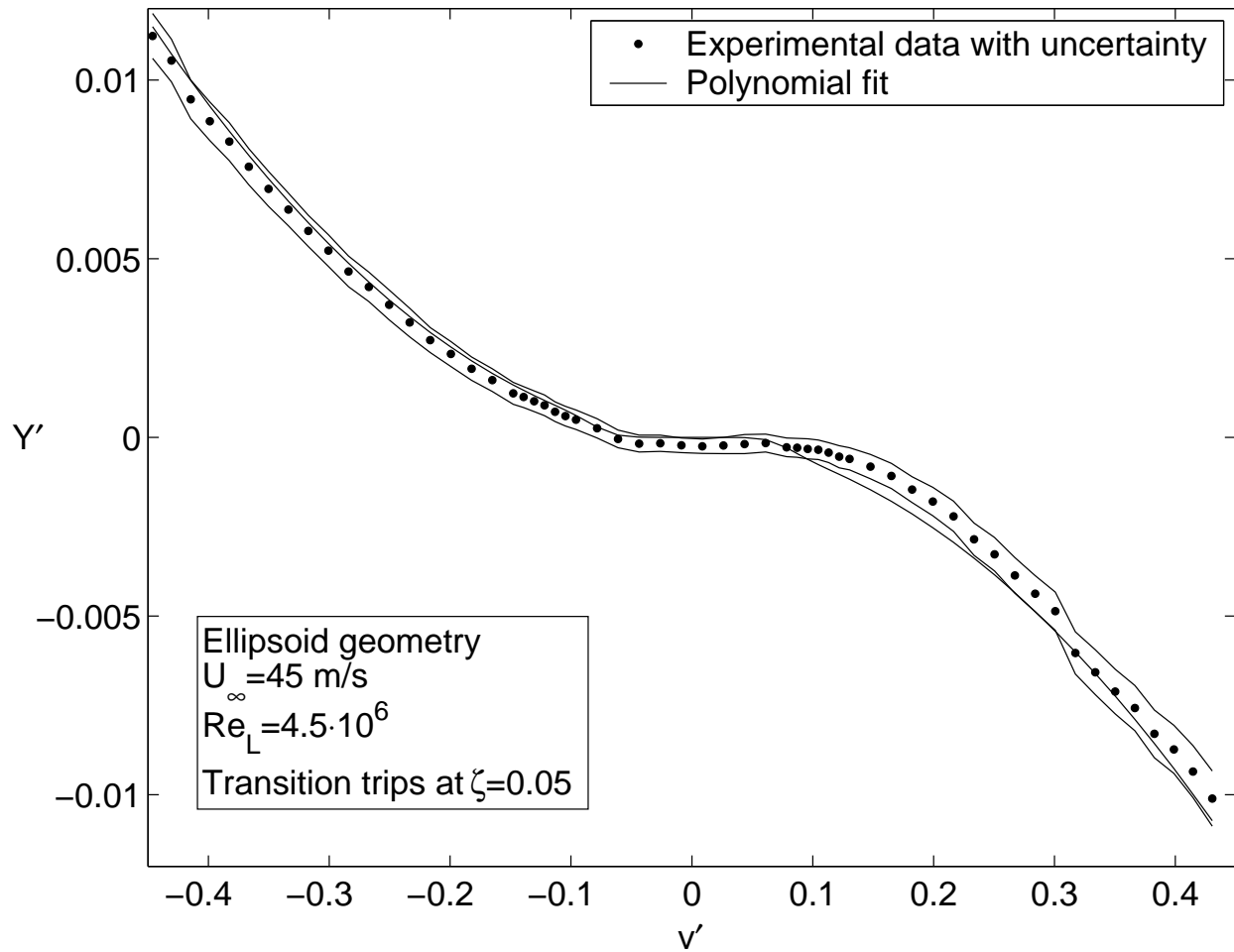
Figure 4.10: Ellipsoid side force

The same observation for the yaw moment, as for pitching moment, can be observed in Figures 4.11. The yaw moment is destabilizing since a sideslip angle will produce a yaw moment that increases the sideslip angle.
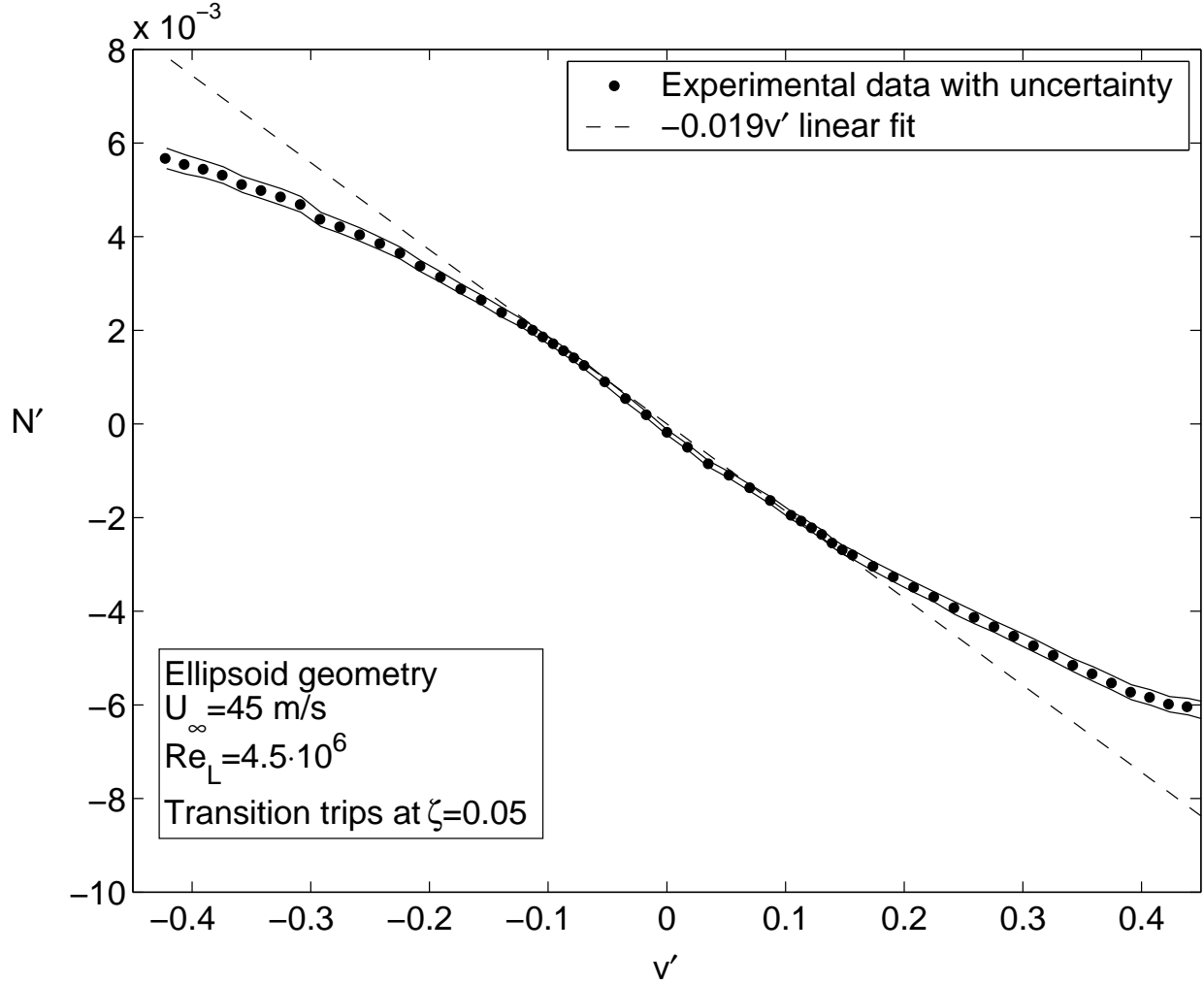
Figure 4.11: Linear fit to yawing moment

The linear approximation of the pitching moment for small angles is

$$N'_{att} = -0.019v' \tag{4.10}$$

For larger sideslip angles, the pressure gradient from the normal velocity becomes large enough to invoke cross-flow separation starting from the stern the same way as for angle of attack. The vortical force contribution is done the same way for the normal force. Figure 4.12 shows that, with vortical lift center of pressure to $\zeta_{vor} = 0.76$, the polynomial approximations of the normal force and pitching moment agree to within the experimental measurement uncertainties.

$$
\begin{aligned}
N' &= -0.019v' + (\zeta_{vor} - \zeta_M)\frac{Y'_{vor}}{1 + exp(-k|v'| - 0.06)} \\
&= -0.019v' + 0.26\frac{0.053v'|v'| - 0.0021v\prime}{1 + exp(-k|v'| - 0.06)}
\end{aligned}
\tag{4.11}
$$
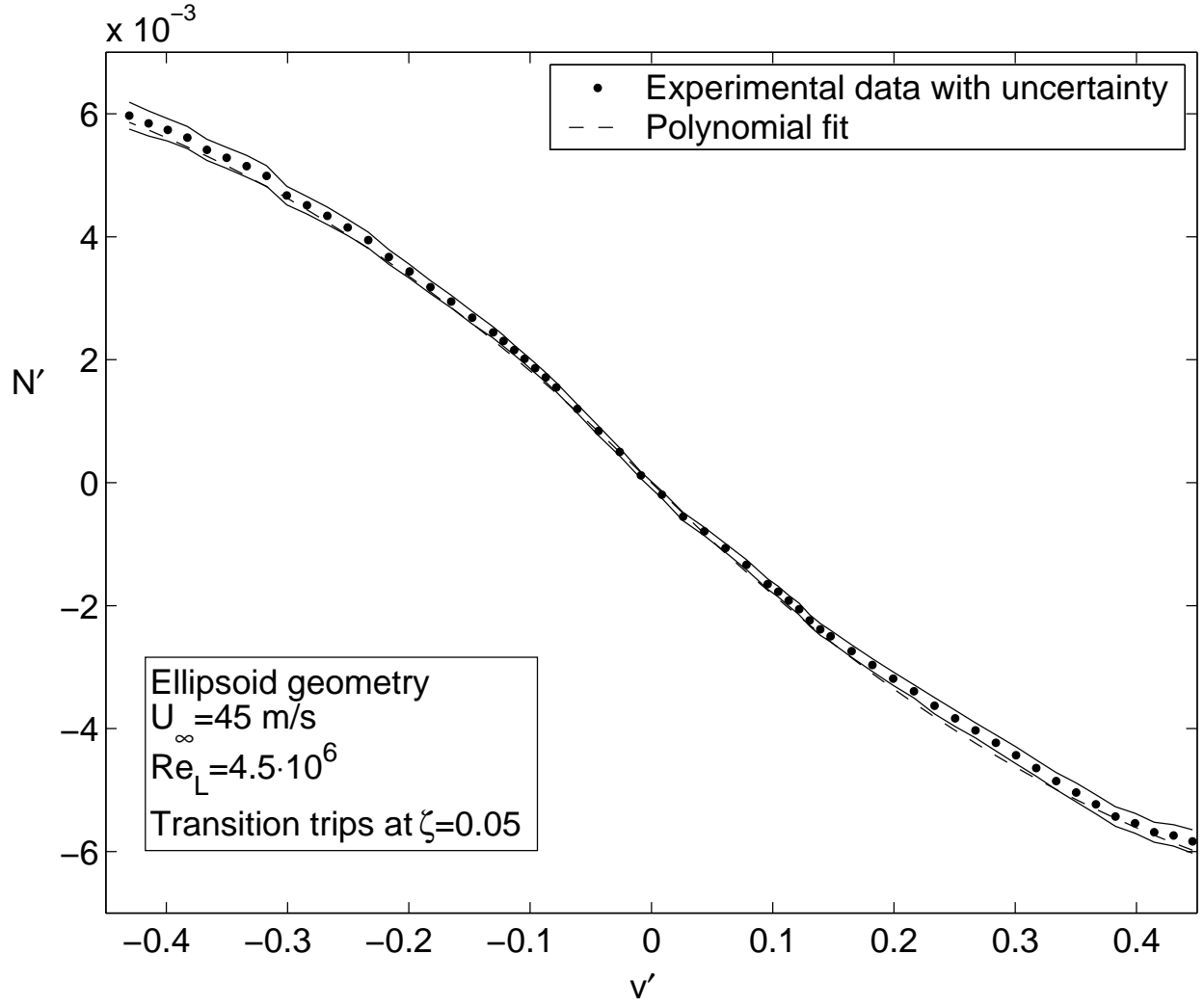
Figure 4.12: Ellipsoid yaw moment

4.1.4 Potential flow slender body theory results

From Karamcheti [52], one can use slender body theory to predict the normal force and pitch moment for small angles

$$Z' = \frac{Z2sin\alpha}{q_\infty L^2} = \frac{-2q_\infty w'}{q_\infty L^2}\int_0^L \frac{dS}{dx}dx = Z'_w w' \tag{4.12}$$

$$M' = \frac{-2q_\infty w'}{L^3}\int_0^L (x-0.8)dS = M'_w w' \tag{4.13}$$

Since a closed body in potential flow without circulation does not produce any lift, we end the integration prematurely at a location in the stern where the flow will undergo separation. The exact location of the stern separation cannot easily be determined. It cannot be further upstream than where the stern meets the constant cross section since separation occurs in adverse pressure gradients where the cross section area is reduced. The body is also suspended with a $3in.$ sting on the centerline through a hole with an approximately $4in.$ diameter. The bounds for the separation are therefore

$$0.75 < \zeta_{sep} < \frac{1}{1.6}\left(1.2 + \sqrt{1 - \left(\frac{0.0254 \cdot 2}{0.2}\right)^2}\right) = 0.99 \tag{4.14}$$

When using these limits in the sender body theory equations, the normal force and pitch moment coefficients vary between

$$-0.098 < \quad Z'_w \quad < -0.0061 \tag{4.15}$$

$$0.0102 < \quad M'_w \quad < 0.0152 \tag{4.16}$$

with the smaller values corresponding to the separation location at $\zeta_s = 0.75$ and the larger values corresponding to $\zeta_s = 0.99$. The measured $Z'_w = -0.045$ is within the bounds of the computational result, but the measured pitch moment $M'_w = 0.057$ is almost three times greater than the possible maximum. The most likely reason for the difference in pitch moment is the fact that slender body theory, as well as thin airfoil theory, are based on the assumptions on small disturbances and therefore small changes in body area difference and airfoil thickness. This is not valid at the bow for blunt bodies and the leading edge for airfoils where the greatest influence on pitch moment is generated. Therefore, this method should not be used to predict the pitch moment.

4.1.5 Combination of Angle of Attack and Sideslip

An angle sweep from $-26° < \theta < 26°$ with a roll angle of $\phi = 80°$ was also tested in order to see any evidence of curvature discontinuities in the force and moment response plots Figure 4.13 to 4.17. Any discontinuities would be an indication of bifurcation instabilities for motions. However, the figures indicate near perfect symmetrical or antisymmetrical curves. In Figure 4.13 and 4.14 we can observe that the angle span of the linear relationship of side- and normal force to the pitch angle appears to be larger than for the case when the roll angle is zero in Figure 4.3 and 4.10.
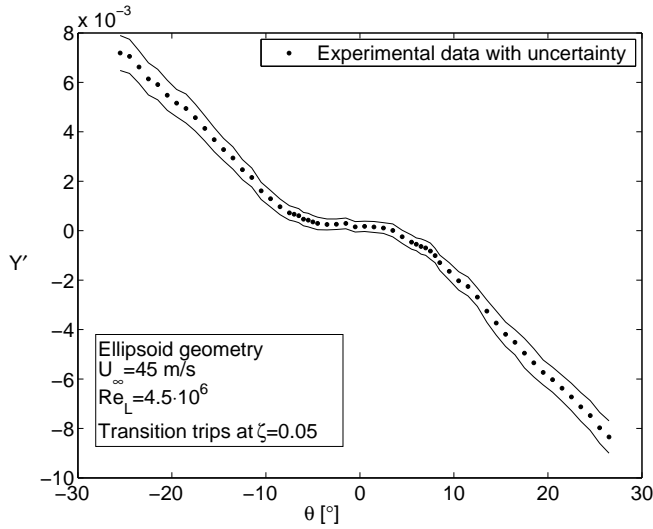
Figure 4.13: Side force at 10° roll angle   Figure 4.14: Normal force at 10° roll angle
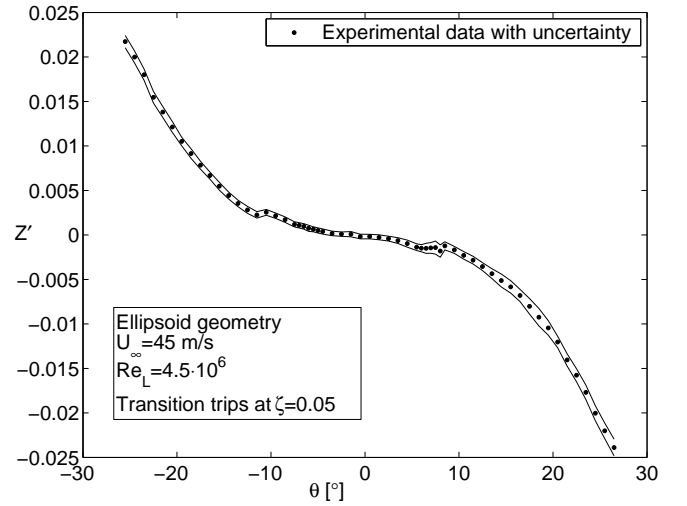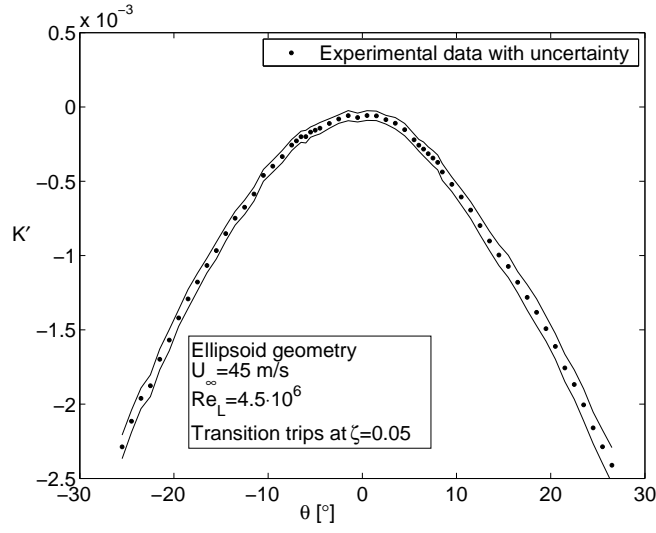
Figure 4.15: Roll moment at 10° roll angle
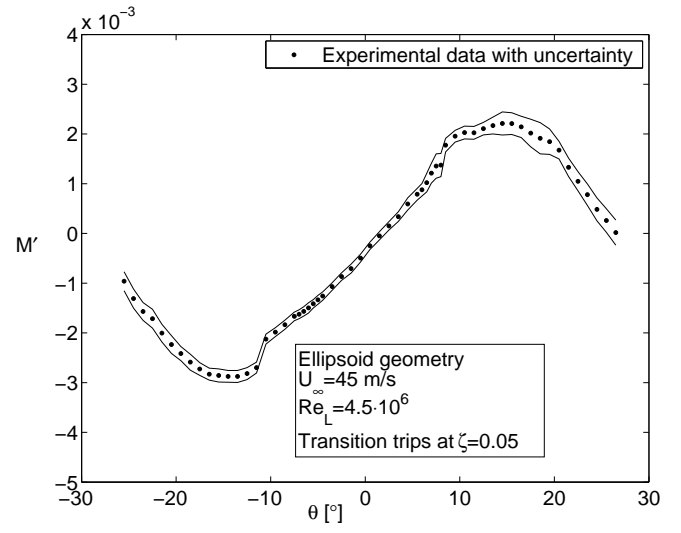
Figure 4.16: Pitching moment at 10° roll angle
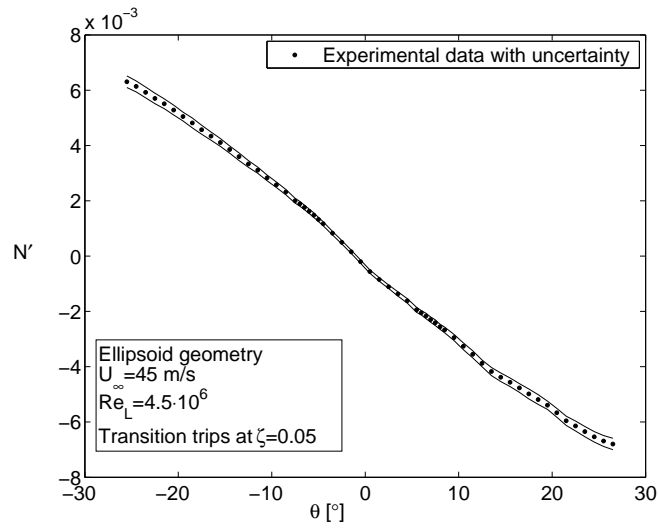
Figure 4.17: Yaw moment at 10° roll angle

When plotting the forces with respect to the non-dimensional body-coordinates instead, one can observe in Figure 4.18 and Figure 4.20 that the side force Y' reaches maximum magnitude at pure sway velocity v' with heave velocity $w' = 0$. A slight roll angle of $\phi = 80°$ from a pure sideslip reduces the side force Y'. Figure 4.18 includes the $\phi = 80°$ roll angle data points that are also duplicated for $\phi = 100°$ data points (since the body is symmetric). The slight assymmetry of the $v' = 0$ line is believed to be from the non-uniformity of the freestream.

$$v' = \sin\phi \sin\theta \tag{4.17}$$
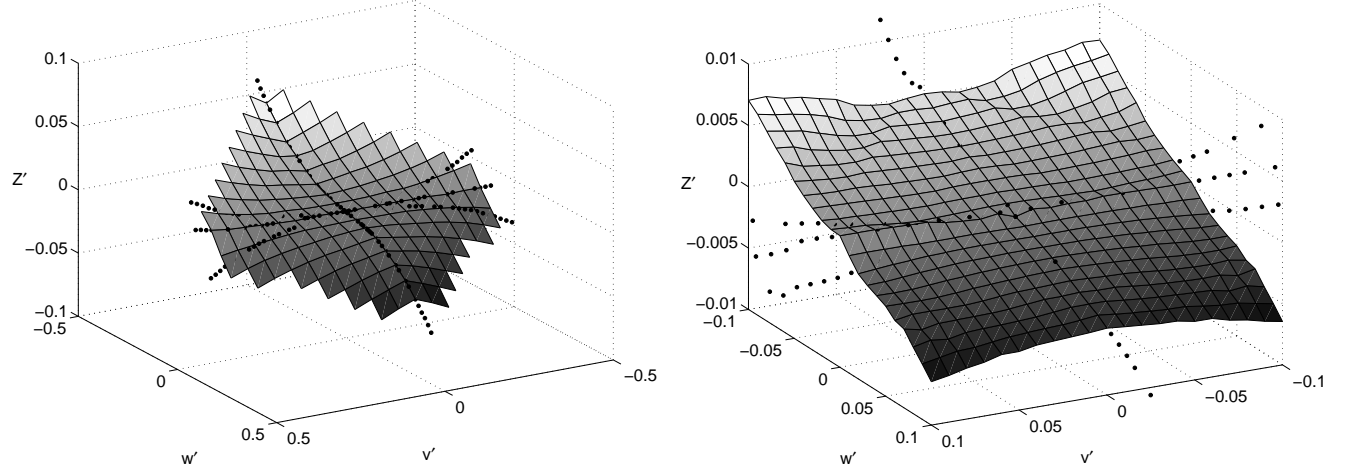
$$w' = \cos\phi \sin\theta \tag{4.18}$$
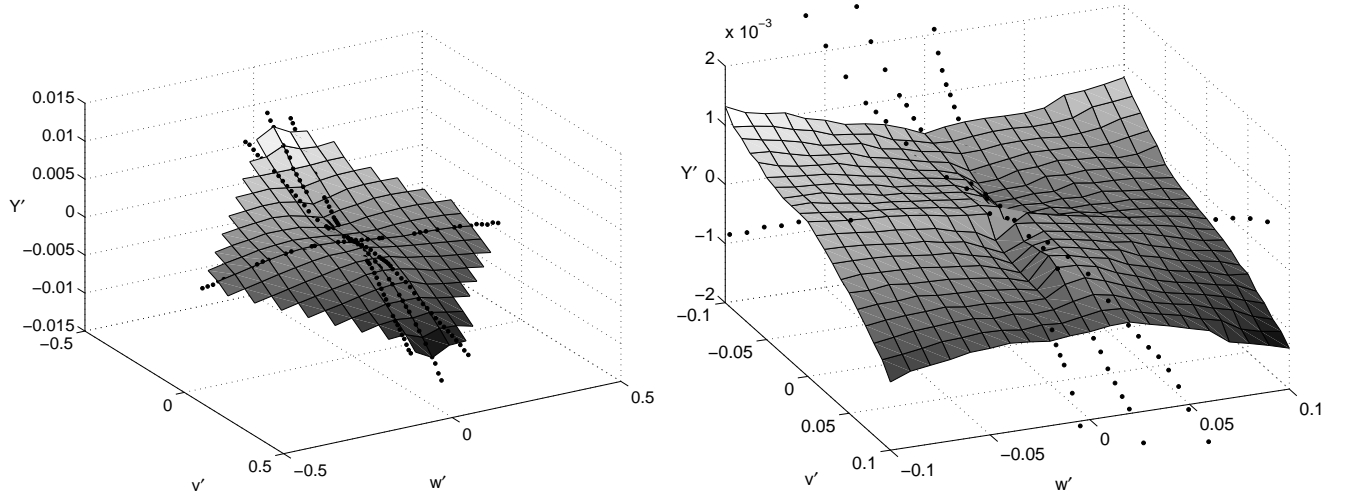
Figure 4.18: Side force at combinations of normal and transversal velocities

The side force Y' reduces in magnitude at sideslip angles when a small angle of attack is included as seen in Figure 4.18. Figure 4.19 shows how the coefficient $Y'_{|w|}$, calculated in Equation 4.19, varies over a range of v' and is near constant for $0.15 < v' < 0.45$. At smaller $v' < |0.1|$ the coefficient rapidly approaches zero since there are no cross-flow separation vortices.

$$Y'_{|w|} = \frac{Y'|_{w'=0} - Y'|_{\phi=80°}}{|w'|} = -0.085 \tag{4.19}$$
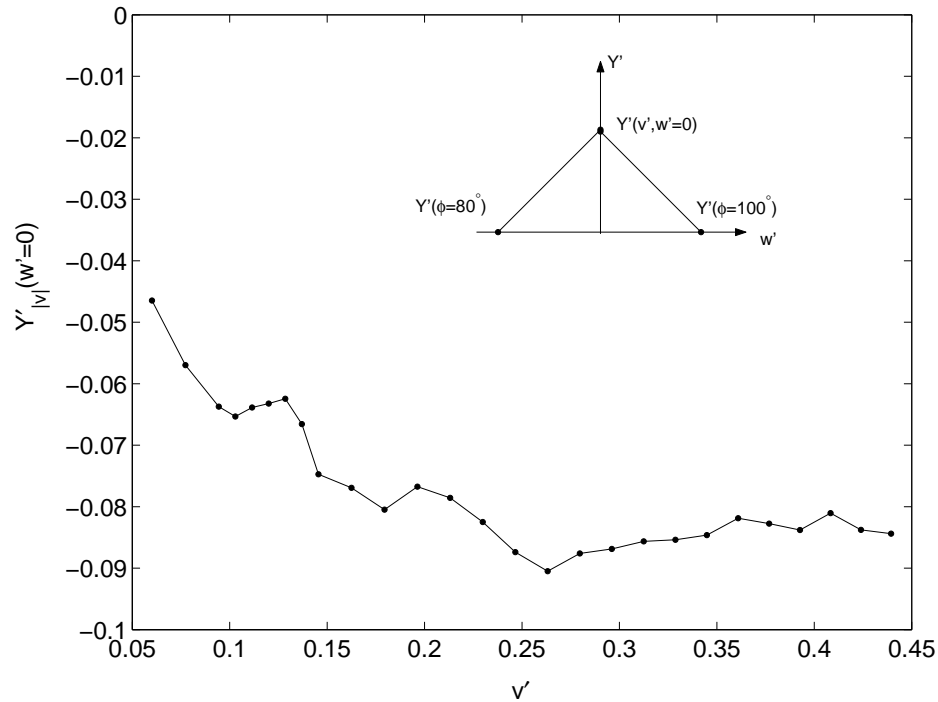
Figure 4.19: Side force coefficient as function of $|w'|$ at a range of v'

Since the data are interpolated for other roll angles the figures can therefore not reliably be seen to illustrate the forces and moments where the magnitude of v' and w' are roughly equal.

The normal force Z' in Figure 4.20 increases in magnitude at a combination of larger sway velocity v' and small heave velocity w' according to the data points.

Figure 4.20: Normal force at combinations of normal and transversal velocities

The normal force Z' increases in magnitude at sideslip angles when a small angle of attack is included as seen in Figure 4.20. Figure 4.21 shows how the coefficient $Z'_{\sqrt{v}w^2}$ varies over a range of v' and is near constant for $0.15 < v' < 0.45$. At smaller $v' < |0.15|$, the coefficient rapidly approaches infinity because of the difficulty of numerically determining any derivatives there.

$$Z'_{\sqrt{v}w^2} = -5.5 \tag{4.20}$$

92
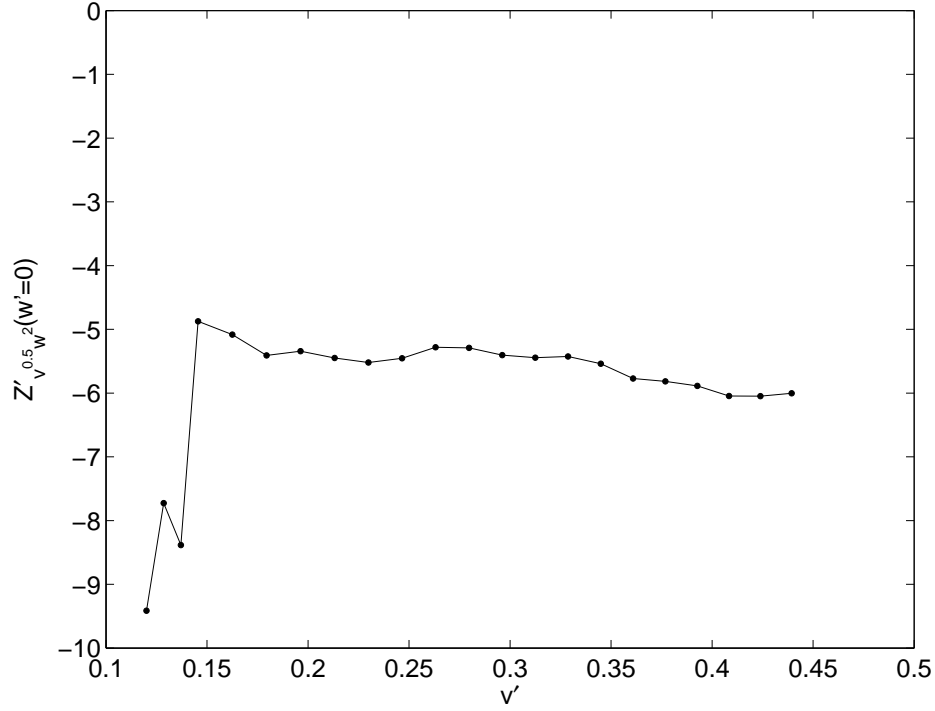
Figure 4.21: Side force coefficient derivative at a range of v'

Since there does not exist data for other roll angles than $\psi = 80°$, not very much more can be said about how the normal force behaves at combinations of both large heave w' and sway v' velocities.

The rolling moment K' in Figure 4.22 is obviously zero at pure sideslip or angle of attack and some value for a combination of both. From the data at a small roll angle of $\psi = 80°$ away from a pure sideslip, the rolling moment has a large gradient and is very sentitive to small angles of attack. A state of pitched up and yawed left giving positive v' and w' produces a negative rolling moment K' to increase the yawing and pitching. The rolling moment coefficient derivative in Equation 4.21 is constant for $v' > |0.06|$. With only one roll angle tested, nothing can be said if the hydrodynamic derivative is still constant for large heave w' and sway v' velocities.

$$K'_{v^{0.5}w} = \frac{K'}{\sqrt{v'w'}} = -0.045 \qquad (4.21)$$
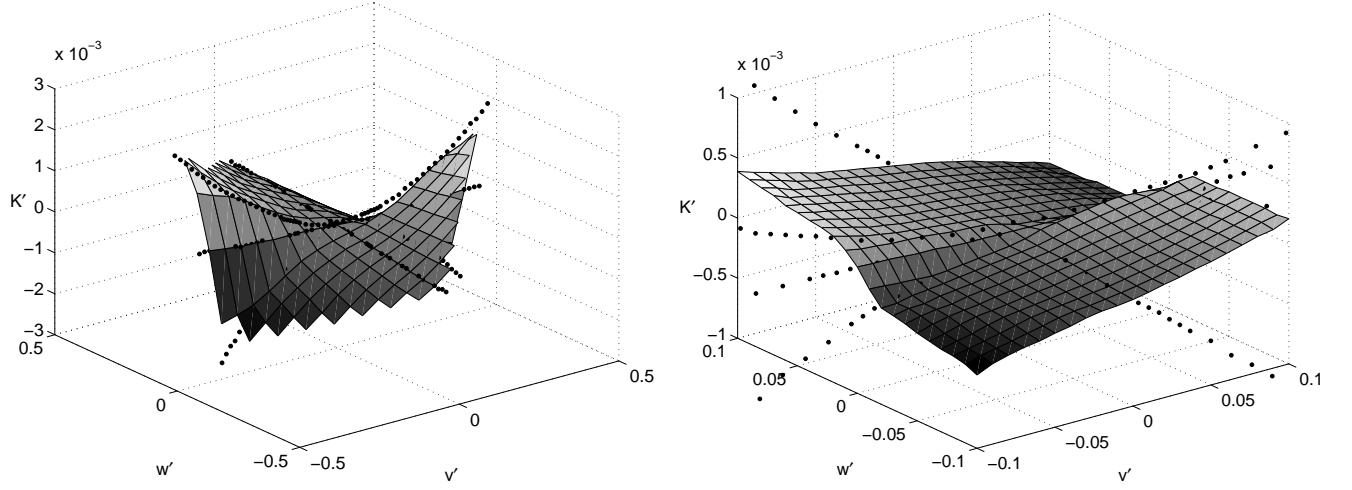
Figure 4.22: Rolling moment at combinations of normal and transversal velocities
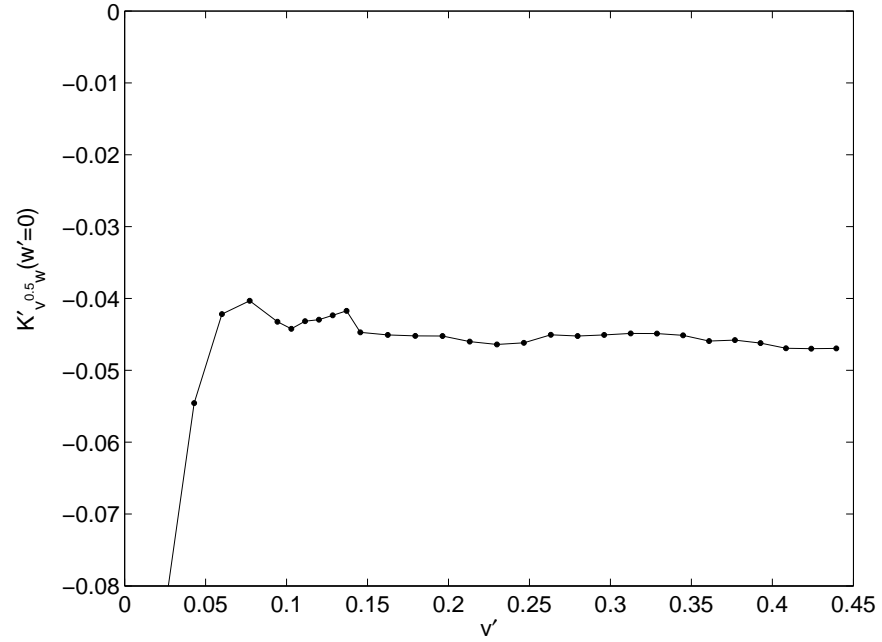
Figure 4.23: Rolling moment coefficient derivative at a range of v'

The pitching moment M' in Figure 4.24 is reduced a great amount when inducing a small amount of sideslip at the same time as the angle of attack is large enough to invoke cross-flow separation.
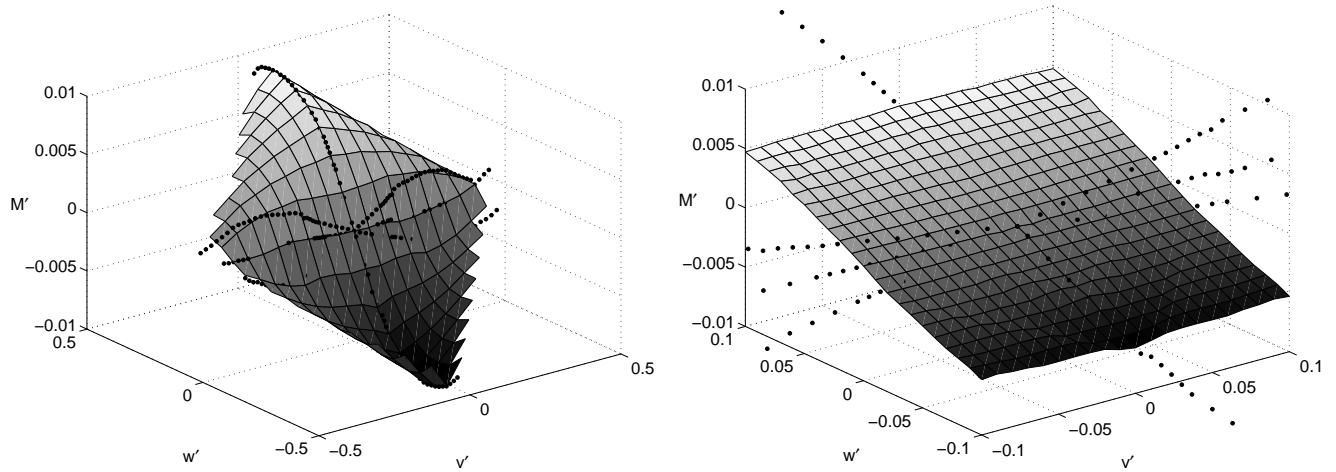

Figure 4.24: Pitching moment at combinations of normal and transversal velocities

The yawing moment N' in Figure 4.25 increases slighly in magnitude with a small angle of attack while at a large sideslip. Since the yawing moment is zero at pure angle of attack, the interpolation will not give any information for combinations of large heave w' and sway v' velocities. No large discontinuities in slope can be observed for small v' and w' in the right hand plots that already do not appear for larger v' and w'. Several more roll angles need to be tested in order to better give an explanation of how the forces and moments behave at combinations of heave- and sway velocities.
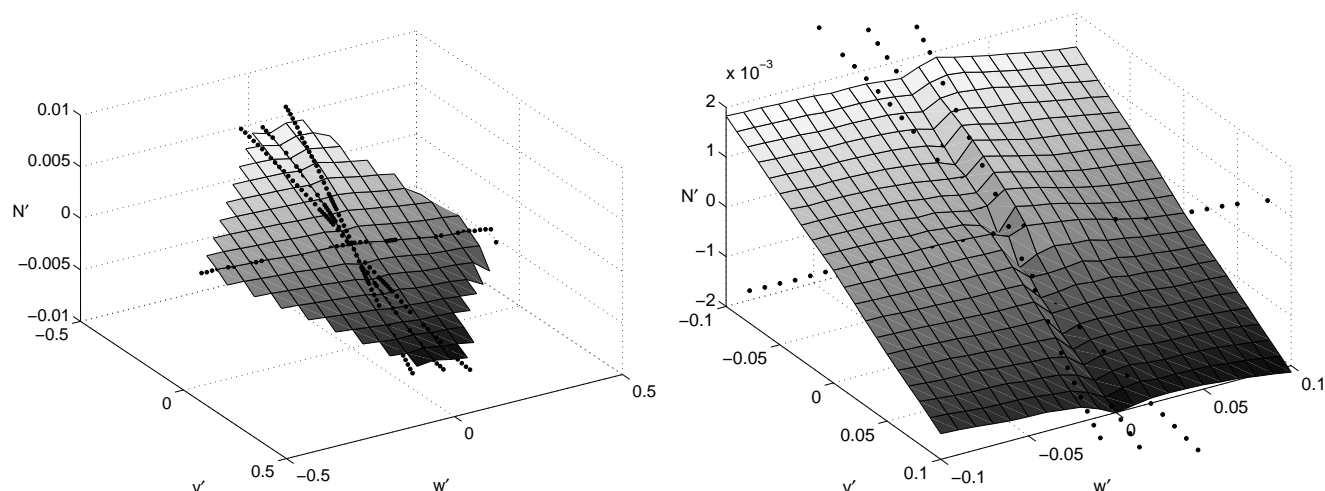
Figure 4.25: Yawing moment at combinations of normal and transversal velocities

4.2   Ellipsoid unsteady maneuvers

Three different pitch motions are used for unsteady tests as shown in Figure 4.26. The first one starts at a static angle of attack α, or sideslip β of $-15°$ and ends at $0°$ after $t' \approx 6$. The second motion starts with the same initial conditions as the first one, but continues with a rotation past $0°$ at $t' \approx 6$ to a static $+15°$ at $t' \approx 12$. The third motion starts at a static angle of $0°$ and ends at $15°$ after $t' \approx 6$. All unsteady motions are repeated twenty times to reduce ensemble uncertainties.
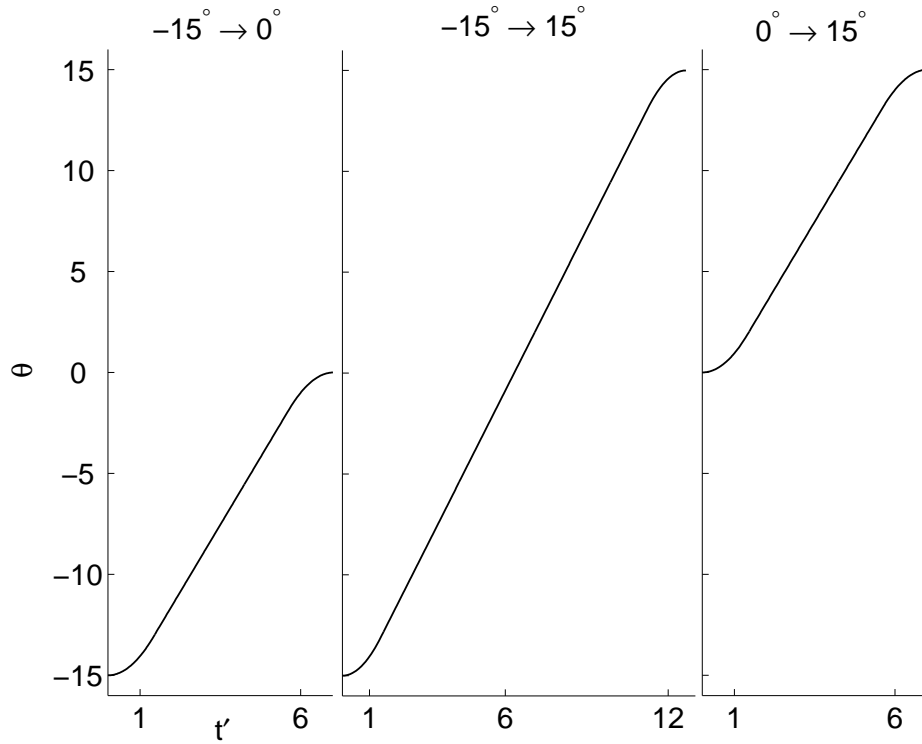
Figure 4.26: Three different pitch ramp unsteady motions

The idea is to perform unsteady motions of slender bodies similar in maneuvering envelope and time to submarines. The results from the unsteady motions will also be used to investigate the dependence on initial conditions as described in Chapter 1.

Figure 4.27 shows the change in states during the $-15°$ to $+15°$ motion. Both states are needed when conducting analytical force and moment predictions of the motions since the body is rotated at $\zeta = 0.25$. If the rotation had been at $\zeta = 0.5$ where the origin of the coordinate system is, then $q = \dot{\alpha}$.
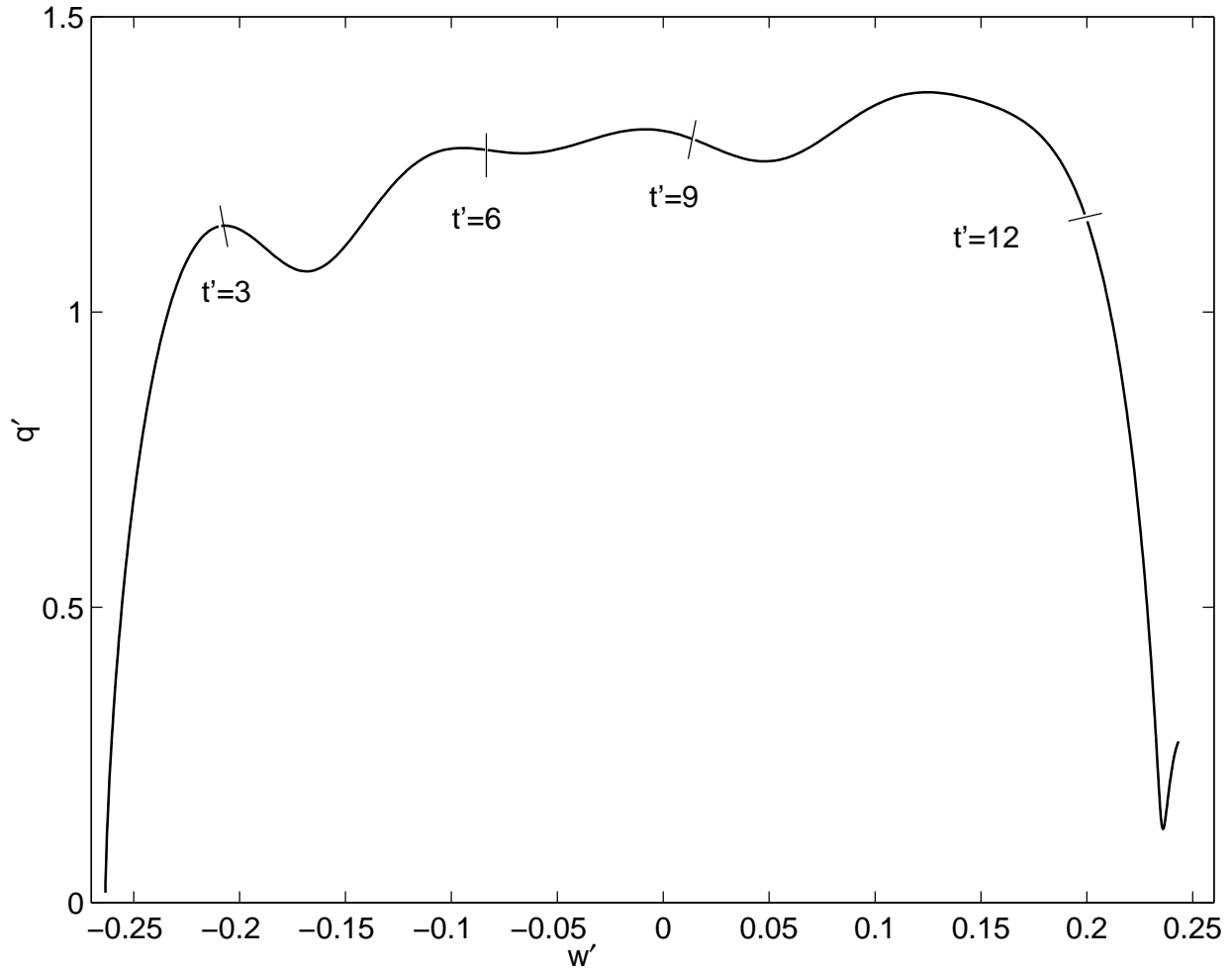

Figure 4.27: Change of states during an unsteady motion

4.2.1   Unsteady motion − $\alpha : -15° \to 15°$

When starting from a steady state with angle of attack $\alpha = -15°$ and rapidly increasing the angle of attack by rotating around $\zeta = 0.25$, the normal force in Figure 4.28 decreases slower than what the quasi-steady approximation predicts. This continues as long as the pitch angular velocity is increasing or is constant. At $t' \approx 7$ the model is aligned with the freestream but with a pitch angular velocity. Continuing until $t' \approx 13$, the normal force increases in magnitude faster than the quasi-steady prediction where the motion is slowed down towards a steady angle of attack of $\alpha = 15°$
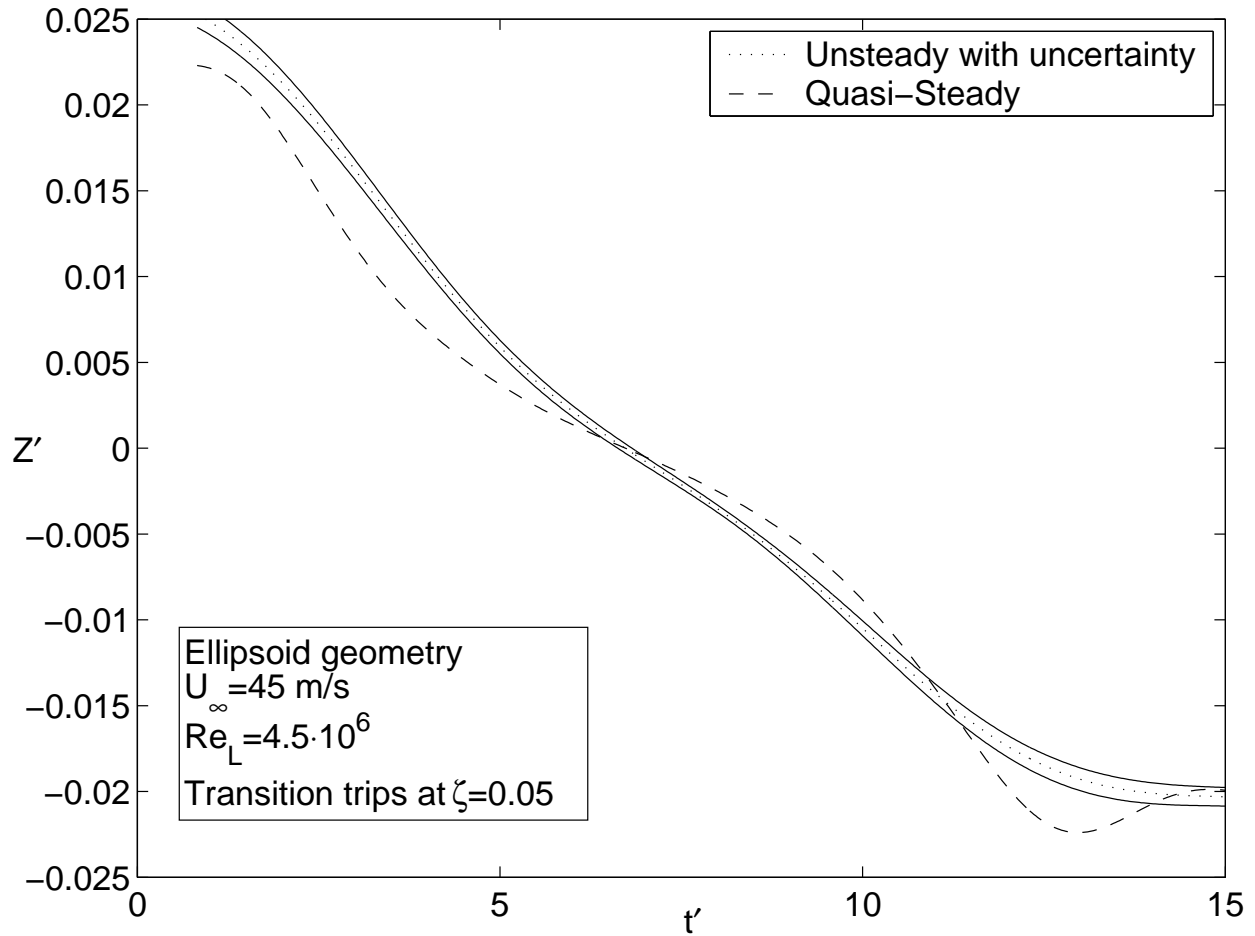
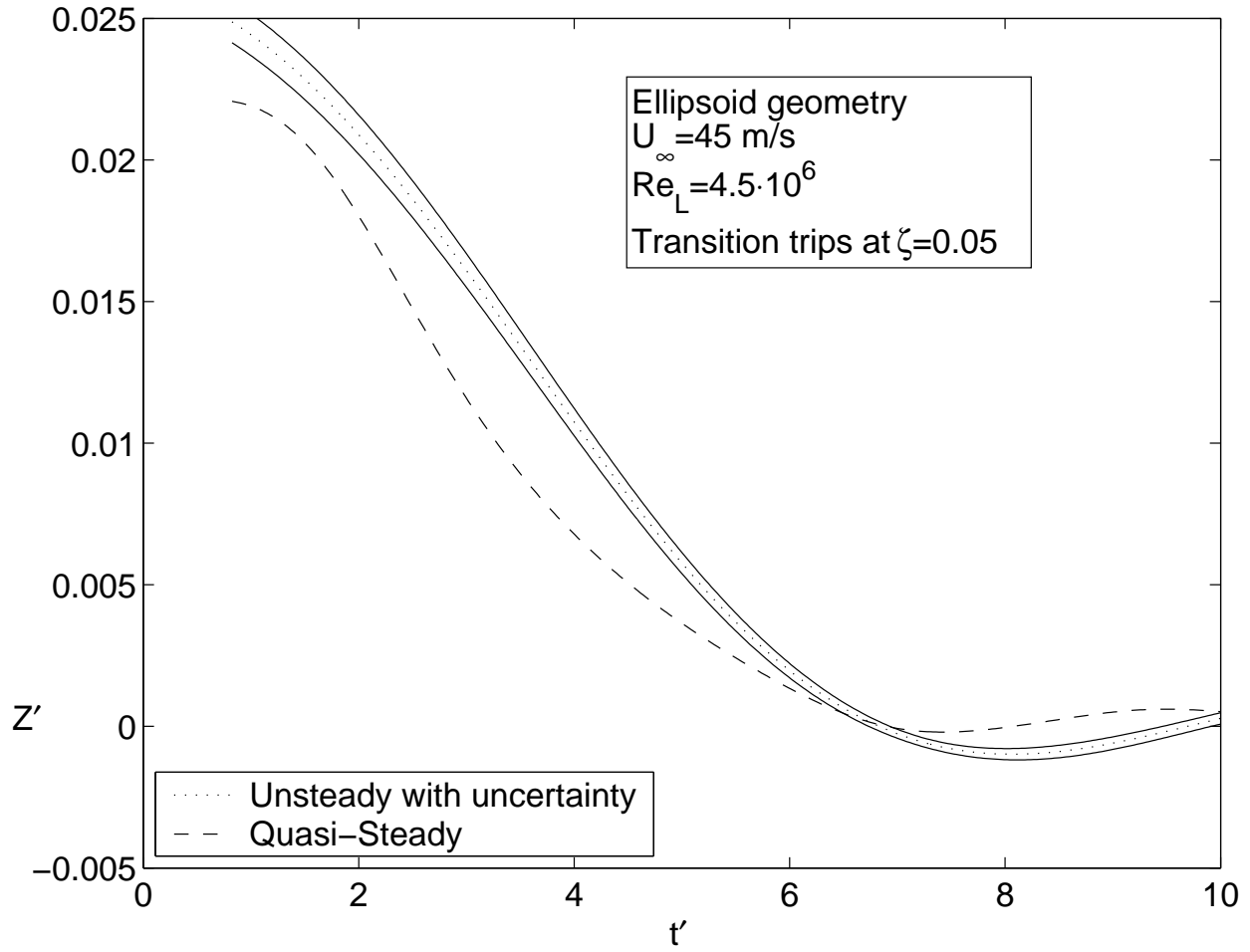Figure 4.28: Normal force $\alpha : -15° \to 15°$

The pitch moment in Figure 4.29 recorded during the unsteady motion is continuously lower than the quasi-steady prediction.
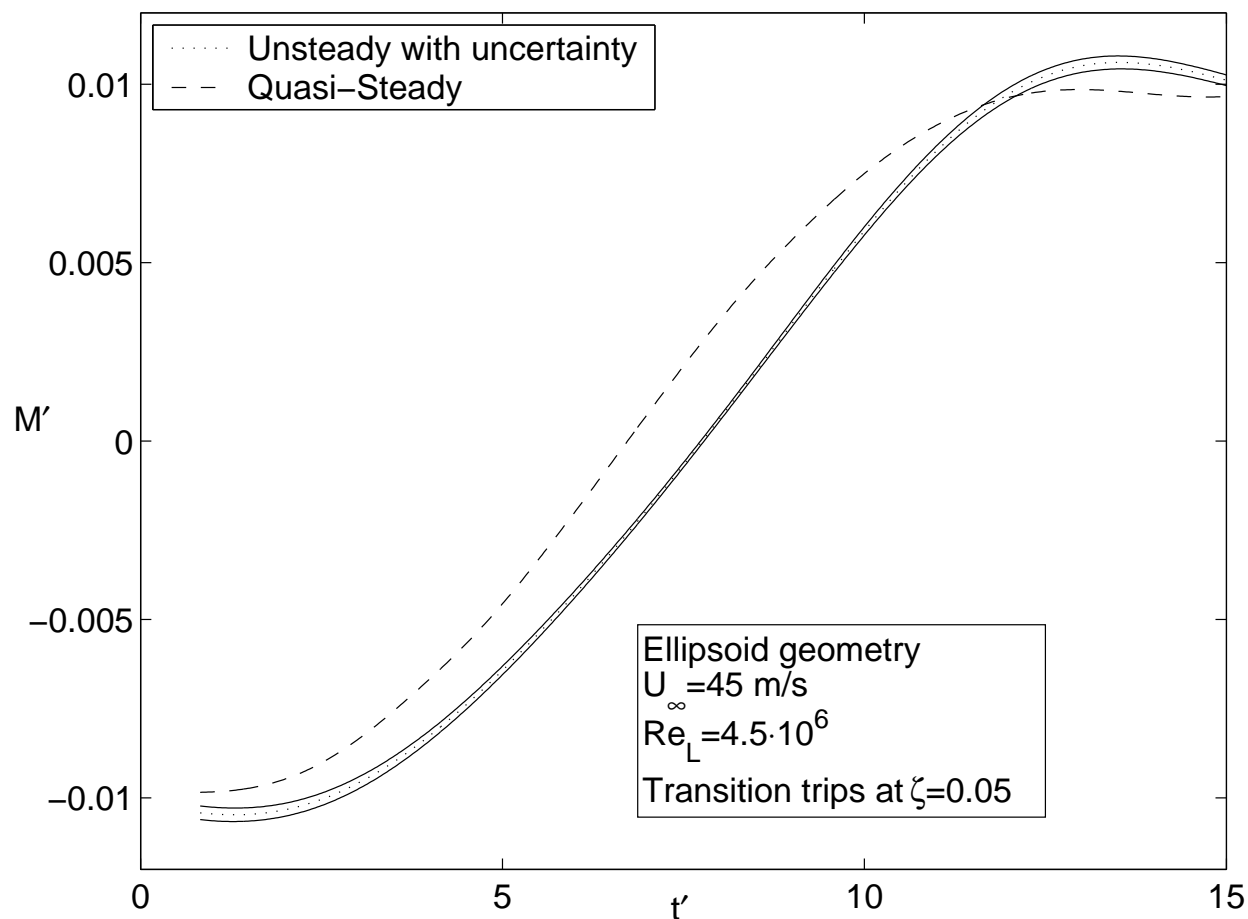
Figure 4.29: Pitch moment $\alpha : -15° \rightarrow 15°$

Due to difficulties in the filtering process described in Chapter 3, the initial conditions are not correct. The middle part of the motion is however correct in both phase and amplitude.

4.2.2   Unsteady motion − $\alpha : -15° \rightarrow 0°$

When starting from a steady state with angle of attack $\alpha = -15°$ and rapidly increasing the angle of attack by rotating around $\zeta = 0.25$, the normal force in Figure 4.30 decreases slower than what the quasi steady approximation predicts. This continues as long as the pitch angular velocity is increasing or is constant. At $t' \approx 7$ the motion is slowed down towards a steady angle of attack of $\alpha = 0°$ and the normal force approaches the quasi-steady value.

Figure 4.30: Normal force $\alpha : -15° \rightarrow 0°$

The pitch moment in Figure 4.31 recorded during the unsteady motion is continuously lower than the quasi-steady prediction until the motion is slowed down. Overall, the same behavior is seen as for the first part of the $\alpha : -15° \rightarrow 15°$ motion.
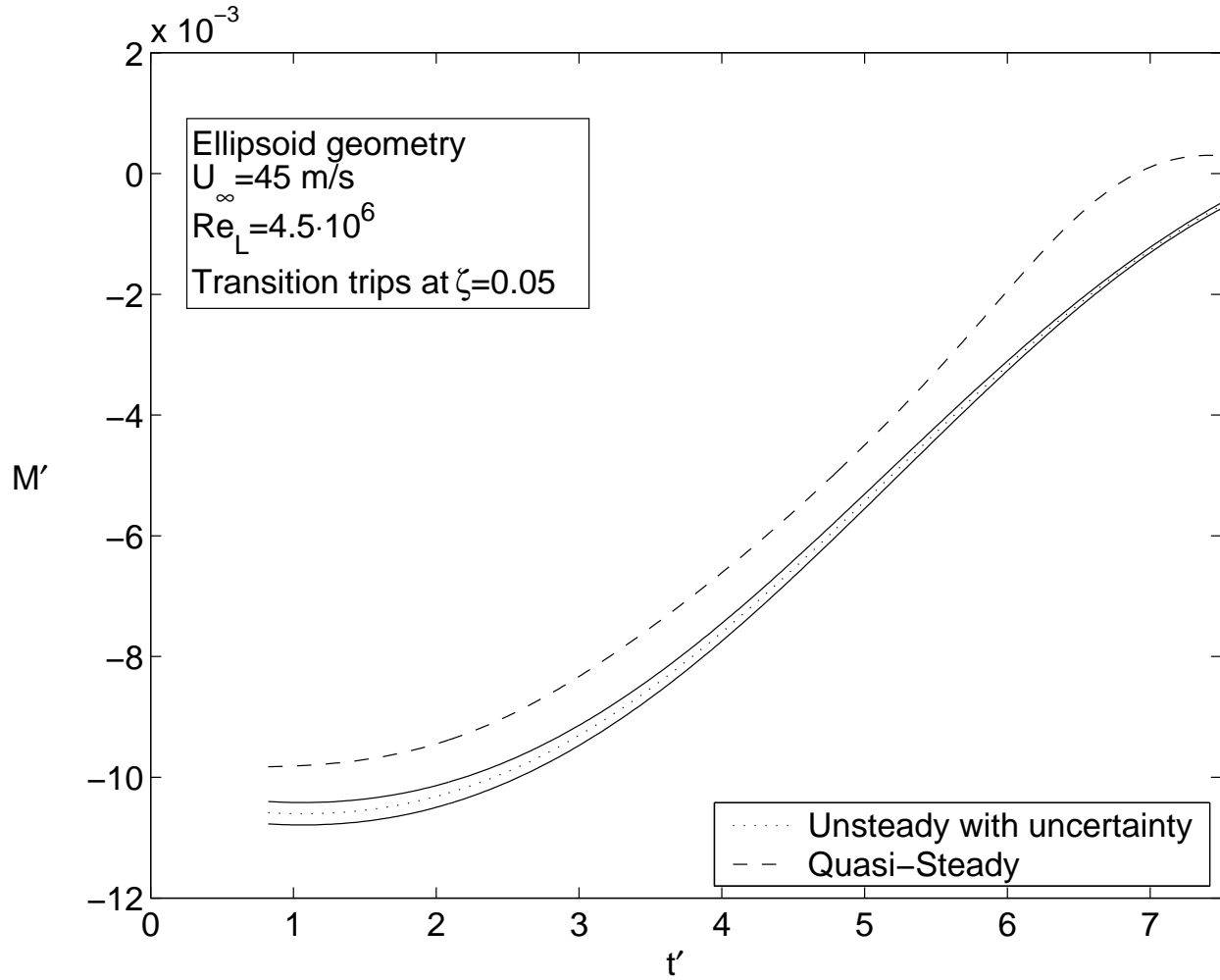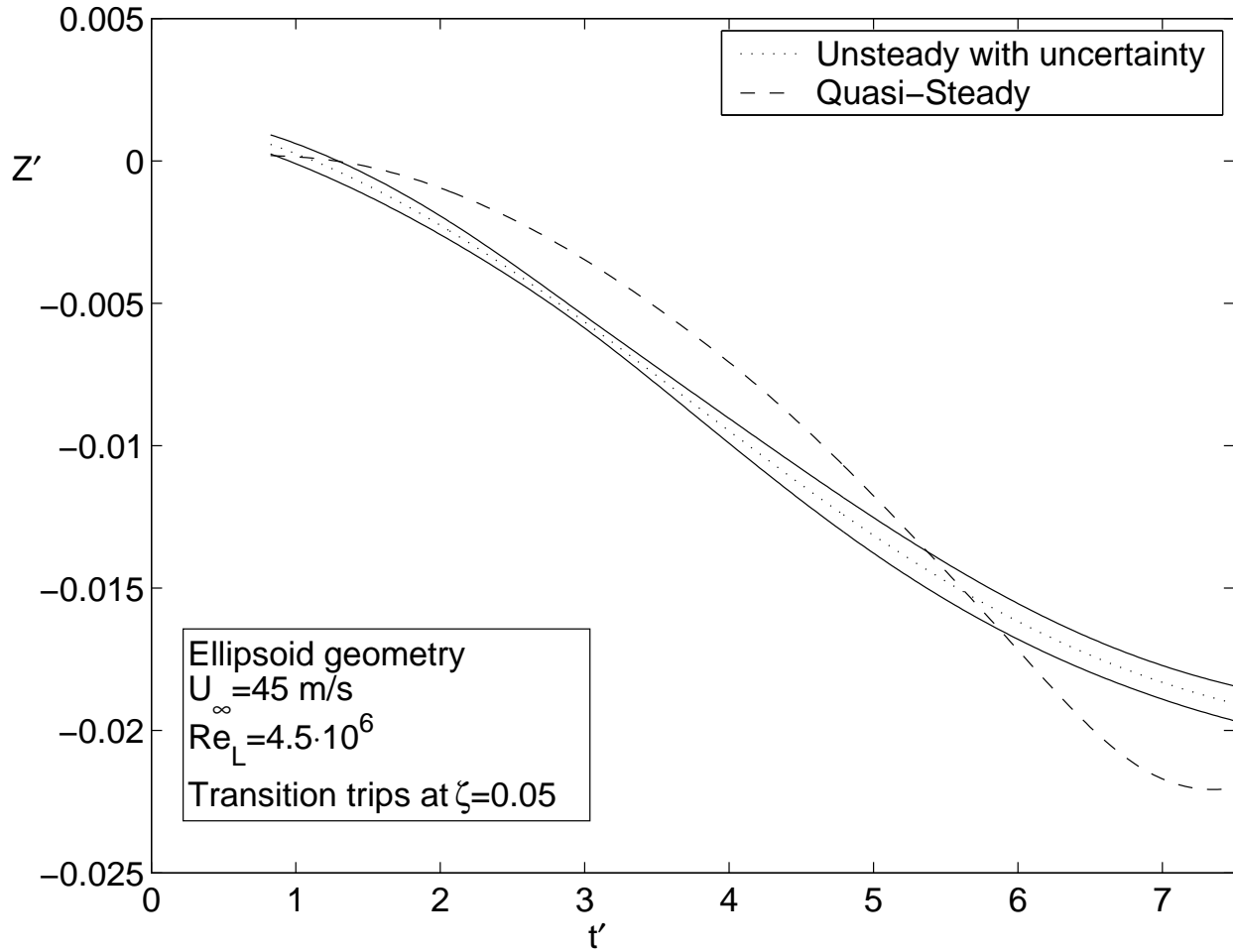

Figure 4.31: Pitch moment $\alpha : -15° \rightarrow 0°$

4.2.3   Unsteady motion − $\alpha : 0° \rightarrow 15°$

Starting from a steady state with angle of attack $\alpha = 0°$ and rapidly increasing the angle of attack by rotating around $\zeta = 0.25$, the normal force in Figure 4.32 increases faster than what the quasi-steady approximation predicts. This continues as long as the pitch angular velocity is increasing or is constant. At $t' \approx 7$ the motion is slowed down towards a steady angle of attack of $\alpha = 0°$ and the normal force approaches the quasi-steady value.

Figure 4.32: Normal force $\alpha : 0° \rightarrow 15°$

The pitch moment in Figure 4.33 recorded during the unsteady motion is continuously lower than the quasi-steady prediction until the motion is slowed down. Overall, the same behavior is seen as for the $\alpha : -15° \rightarrow 15°$ motion.
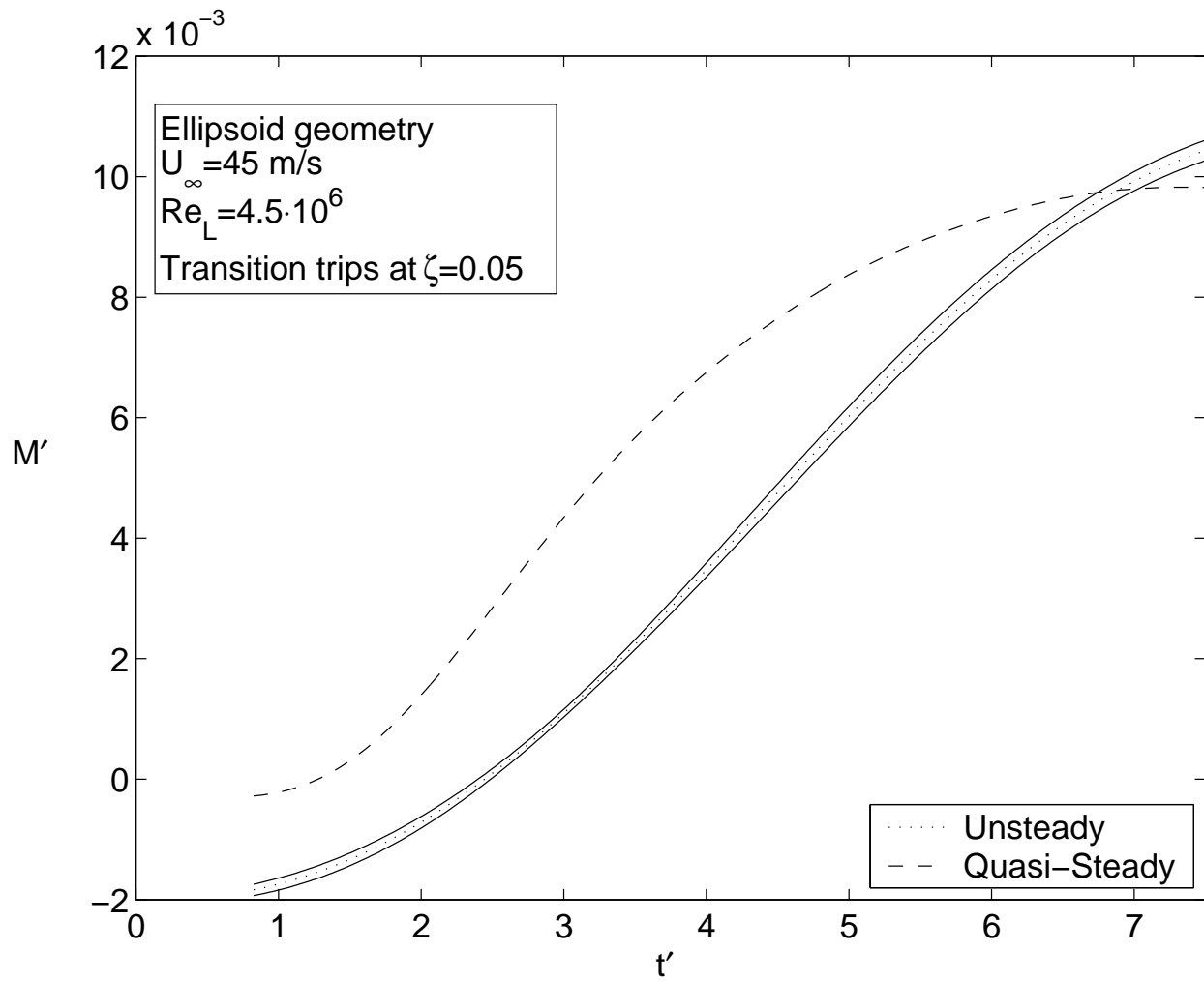

Figure 4.33: Pitch moment $\alpha : 0° \rightarrow 15°$

4.3 Unsteady maneuver video analysis

Still frames have been extracted from a recorded videoclip of the unsteady maneuvers. Because the video was recorded and later saved in Windows Media Video 9 [60] format, it is slightly difficult to tell exactly what rate of still frames the video has, and if that framerate is even consistent since WMV9 has adaptive compression. Video still frames are also not synchronized with the model motion, so it is difficult to set an accurate timestamp to every frame. The figures 4.34 to 4.39 seem to complete the motion within the 0.5s in Figure 4.42 and 4.43 such that there is a nominal 100ms between the frames. Figures 4.42 and 4.43 depict the stopping oscillation of the model.

The model is rotated about $\zeta = 0.25$; this point has been marked with a red dot in every frame. Alignment lines with 75mm spacing have been drawn from the slotted walls in every frame.

4.3.1 Unsteady motion $- \alpha : -15° \rightarrow 15°$

Figure 4.34 is before the motion has started. In the second figure 4.35 one can observe that the red dot has moved vertically approximately 8cm from the original location in Figure 4.34. The model is pitched up more rapidly than the correct motion.
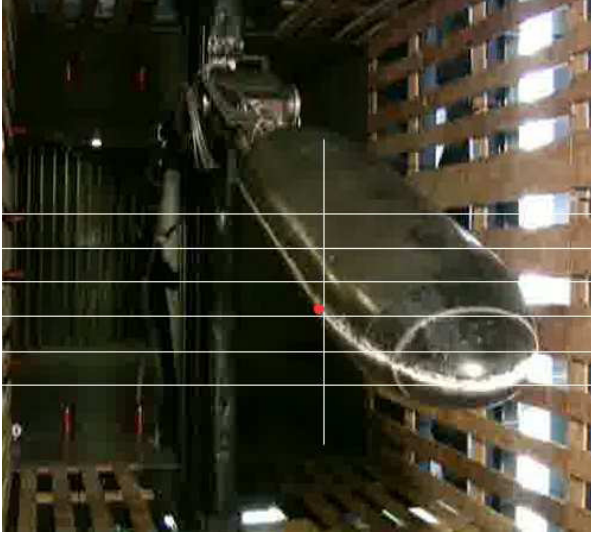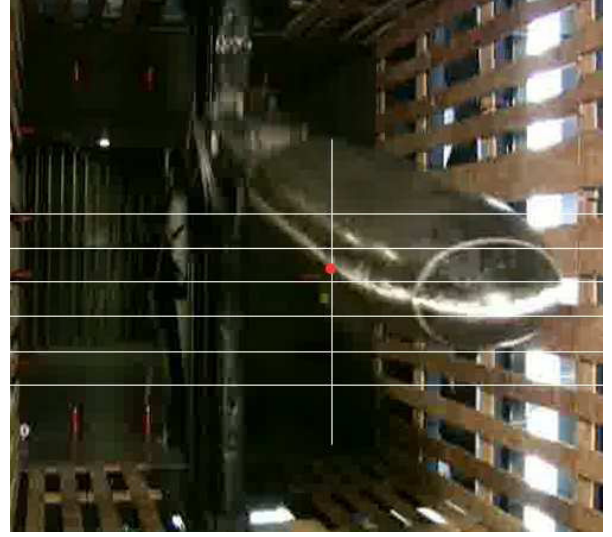
Figure 4.34: $\alpha : -15° \to 15°$ t_0

Figure 4.35: $\alpha : -15° \to 15°$ $t_0 + 100ms$

In Figure 4.36 and Figure 4.37 the $\zeta = 0.25$ location is nearly constant, but still incorrect location compared to the initial location.
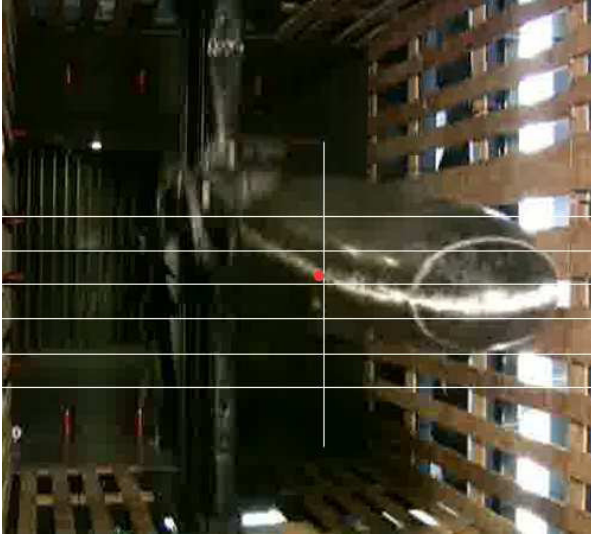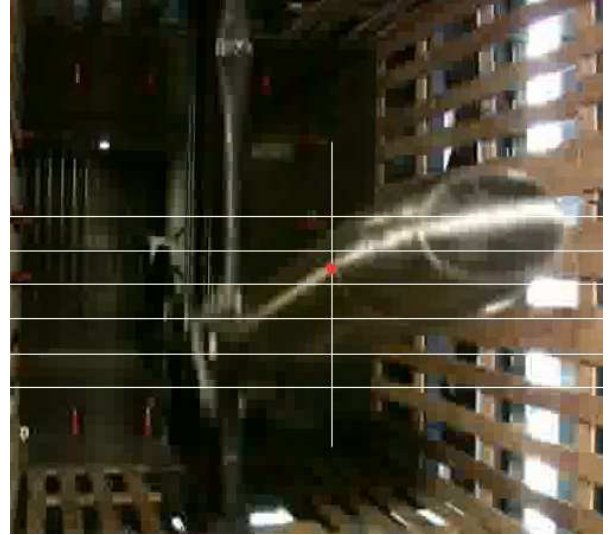

Figure 4.36: $\alpha : -15° \to 15°$ $t_0 + 200ms$

Figure 4.37: $\alpha : -15° \to 15°$ $t_0 + 300ms$

In Figure 4.38 and Figure 4.39 the model $\zeta = 0.25$ position starts to drop down to the correct location, and in Figure 4.41 the model $\zeta = 0.25$ location is back at the correct location.
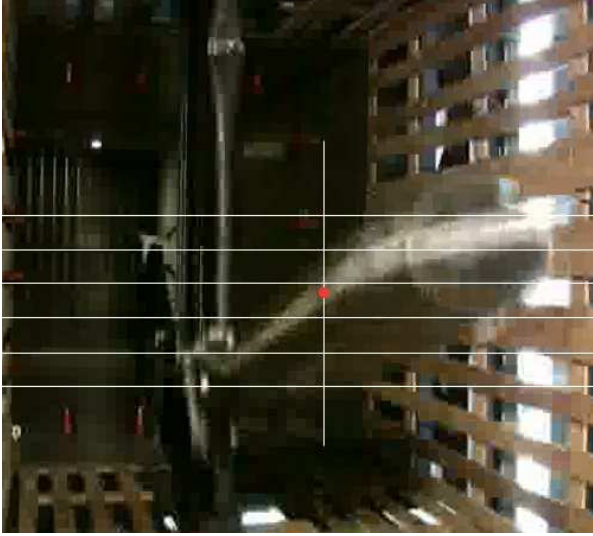

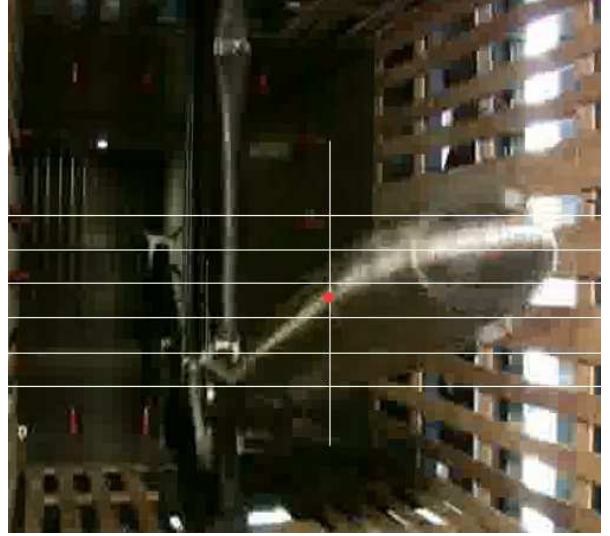Figure 4.38: $\alpha : -15° \rightarrow 15°$ $t_0 + 400ms$

Figure 4.39: $\alpha : -15° \rightarrow 15°$ $t_0 + 500ms$

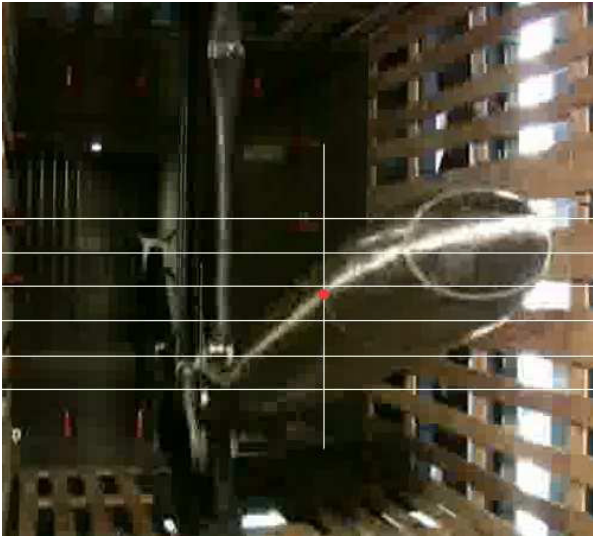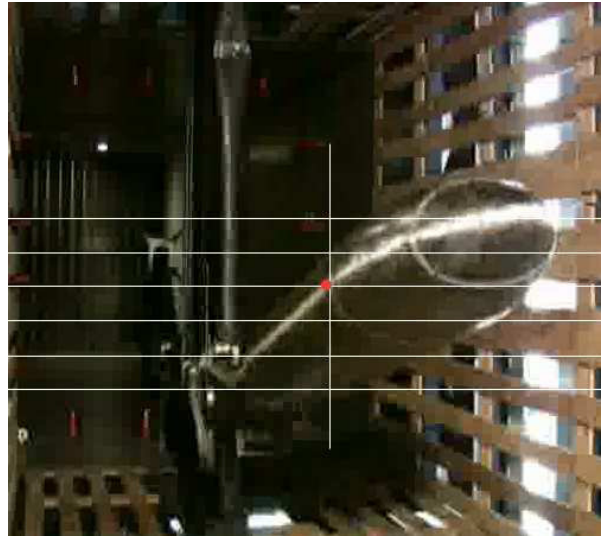

Figure 4.40: $\alpha : -15° \rightarrow 15°$ $t_0 + 600ms$
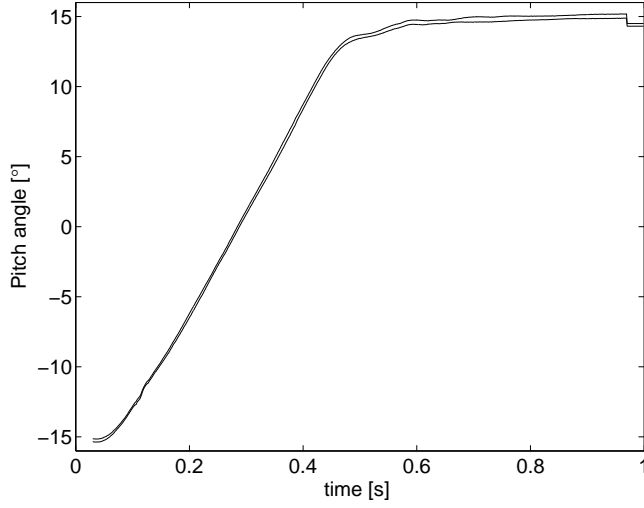

Figure 4.41: $\alpha : -15° \rightarrow 15°$ $t_0 + 700ms$

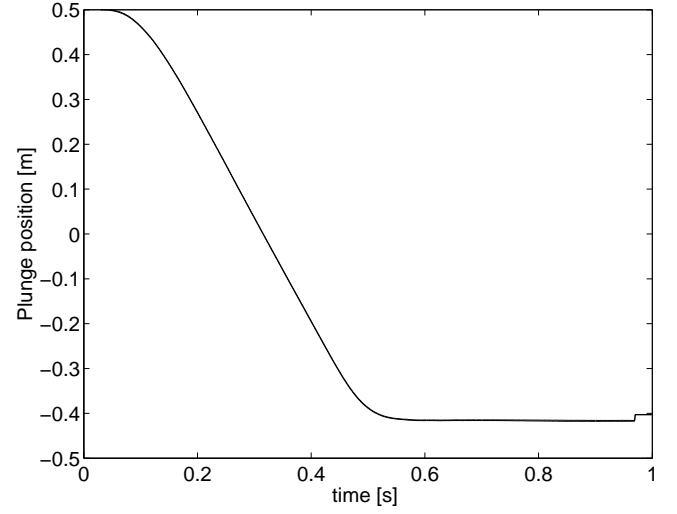Figure 4.42: $\alpha : -15° \rightarrow 15°$ pitch angle position

Figure 4.43: $\alpha : -15° \rightarrow 15°$ plunge vertical position

Figure 4.42 and 4.43 show the position uncertainty bounds over twenty repetitions of the vertical- and pitch actuators respectively. Repeatability uncertainties during motions are $0.5mm$ in plunge and $0.1°$ in pitch. One can observe that the motions are very repeatable and no large oscillations in actuator position occur. At close inspection the pitch actuator position has a minor oscillation at $t \approx 0.1s$. The inaccurate pitch position and relatively large uncertainty for $t > 0.45s$ is after the motion has ended and when the model is abrubtly slowed down.

4.3.2 Unsteady motion − $\alpha : -15° \rightarrow 0°$
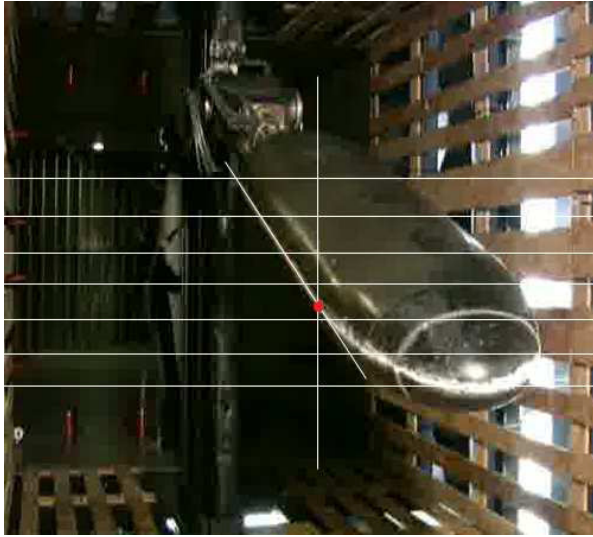
Figure 4.44: $\alpha : -15° \rightarrow 0°$ t_0
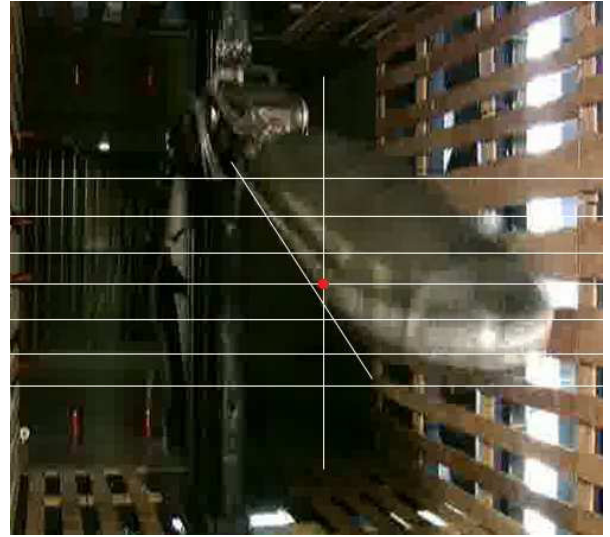
Figure 4.45: $\alpha : -15° \rightarrow 0°$ $t_0 + 100ms$

In Figure 4.45 one can observe that the center of rotation location $\zeta = 0.25$ has moved up aproximately 5cm from the initial location in Figure 4.44. In Figure 4.46 the $\zeta = 0.25$ location has moved up another 2.5cm from the location in Figure 4.46 only to move down to the correct position in Figure 4.47.
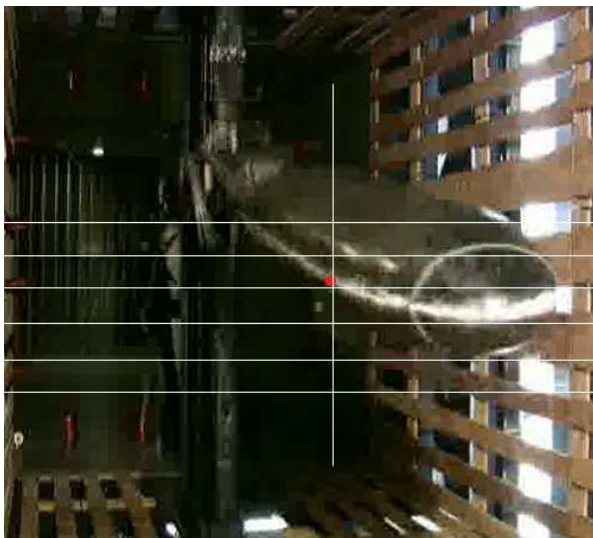
Figure 4.46: $\alpha : -15° \rightarrow 0°$ $t_0 + 200ms$
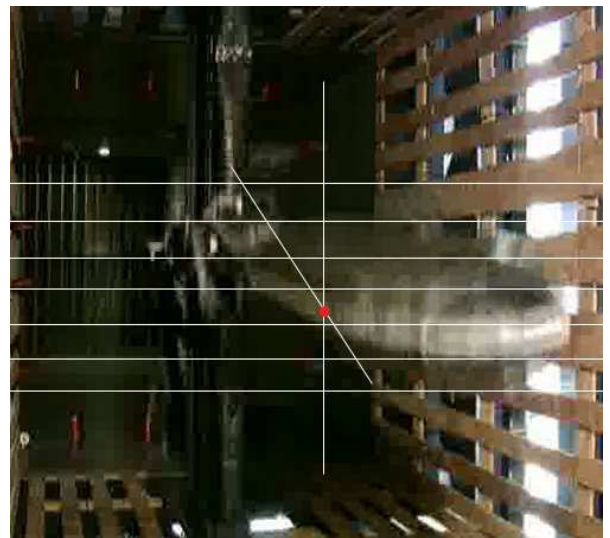
Figure 4.47: $\alpha : -15° \rightarrow 0°$ $t_0 + 300ms$
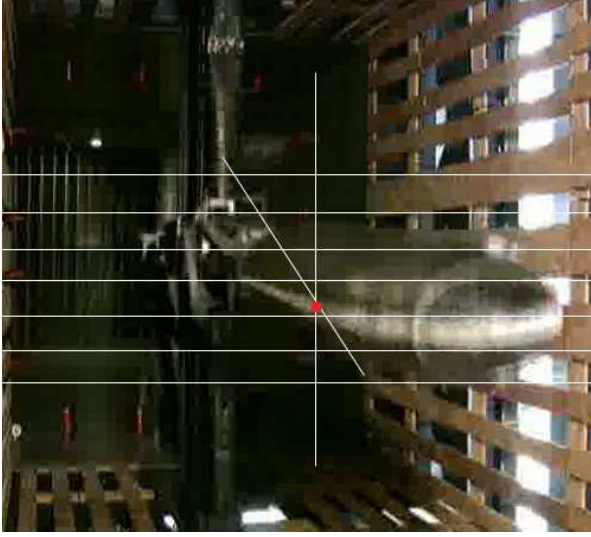
Figure 4.48: $\alpha : -15° \to 0°$ $t_0 + 400ms$
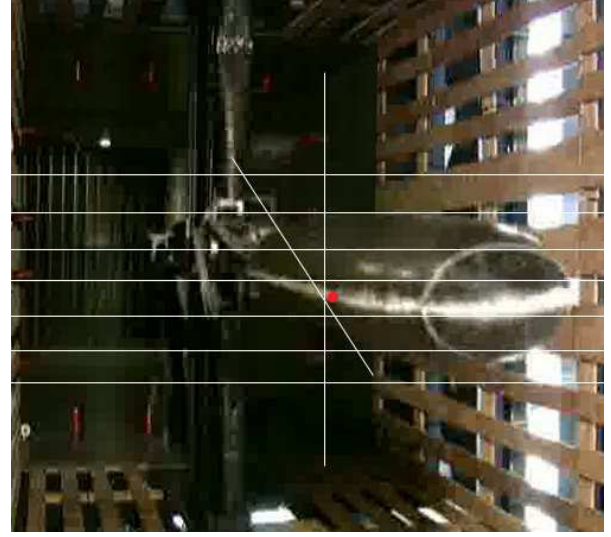
Figure 4.49: $\alpha : -15° \to 0°$ $t_0 + 500ms$

The center of rotation location $\zeta = 0.25$ stays constant in the correct location throughout the remainder of the motion as evident in Figure 4.48 and 4.49. Figure 4.50 and 4.51 shows the position uncertainties over twenty repetitions of the vertical- and pitch actuators respectively. One can observe that the motions are very repeatable and no large oscillations in actuator position occur except a minor oscillation at $t \approx 0.1s$.
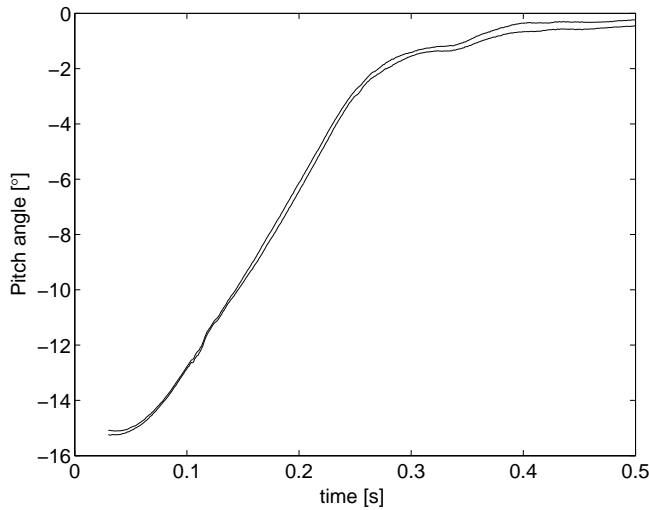
Figure 4.50: $\alpha : -15° \to 0°$ pitch angle position
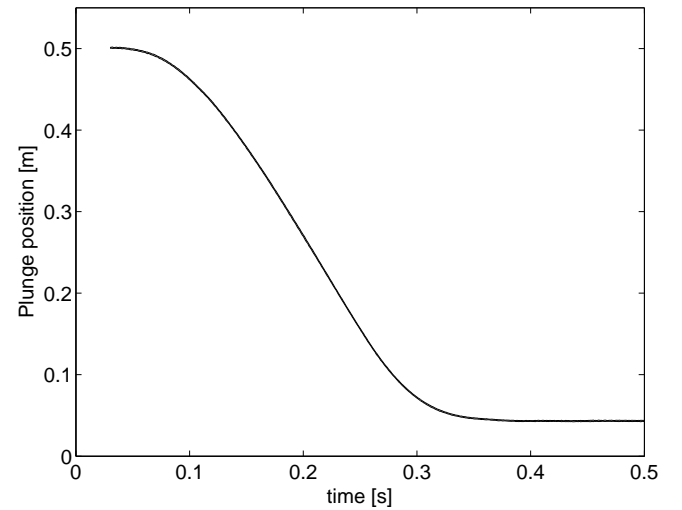
Figure 4.51: $\alpha : -15° \to 0°$ plunge vertical position

4.3.3   Unsteady motion − $\alpha : 0° \to 15°$

Figure 4.52: $\alpha : 0° \to 15°$ t_0

Figure 4.53: $\alpha : 0° \to 15°$ $t_0 + 100ms$

The model is initially pitched rapidly from Figure 4.52 (causing a blurry picture) in Figure 4.53. In Figure 4.54 the model has pitched up too quickly so that the $\zeta = 0.25$ location is approximately 75mm higher up than what it is supposed to be.
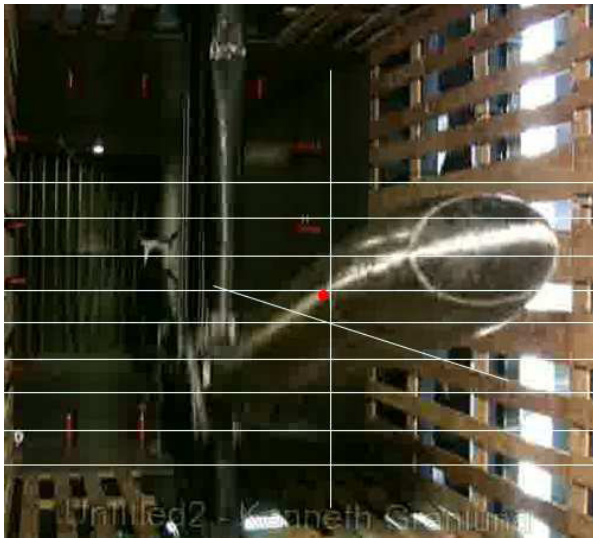
Figure 4.54: $\alpha : 0° \to 15°$ $t_0 + 200ms$
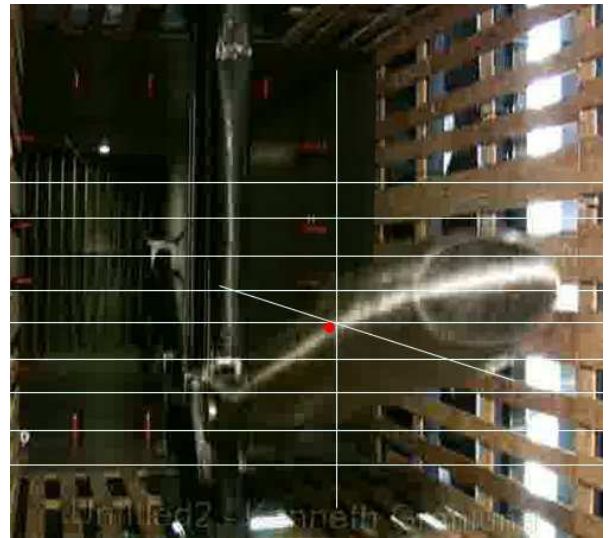
Figure 4.55: $\alpha : 0° \to 15°$ $t_0 + 300ms$

During the remainder of the motion going from Figure 4.55 to 4.57 the model is rotated around the correct position. In Figure 4.58 one can observe significantly larger pitch position uncertainties than in Figure 4.59 for plunge. What is more alarming is the quite significant oscillation in pitch at $t \approx 0.1s$. This is a much larger oscillation than what is evident in the two other motions.
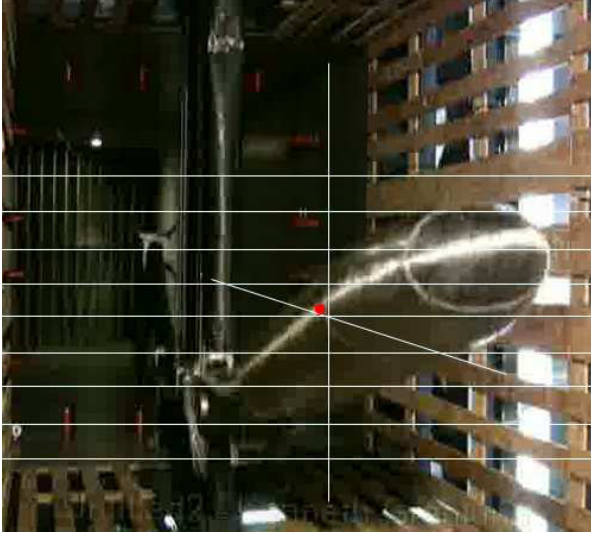
Figure 4.56: $\alpha : 0° \rightarrow 15°$ $t_0 + 400ms$
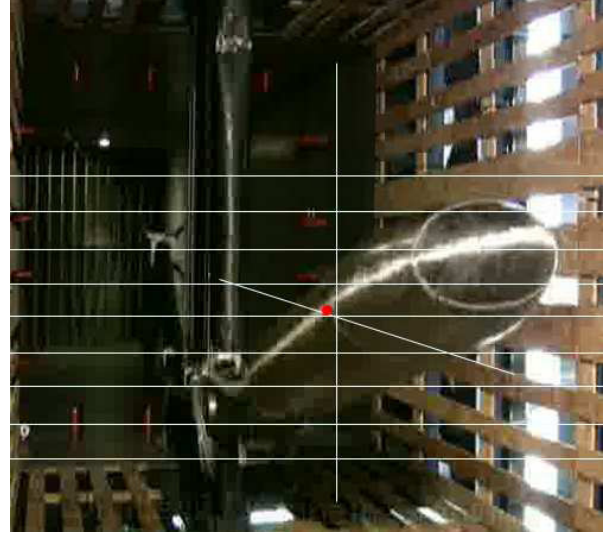
Figure 4.57: $\alpha : 0° \rightarrow 15°$ $t_0 + 500ms$
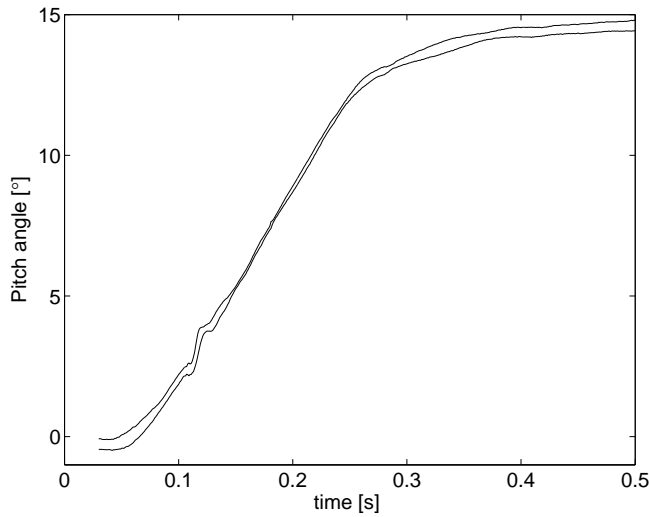
Figure 4.58: $\alpha : 0° \rightarrow 15°$ pitch angle position
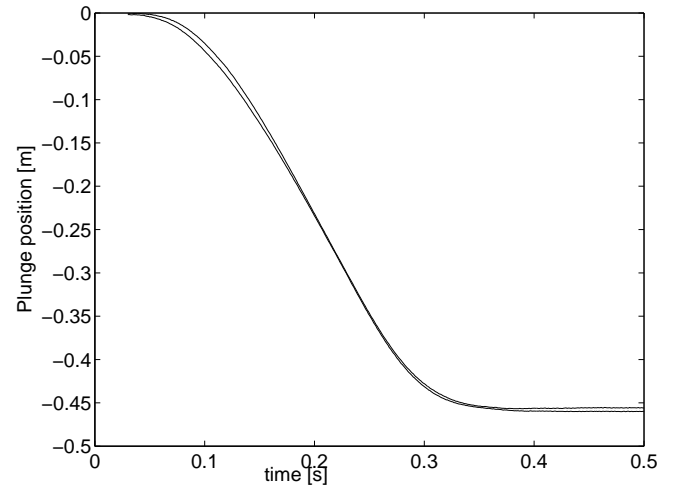
Figure 4.59: $\alpha : 0° \rightarrow 15°$ plunge vertical position

Is is evident in all three motions that there is a pitch impulse right after starting the motion that is believed to be the cause of the model pitching up too quickly and not hold the $\zeta = 0.25$ center of rotation in a fixed location. It is definitely a source of the inertial loads on the model that makes is more difficult to extract the aerodynamic contribution. Since the image frames have significant time separation, it is also difficult to judge the magnitude of the incorrect motion of the model and effect it has on the forces and moments during the entire motion, even when the model is following the correct motion in the middle and latter stages of the motion.

Since the imperfection of the motion is very repeatable, it has to originate from the hydraulic control system in the pitch circuit of the DyPPiR. The history of repairs of the DyPPiR in Appendix C go into depth why the electrohydraulic feedback control of the pitch circuit is too sensitive and has difficulties controlling the position.

4.4 Barebody Suboff steady data

4.4.1 Normal force

From Figure 4.60 one can observe a linear region for small translation velocities (or angles of attack) for $|\alpha| < 5°$ or $|w'| < 0.07$ in Equation 4.22.
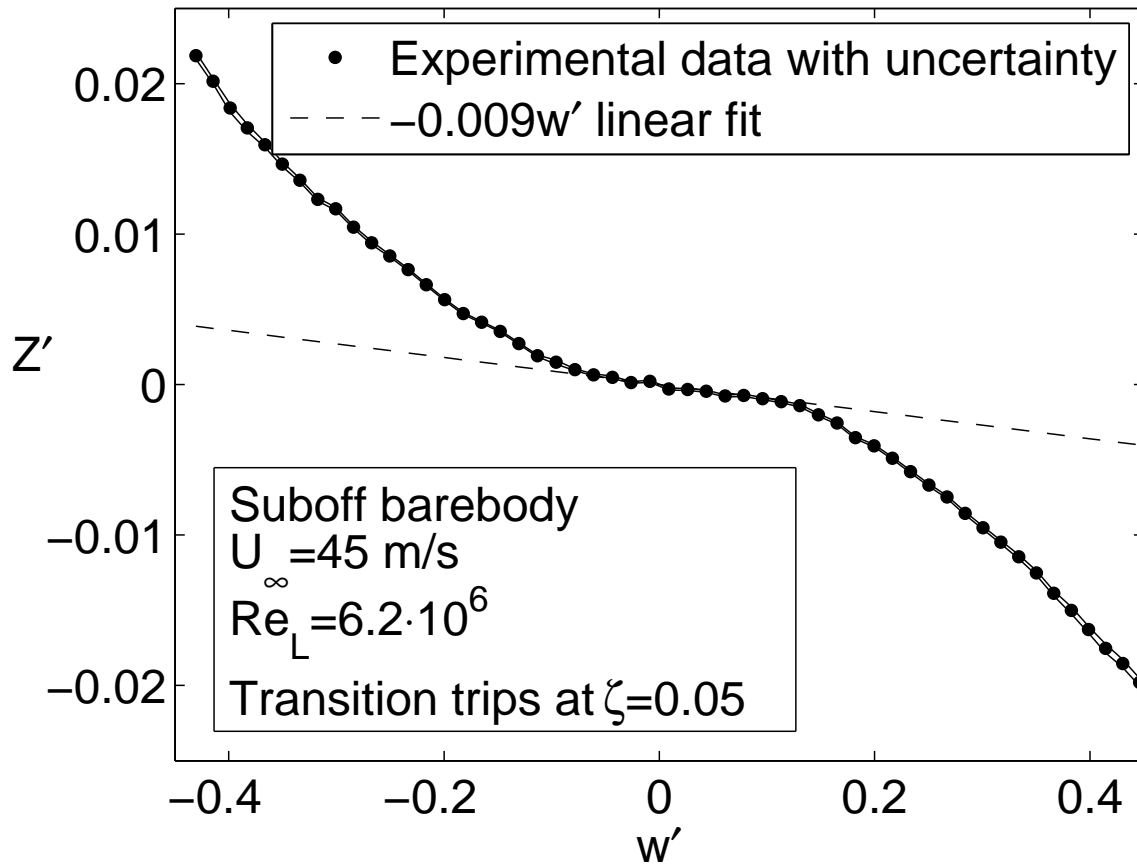
Figure 4.60: Steady normal force as function of translation velocity

$$Z'_{att} = -0.009w' \tag{4.22}$$

The cross-flow separation second order lift component shown in Figure 4.61 and Equation 4.23 for $|w'| > 0.07$ is
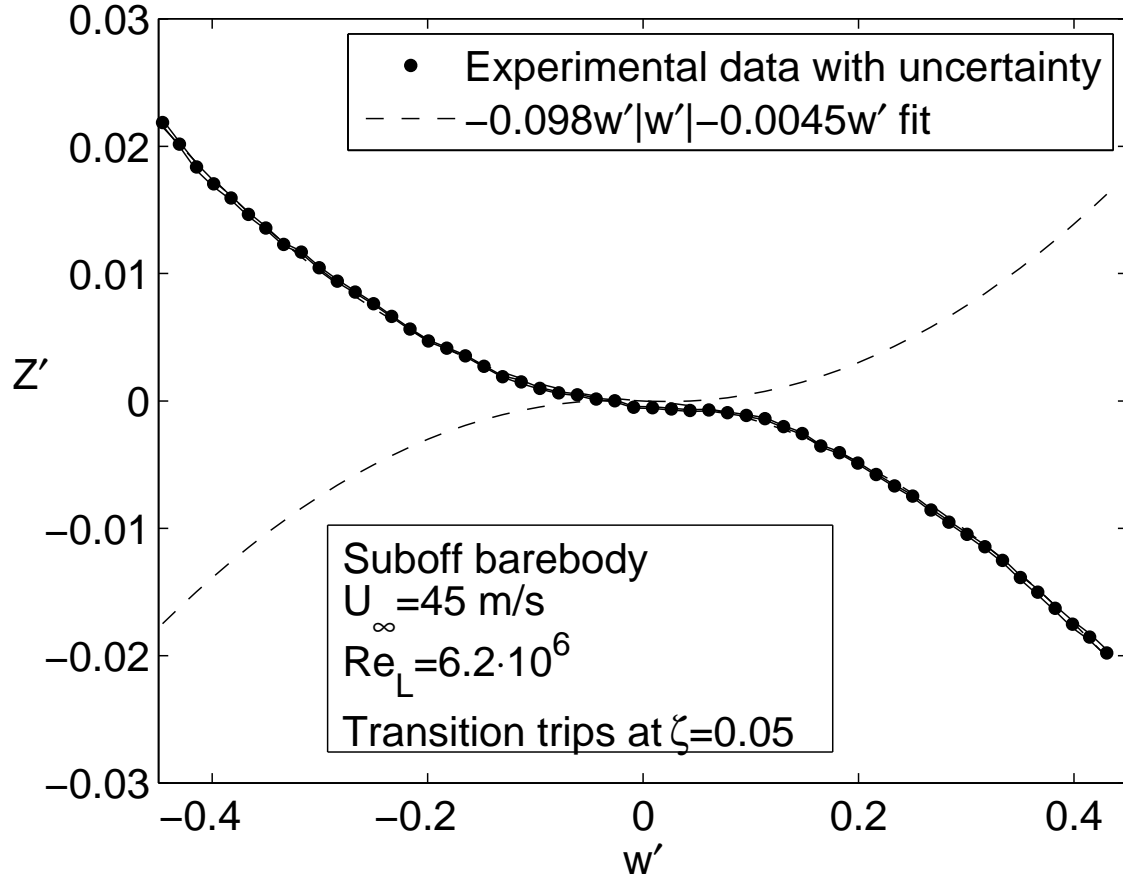
Figure 4.61: Quadratic fit to normal force

$$Z'_{vor} = -0.098w'|w'| + 0.0045w' \qquad (4.23)$$

The functional form of the normal force in Equation 4.24 fits within the uncertainty bounds of the experimental data in Figure 4.62.
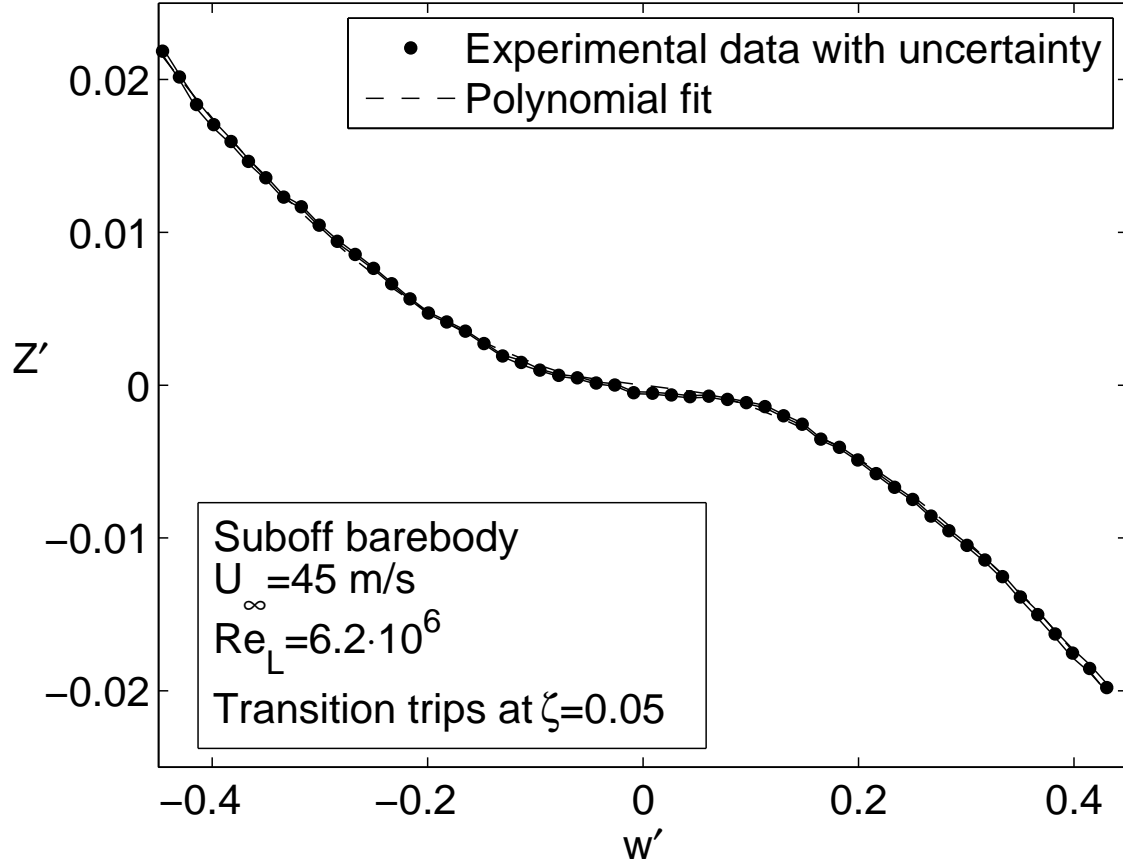
Figure 4.62: Polynomial fit to normal force

$$Z'_{vor} = -0.009w' + \frac{1}{1 + exp(-k|w'| - 0.07)}(-0.098w'|w'| + 0.045w') \qquad (4.24)$$

4.4.2 Pitch moment

From Figure 4.63 one can observe a linear region for small translation velocities (or angles of attack) for $|\alpha| < 5°$ or $|w'| < 0.07$ in Equation 4.25.
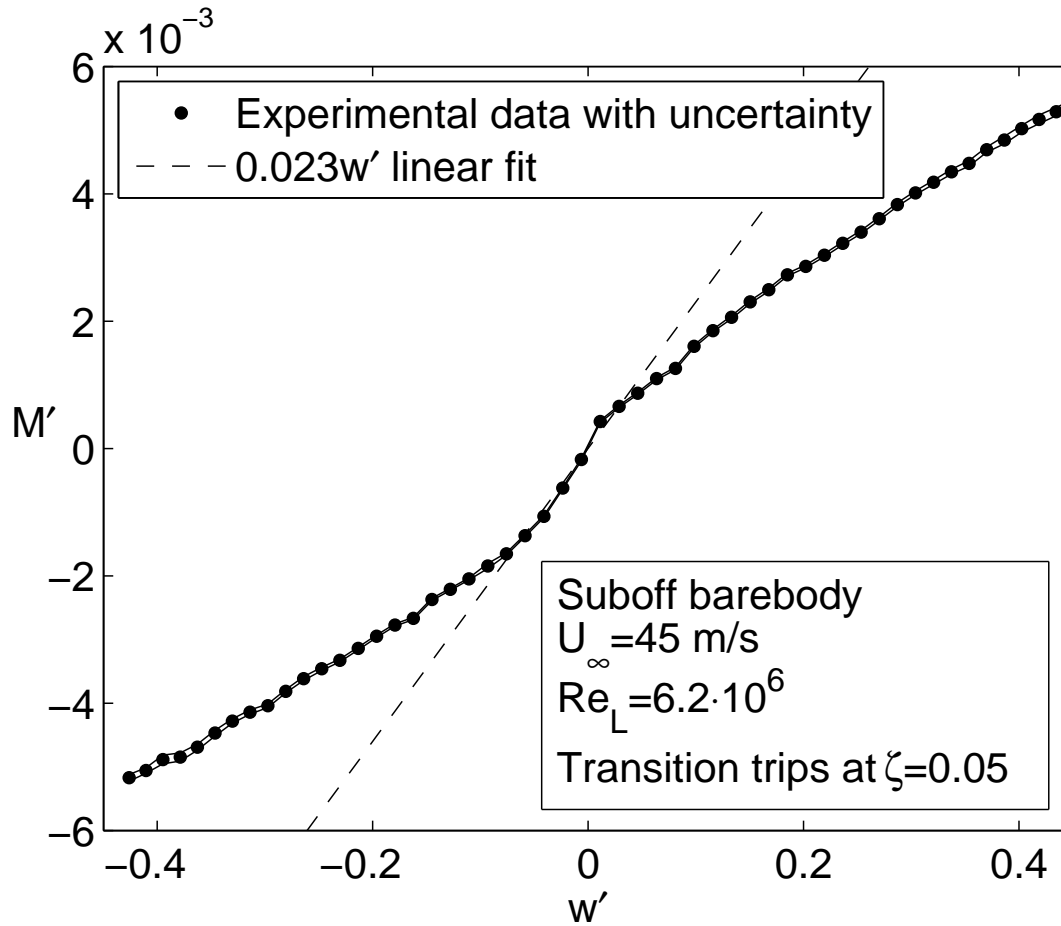
Figure 4.63: Linear fit to pitch moment as function of translation velocity

$$M' = 0.023w' \tag{4.25}$$

If we use the same form of equation to predict the pitch moment as for the ellipsoid body, one can observe that there is no constant center of pressure for the vortical contribution that will make Equation 4.26 fit the experimental data in Figure 4.64.
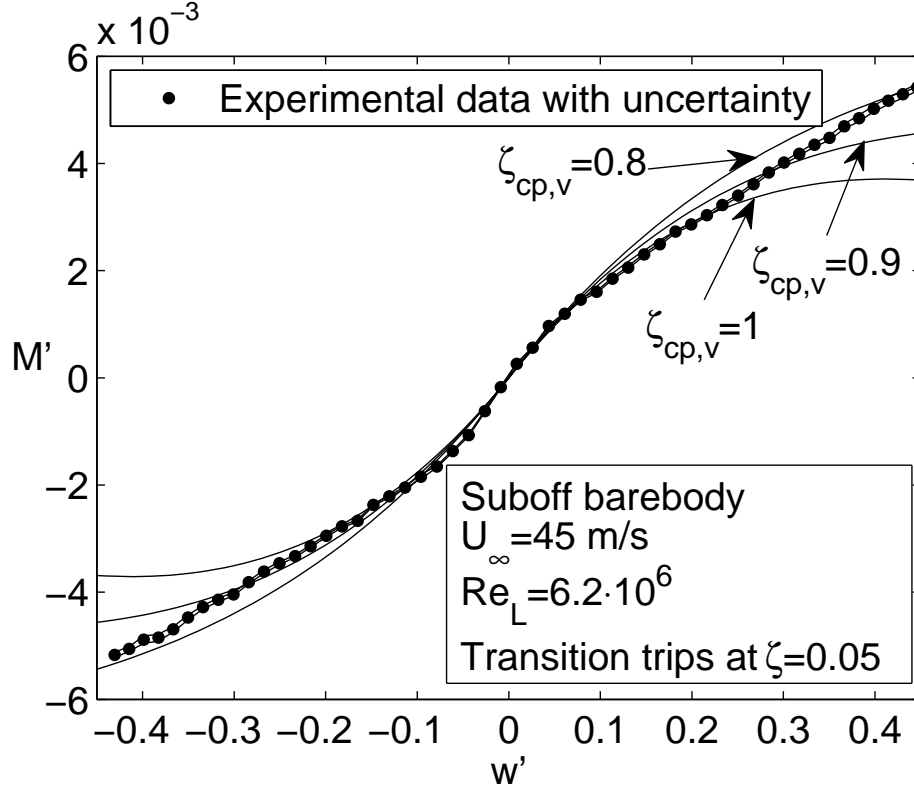
Figure 4.64: Polynomial fit to pitching moment

$$M' = 0.023w' + \frac{(\zeta_{cp,v} - \zeta_M)Z'_{vor}}{1 + exp(-k|w'| - 0.07)} \qquad (4.26)$$

For small angles slightly larger than $w' = 0.07$, a $\zeta_{cp,v} \approx 1$ will fit the data. For larger angles, a center of pressure location of the vortical contribution $\zeta_{cp,v}$ more upstream on the body makes the analytical prediction fit the data. This is supported by the results by Hosder and Simpson [49]. This behavior is unlike the ellipsoid, where the center of pressure for the cross-flow separation contribution is a fixed location. An effect of this is that the longitudinal instability of the Suboff is reduced less than for the ellipsoid.

118

4.5 Suboff with sail steady data

4.5.1 Normal force

For the Suboff geometry with a sail, one can observe that the presence of a sail modifies the coefficients from those for the barebody Suboff. The normal force slope $Z'_{w,att}$ in Figure 4.65 is less steep than for the barebody in Figure 4.60.
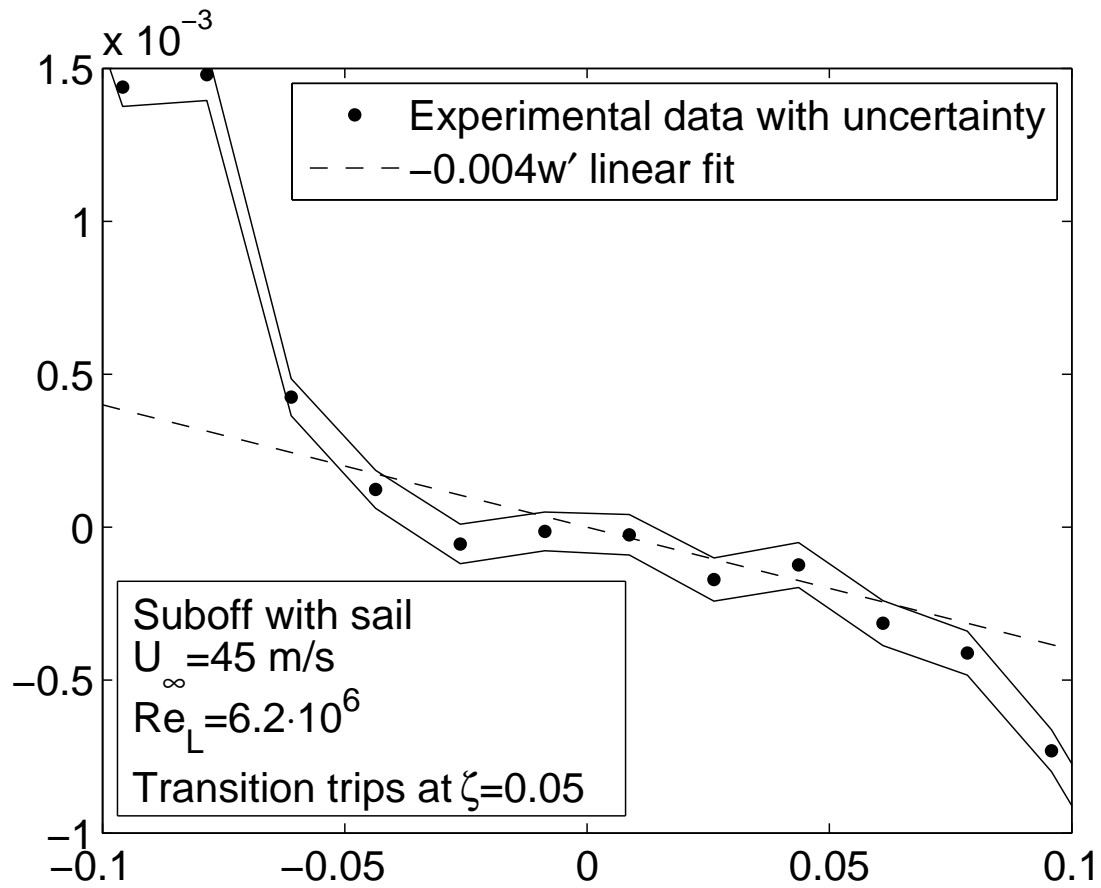
Figure 4.65: Linear fit to normal force

The crossflow contribution component Z'_{vor} is different depending on whether the angle of attack is negative in Figure 4.66 or positive in Figure 4.67. The quadratic term $-0.098w'|w'|$ from Equation 4.23 for the barebody Suboff is very similar in magnitude for the Suboff with sail.
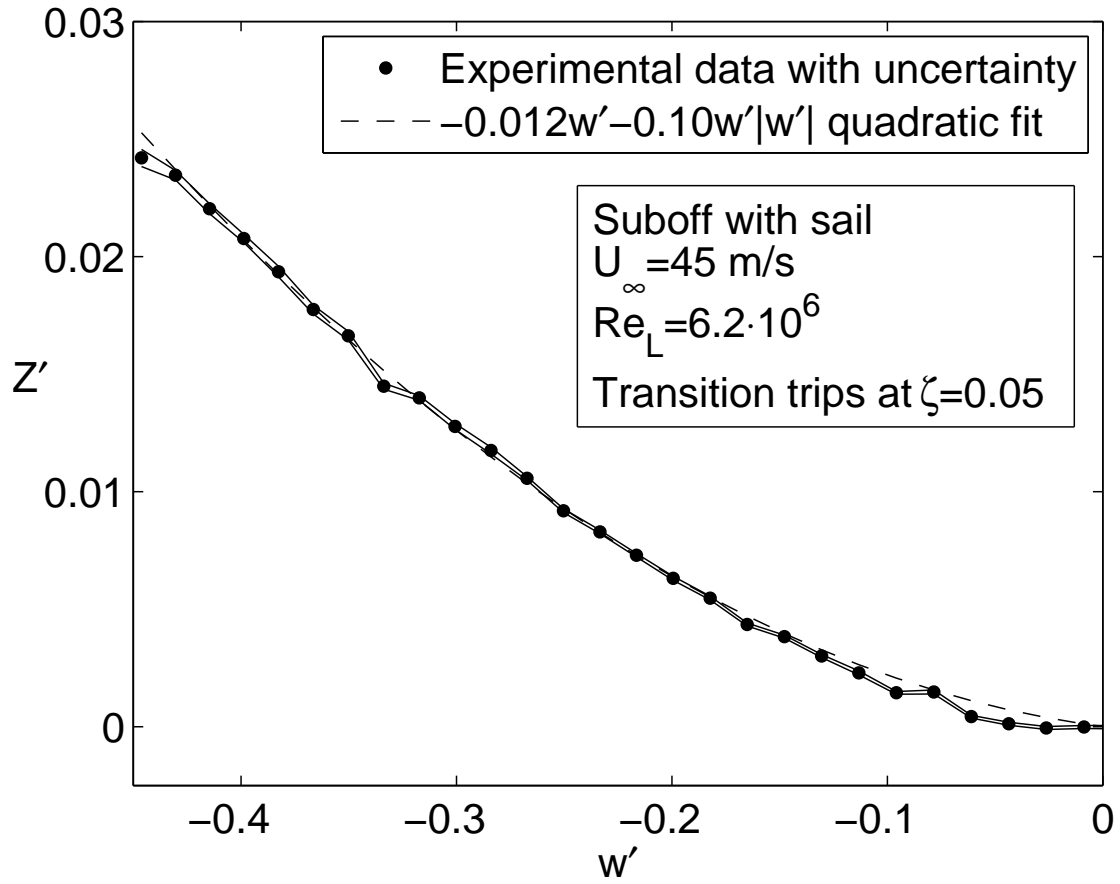
Figure 4.66: Quadratic fit to normal force
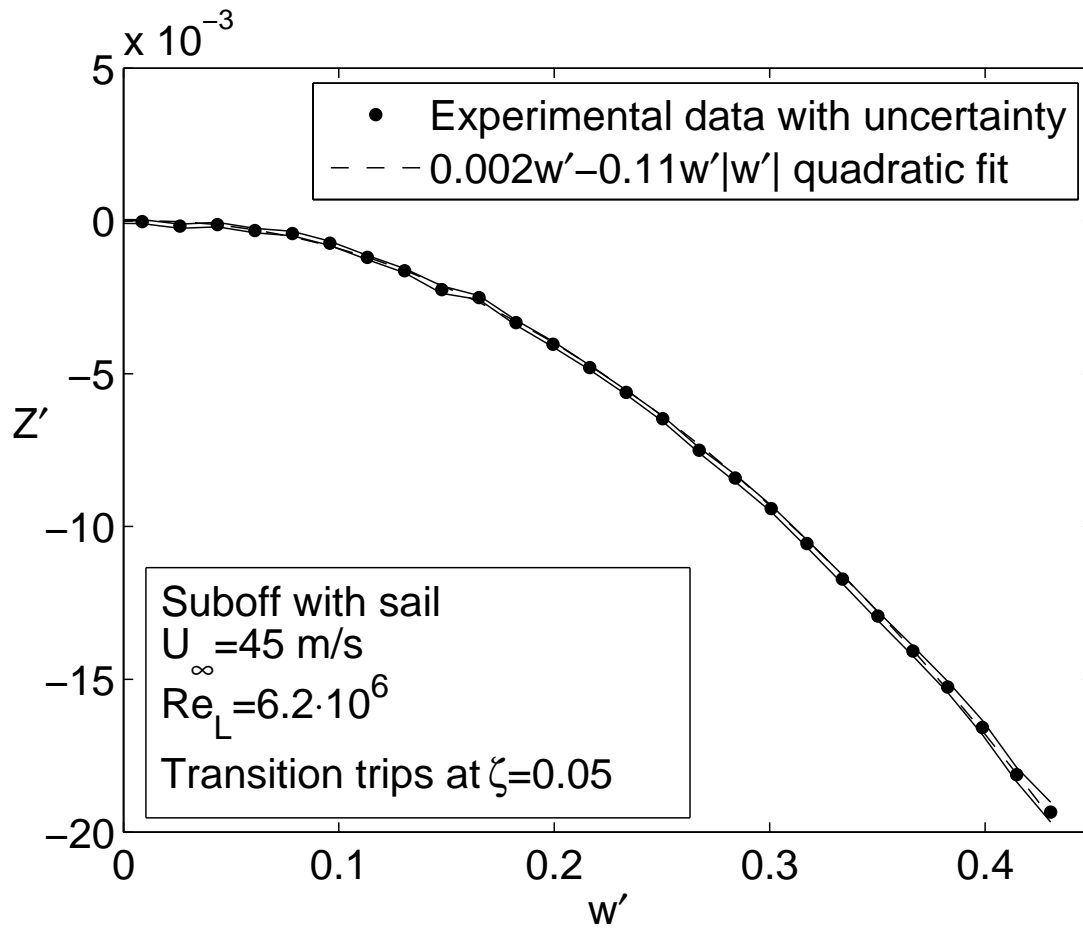
Figure 4.67: Quadratic fit to normal force

The pitching moment M'_w in Figure 4.68 is not different in the small angle linear range from the barebody Suboff case in Figure 4.63. It is, at the time of writing, unclear of exactly how to implement an analytical model extension to that of the barebody Suboff to also take into account the effects of the sail.
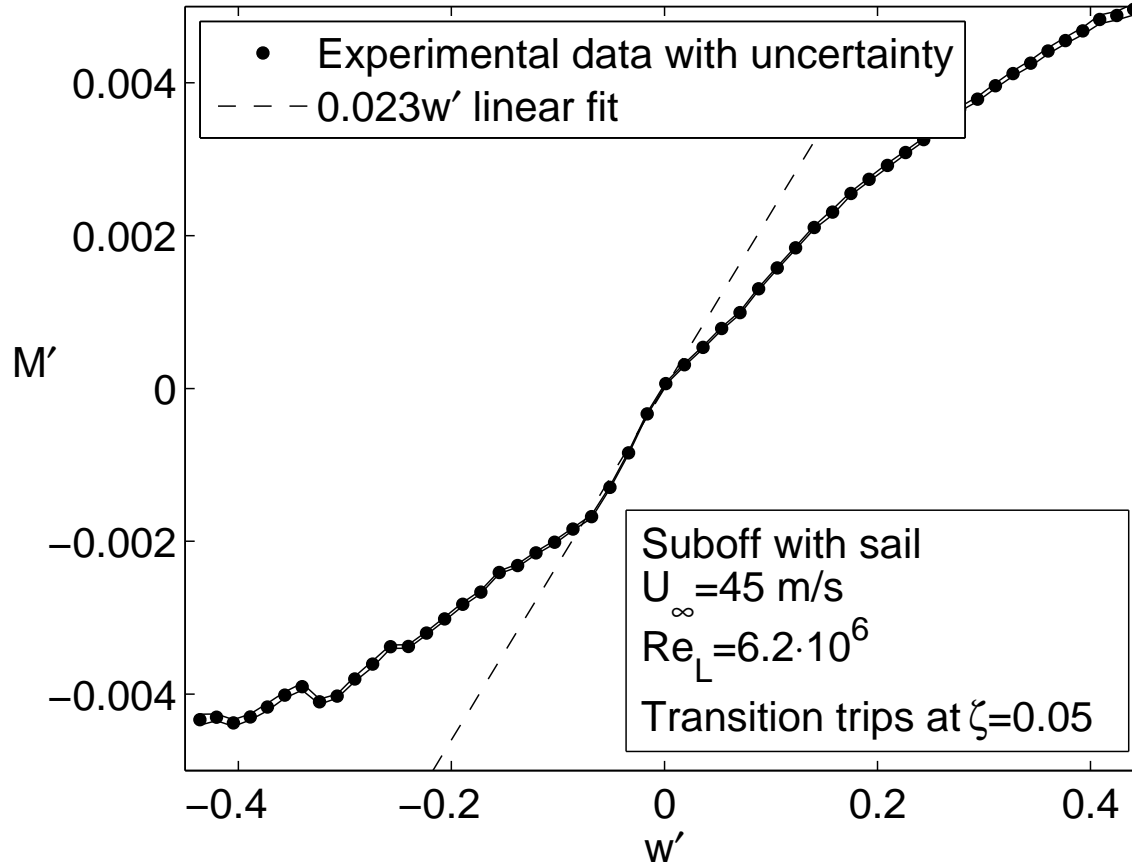
Figure 4.68: Linear fit to pitch moment

4.6 Fully appended Suboff steady data

4.6.1 Angle of Attack

The normal force Z' and pitch moment M' in Figure 4.69 and 4.70 behave like expected and similar as for both the Suboff with sail and ellipsoid cases. There is a slight asymmetry to the curve because of the sail induced horseshoe vortex.
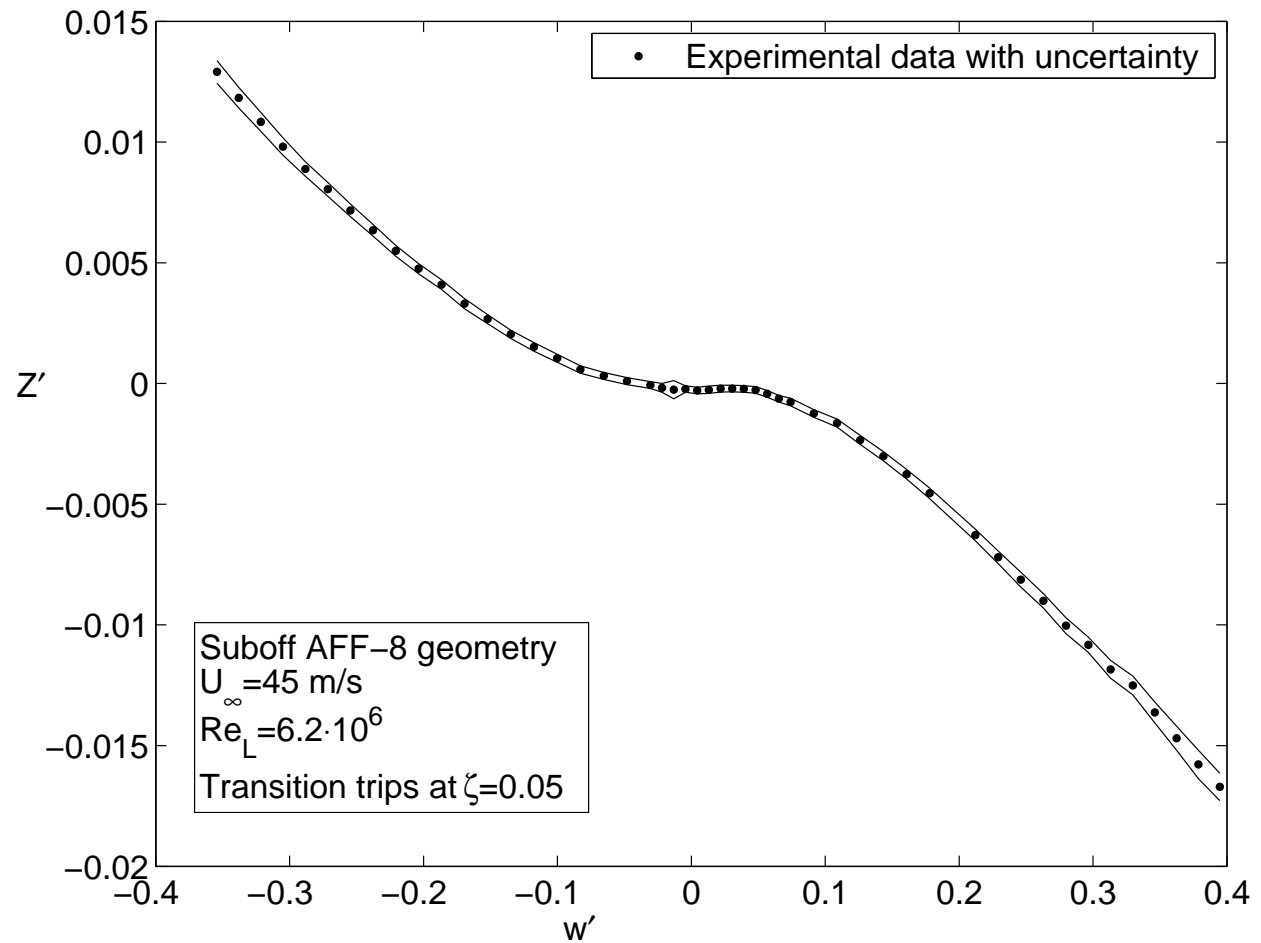
Figure 4.69: Fully appended Suboff Normal force vs. AoA
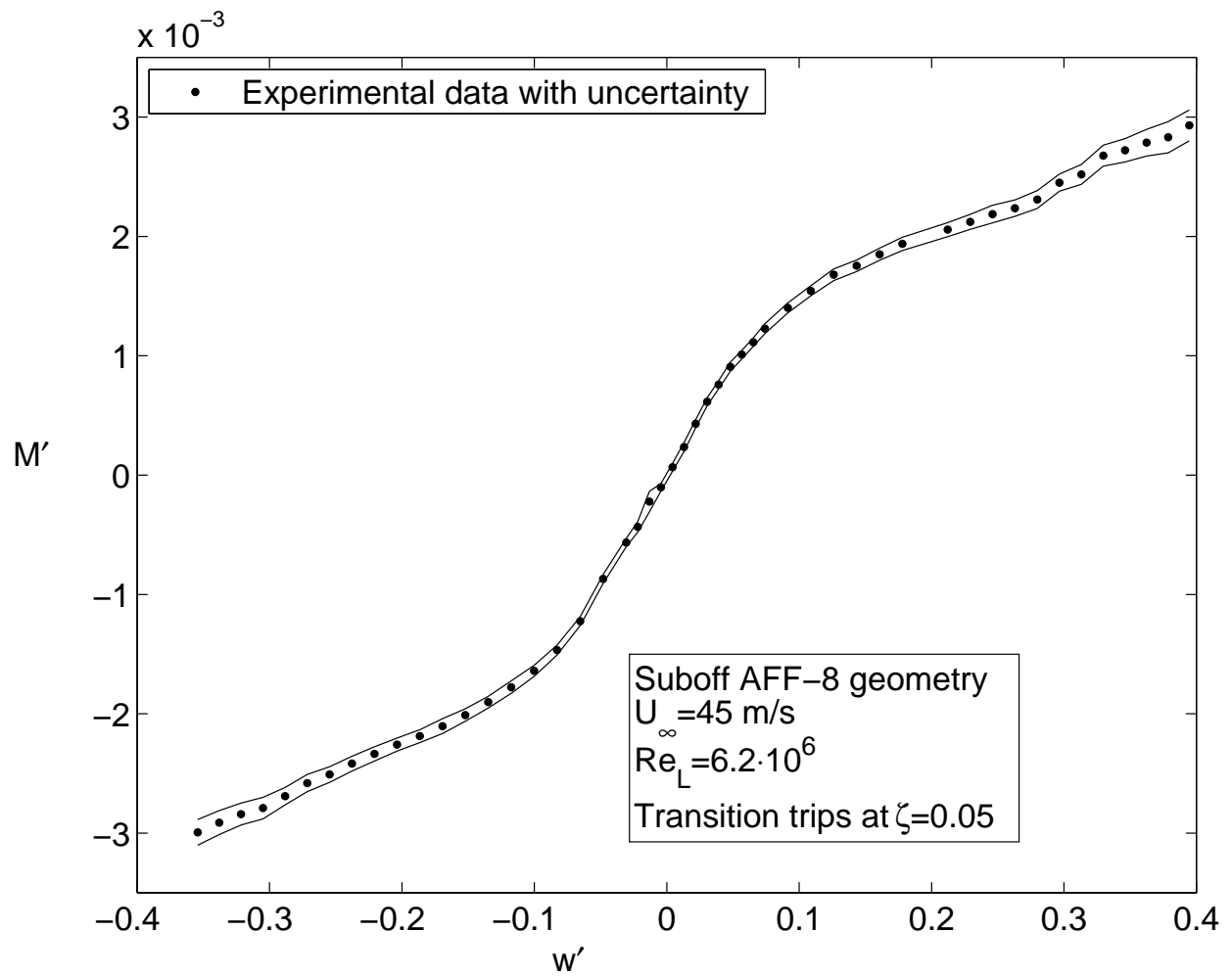
Figure 4.70: Fully appended Suboff Pitch moment vs. AoA

The out-of-plane forces and moments are very small on the order of 5% of the in-plane forces and moments in Figure 4.71, 4.72 and 4.73 indicating the model was properly aligned on the sting. For the same reason as for the Suboff case with sail only, it is unclear at the time of writing on how to incorporate the effects of the sail in the proposed analytical model for normal force Z' and pitch moment M'.
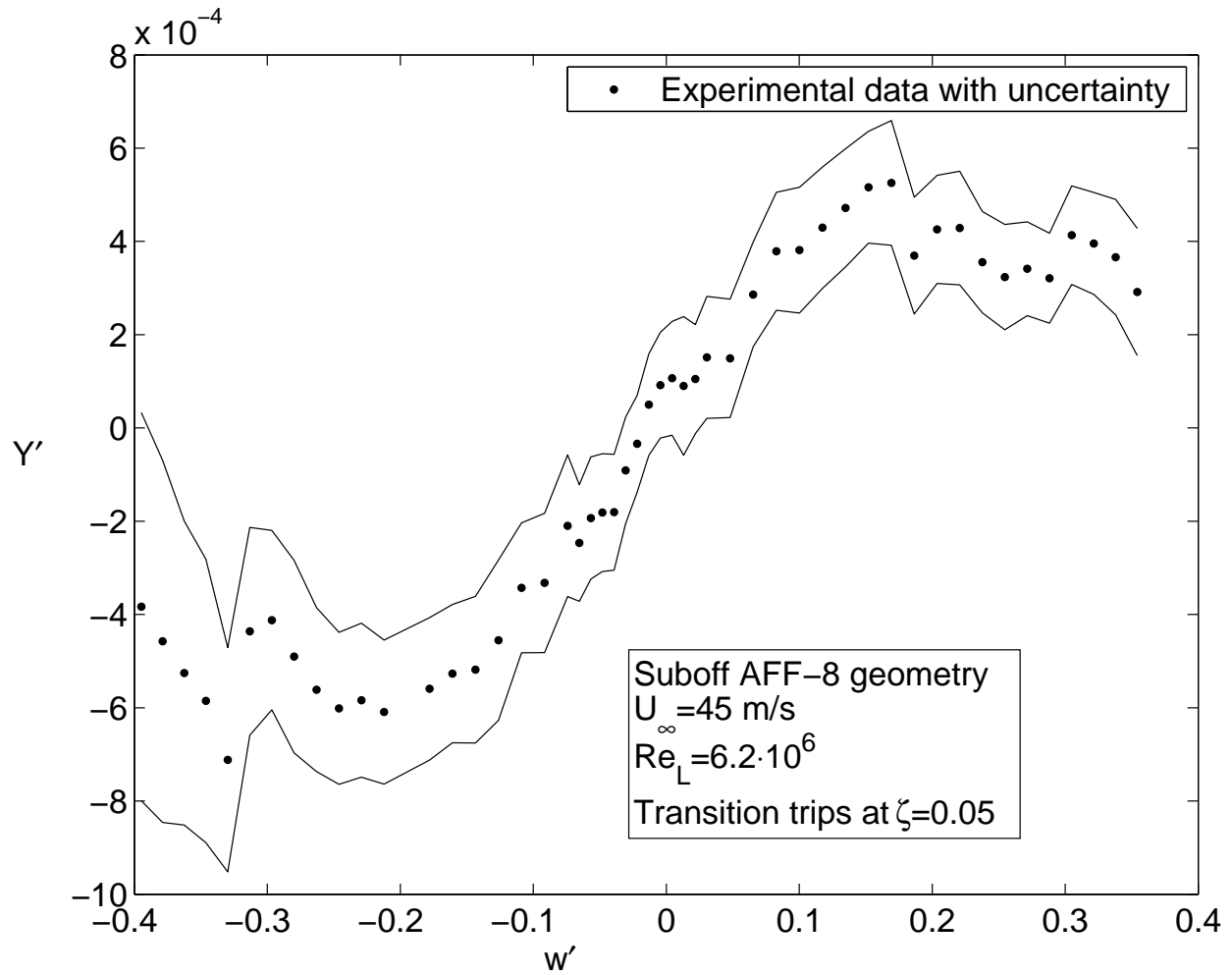
Figure 4.71: Fully appended Suboff side force vs. AoA
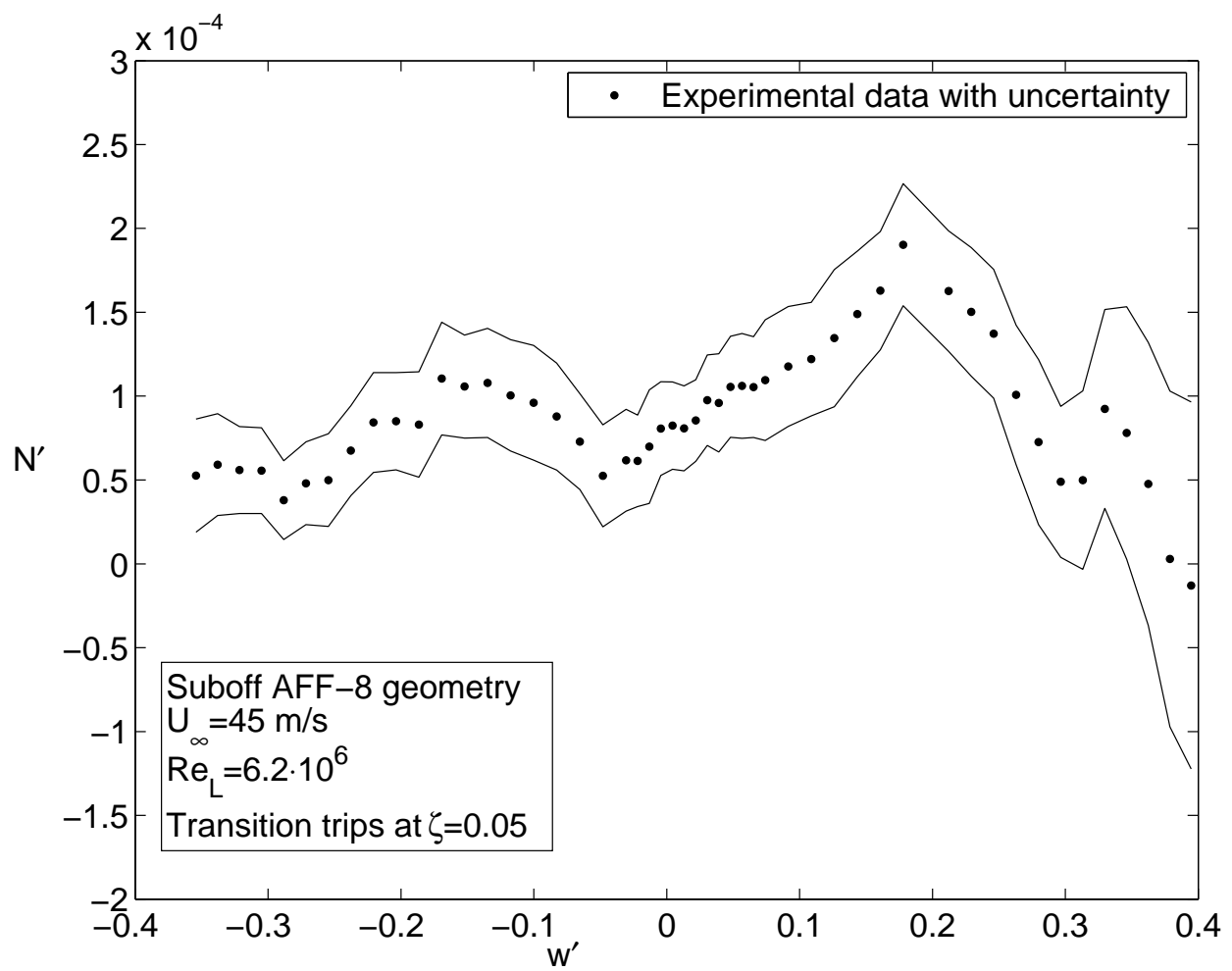
Figure 4.72: Fully appended Suboff Yaw moment vs. AoA
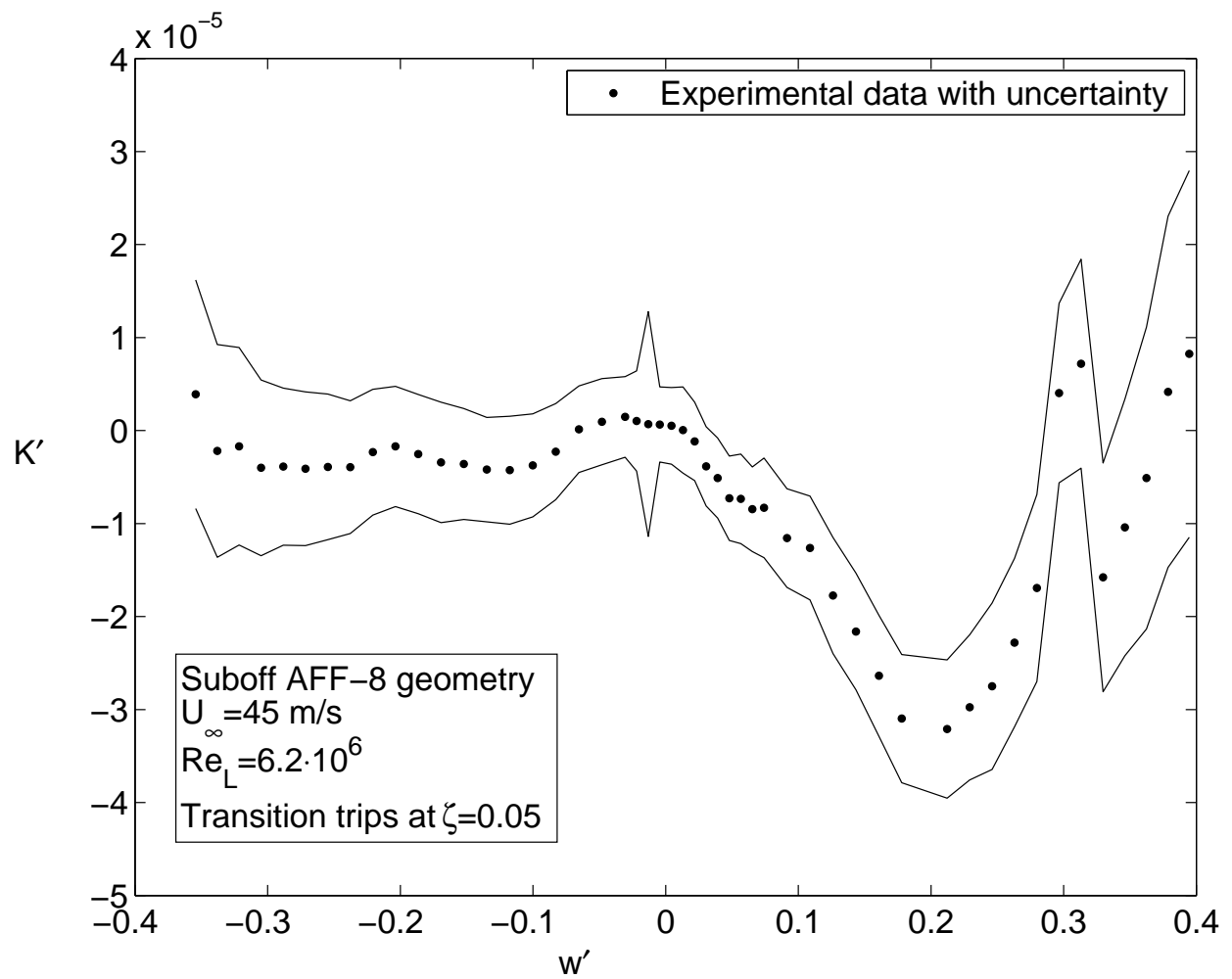
Figure 4.73: Fully appended Suboff Rolling moment vs. AoA

4.6.2 Sideslip

The side force Y' in sideslip in Figure 4.74 have small discontinuities at $|v'| \approx 0.2$.
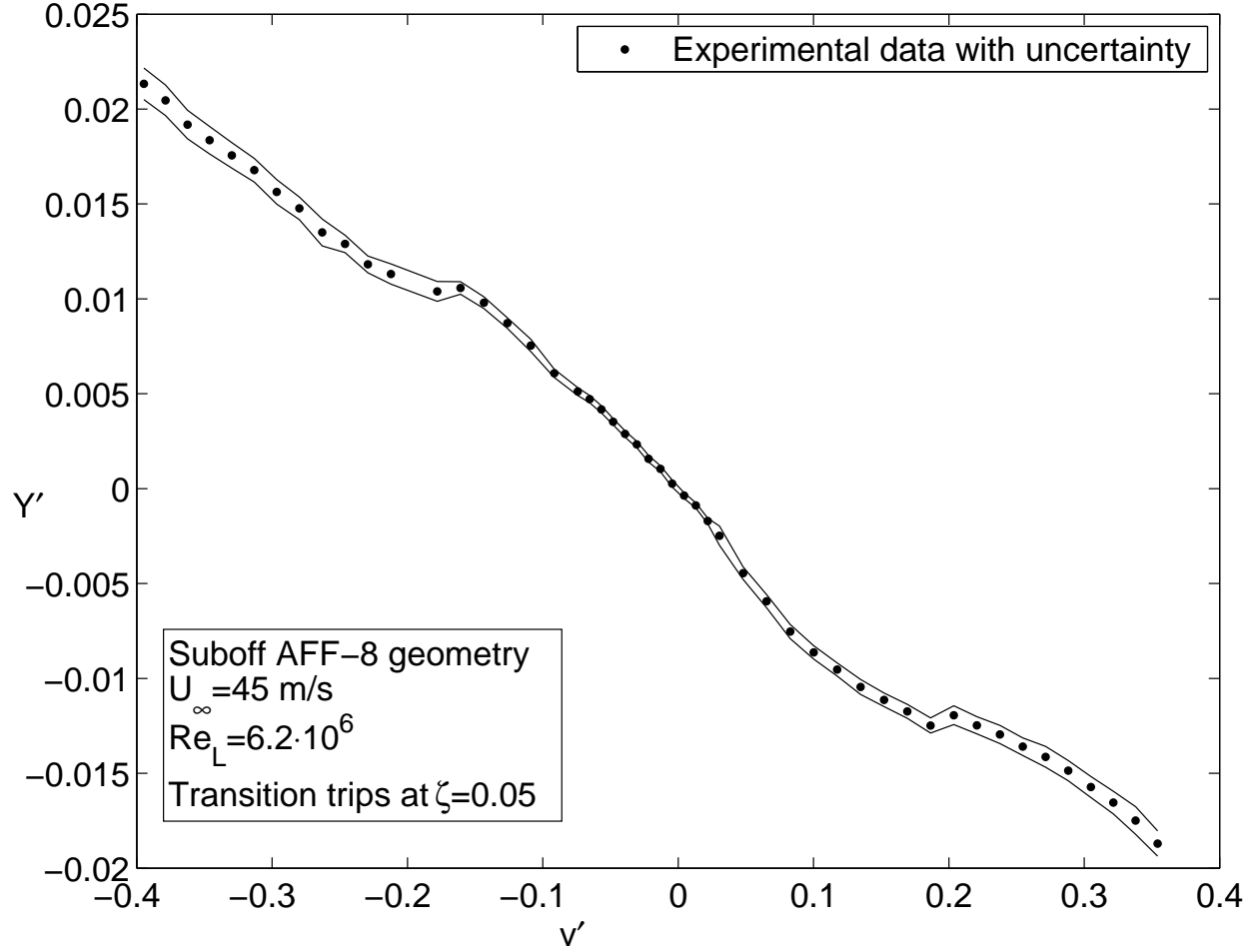
Figure 4.74: Fully appended Suboff Side force vs. sideslip

The yaw moment N' in sideslip in Figure 4.75 does not have any evidence of the discontinuities from Figure 4.74. The source of the small assymetry at $v' \approx 0.5$ is unknown. The model is symmetric in yaw and should produce a symmetric curve.
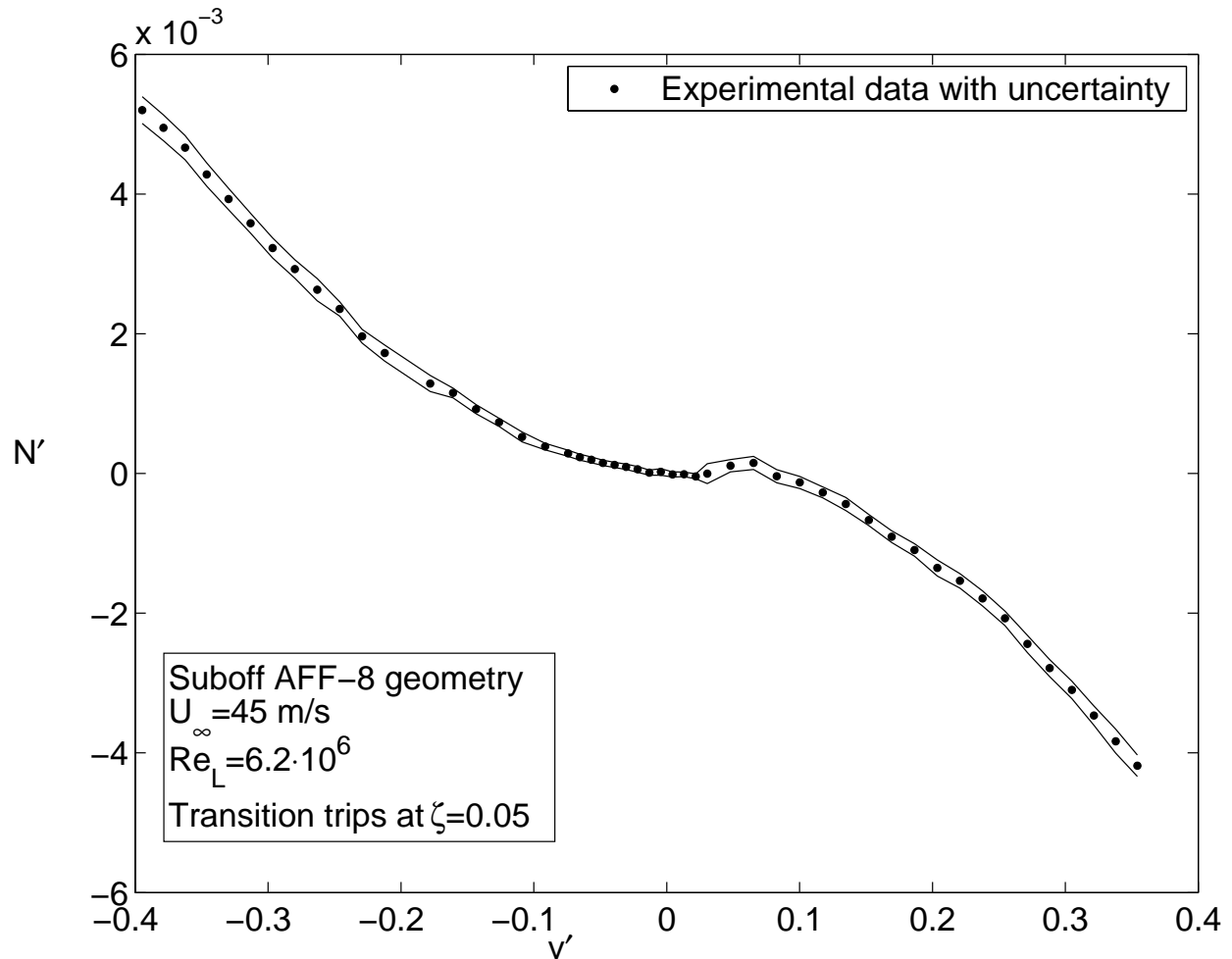
Figure 4.75: Fully appended Suboff Yaw moment vs. sideslip

The normal force Z' is positive for increasing sideslip, although the curve is not completely symmetric.
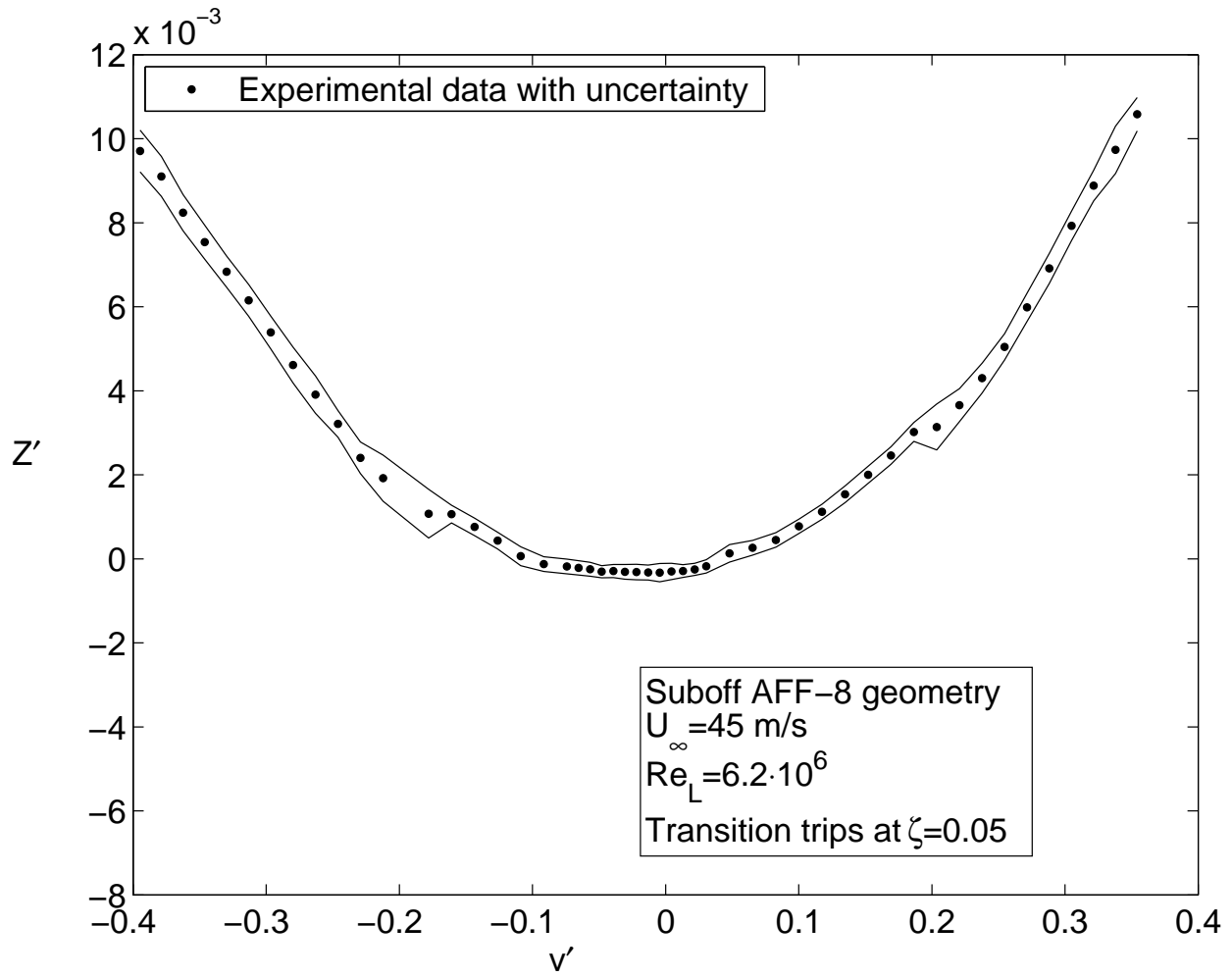
Figure 4.76: Fully appended Suboff Normal force vs. sideslip

The pitch moment M' is negative for small sideslip and increases to a positive value for larger sideslip. There curve is symmetric.
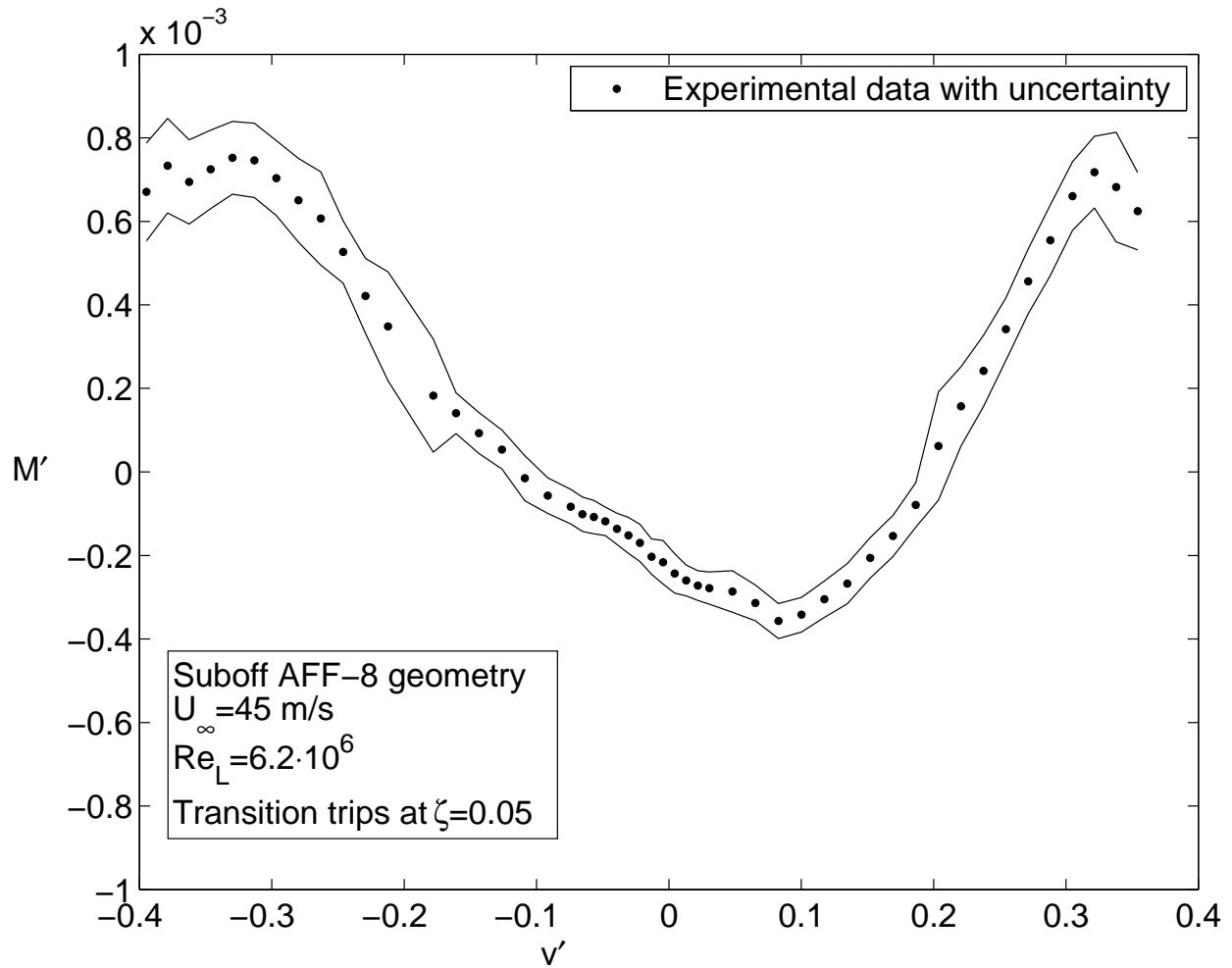
Figure 4.77: Fully appended Suboff Pitch moment vs. sideslip

The slope discontinuities that are evident in Figure 4.74 and to a larger extent in Figure 4.78 at $|v'| \approx 0.19$ are thought to come from the sail stalling at a too large sideslip angle. This is not evident in the reults by Roddy [68] although those tests were conducted at a $Re_L \approx 14 \cdot 10^6$. It is possible that the lower $Re_L \approx 6 \cdot 10^6$ this experiment was performed at would produce laminar separation on the sail suction side.
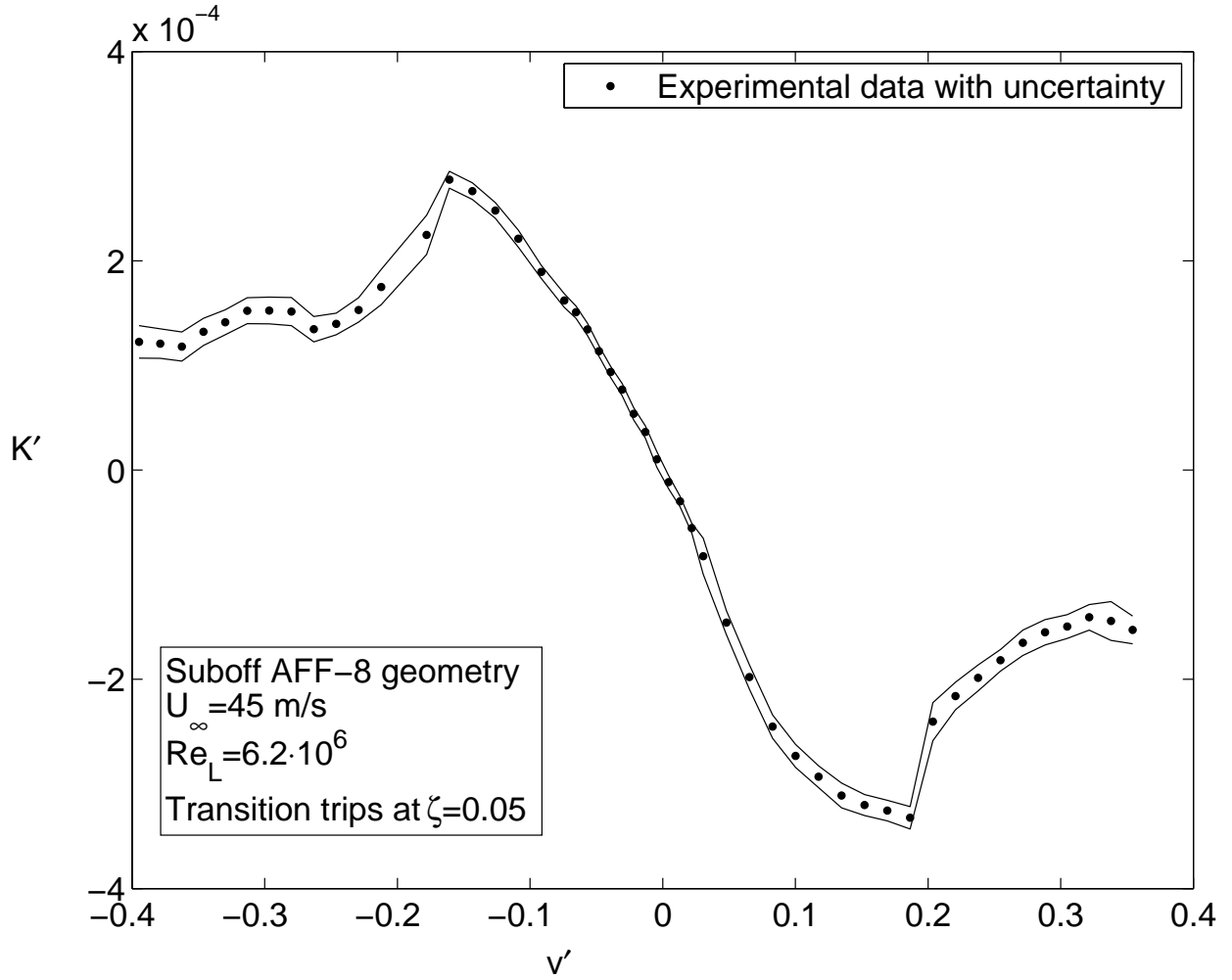
Figure 4.78: Fully appended Suboff Rolling moment vs. sideslip

The slight assymmetry in Figures 4.76 and 4.77 could be due to the not completely uniform freestream in the windtunnel, or if the model was not perfectly aligned on the sting.

132

Chapter 5

Conclusions

5.1 Experimental results

A low order functional form, based on flow physics, has been developed to better determine normal force and pitching moment, as well as side force and yaw moment, for a non-Body-of-Revolution ellipsoidal generic submarine shape, as well as for the Suboff submarine shape. The force and moment model equations take into the account that flow over the body stays attached for small angles of attack and/or sideslip and does not exhibit cross-flow separation. The normal- and side force as well as the pitching- and yawing moment coefficient derivatives are constant for small normalized heave- and sway velocities. At larger normalized heave- and sway velocities, the normal- and side forces are proportional to the quadratic term of the normalized heave- and sway velocities. The quadratic order comes from the almost century-old assumption that the cross-flow component of the freestream velocity can be observed as the drag over an infinite cylinder in freestream. The quadratic order has been verified through experiments as well as CFD and semi-empirical methods, even though the coefficients themselves have not yet been shown to be reliably predicted.

133

For the Ellipsoid body, the center of pressure for the cross-flow separation second order contribution to the forces and moments is at a fixed location. The analytical model predictions to the forces and moments fall within low uncertainty experimental measurements. The center of pressure for the cross-flow contribution on the Suboff model is not at a fixed location.

One case of a pitch angle sweep with a fixed roll angle was performed to obtain data at a combination of heave-and sway velocities. Unfortunately, this data is insufficient for obtaining analytical functions with coefficients for cross-dependency of normalized velocities.

Low uncertainty force and moment data were acquired and analyzed for unsteady ramp maneuvers and have been performed with different initial conditions for the ellipsoid geometry. The unsteady force and moment data have been found to either lead or lag the data at a fixed angle of attack during the maneuver. Since rotating arm data do not exist for the combined envelope of angle of attack and rotational speed, analytical predictions from time-dependent states against unsteady data cannot be performed.

5.2   Equipment

Other constrained-motion equipment produce oscillatory motions where the model is made to continuously vary the states, and all higher order derivatives of the states. Since the DyP-PiR is a computer controlled apparatus that enables a model to follow a preprogrammed path of motion in a in tunnel test section, one can use the ability to perform investigations on how initial state affects the unsteady flow characteristics, unlike oscillatory motions that have no initial conditions.

When conducting dynamic tests with the DyPPiR, one cannot use the wind–on minus wind–off method as previously used by Granlund [41]. The reason for that is because the wind-off measurements include, not only model inertial measurements, but also aerodynamic inertial measurements. In this kind of process, one essentially includes the added-mass in the tare measurements, which is wrong. The correct procedure is to compute the vertical acceleration of the model and also the mass of the model when performing plunge-only maneuvers. For pitch-maneuvers, the angular acceleration as well as the model moment of inertia is needed.

Because of the overhaul of the actuators and servovalves as well as cleaning the fluid and installing finer filters, the entire hydraulic system of the DyPPiR is now believed to be free of mechanical faults and be able to operate like such for a prolonged time without wear.

5.3 Future work

It is not recommended that the unsteady data acquired prior to this dissertation be reprocessed with new filtering schemes. Improvements can be done, but at the expense of time and money such that the payoff will not be worth it. The limitations to better data lies in improving the hardware. Only after hardware improvements are efforts in improving the post-processing worth it.

Recommended future upgrades to the DyPPiR consist of mounting the 760-557A servo-valve from the D079-121A combination unit directly to the pitch actuator to achieve a more linear control throughout the entire operational envelope of the DyPPiR. Pump #3 with system pressure of 2200psi is also recommended to achieve faster valve response times and higher oscillation frequency, if there still are oscillations.

By attenuating the oscillations in the lower frequency range, one can analyze how, and if, the unsteady forces and moments exhibit transient leads and lags versus quasi-steady forces and moments during different parts of a maneuver.

Chapter 6

Acknowledgements

Appendix A

Model Equations

A.1 Suboff

$$R = 0.13335m$$

$$L = 2.2369272m$$

<u>$0 \leq x[m] \leq 0.5334$</u>

$$r(x) = R\left[1 + 0.054x^2\left(\frac{x}{0.5334} - 1\right)^3 - (1 + 0.0393x)\left(\frac{x}{0.5334} - 1\right)^4\right]^{\frac{1}{2.1}}$$

<u>$0.5334 \leq x[m] \leq 1.7035272$</u>

$$r(x) = R$$

$$r_h = 0.1175$$

$$K_0 = 10$$

$$K_1 = 44.6244$$

$$\xi = \frac{2.2369272 - x}{0.5334}$$

$$\underline{1.7035272 \leq x[m] \leq 2.2369272}$$

$$
\begin{aligned}
r(x) = \ & R \left[r_h^2 + r_h K_0 \xi^2 \right. \cdot \\
& + \left(20 - 20r_h^2 - 4r_h K_0 - \frac{1}{3} K_1 \right) \xi^3 \\
& + \left(-45 + 45r_h^2 + 6r_h K_0 + K_1 \right) \xi^4 \\
& + \left(36 - 36r_h^2 - 4r_h K_0 - K_1 \right) \xi^5 \\
& + \left. \left(-10 + 10r_h^2 + r_h K_0 + \frac{1}{3} K_1 \right) \xi^6 \right]^{\frac{1}{2}}
\end{aligned}
$$

A.2 Ellipsoid

$$a = 0.4$$

$$b = 0.2$$

$$c = 0.1155$$

$$\epsilon = \sqrt{1 - \left(\frac{c}{b} \right)^2} = 0.8164$$

$\underline{0 \leq x[m] \leq 0.4}$

$$
\begin{aligned}
y' &= b\sqrt{1 - \left(\frac{x}{a} - 1\right)^2} \\
r &= \frac{y'(1 - \epsilon^2)}{1 + \epsilon cos\theta} \\
y &= rcos\theta \\
z &= rsin\theta
\end{aligned}
$$

$\underline{0.4 \leq x[m] \leq 1.2}$

$$
\begin{aligned}
r &= b \\
y &= rcos\theta \\
z &= rsin\theta
\end{aligned}
$$

$\underline{1.2 \leq x[m] \leq 1.6}$

$$
\begin{aligned}
y' &= b\sqrt{1 - \left(\frac{x - 1.2}{a}\right)^2} \\
r &= \frac{y'(1 - \epsilon^2)}{1 + \epsilon cos\theta} \\
y &= rcos\theta \\
z &= rsin\theta
\end{aligned}
$$

Appendix B

Loadcell calibration data

All loadcells calibrated with a gain of 1000. Numbered loadcells are made of aluminum, those with letters are of steel.

B.1 Loadcell 1

$$V_1 = \begin{bmatrix} 0.0914 & 0.0011 \\ 0.0021 & 0.0879 \end{bmatrix} F_1$$

$$
\begin{aligned}
Var\left[a_{1,yy}\right] &= 3.5e-6 \\
Var\left[a_{1,yz}\right] &= 8.5e-8 \\
Var\left[a_{1,zy}\right] &= 7.3e-8 \\
Var\left[a_{1,zz}\right] &= 2.2e-6
\end{aligned}
$$

$$F_1 = \begin{bmatrix} 11.062 & -0.5412 \\ -0.264 & 11.3895 \end{bmatrix} V_1$$

$$
\begin{aligned}
Var\left[F_{1,y}\right] &= 0.0537 * V_{1,y}^2 + 0.0013 * V_{1,z}^2 + 112.37 * Var\left[V_{1,y}\right] \\
Var\left[F_{1,z}\right] &= 0.0012 * V_{1,y}1^2 + 0.0369 * V_{1,z}^2 + 129.72 * Var\left[V_{1,z}\right]
\end{aligned}
$$

B.2   Loadcell 2

$$V_2 = \begin{bmatrix} 0.0860 & 0.00473 \\ 0.00264 & 0.08546 \end{bmatrix} F_2$$

$$
\begin{aligned}
Var\left[a_{2,yy}\right] &= 7.1e-6 \\
Var\left[a_{2,yz}\right] &= 6.6e-8 \\
Var\left[a_{2,zy}\right] &= 6.2e-8 \\
Var\left[a_{2,zz}\right] &= 4.8e-6
\end{aligned}
$$

$$F_2 = \begin{bmatrix} 11.6477 & -0.6447 \\ -0.3598 & 11.7213 \end{bmatrix} V_2$$

$$
\begin{aligned}
Var\left[F_{2,y}\right] &= 0.123 * V_{2,y}^2 + 0.0122 * V_{2,z}^2 + 123.67 * Var\left[V_{2,y}\right] \\
Var\left[F_{2,z}\right] &= 0.0011 * V_{2,y}^2 + 0.090 * V_{2,z}^2 + 137.39 * Var\left[V_{2,z}\right]
\end{aligned}
$$

B.3   Loadcell 3

$$V_3 = \begin{bmatrix} 0.0908 & -0.0023 \\ -0.0044 & 0.0864 \end{bmatrix} F_3$$

$$
\begin{aligned}
Var\left[a_{3,yy}\right] &= 7.1e-6 \\
Var\left[a_{3,yz}\right] &= 6.6e-8 \\
Var\left[a_{3,zy}\right] &= 6.2e-8 \\
Var\left[a_{3,zz}\right] &= 4.8e-6
\end{aligned}
$$

$$F_3 = \begin{bmatrix} 11.0325 & 0.2928 \\ 0.5649 & 11.59 \end{bmatrix} V_3$$

$$
\begin{aligned}
Var\left[F_{3,y}\right] &= 0.104 * V_{3,y}^2 + 0.0011 * V_{3,z}^2 + 121.72 * Var\left[V_{3,z}\right] \\
Var\left[F_{3,z}\right] &= 0.001 * V_{3,y}^2 + 0.0861 * V_{3,z}^2 + 134.33 * Var\left[V_{3,z}\right]
\end{aligned}
$$

B.4   Loadcell 4

$$V_4 = \begin{bmatrix} 0.0918 & 0.0044 \\ 0.0022 & 0.0852 \end{bmatrix} F_4$$

$$
\begin{aligned}
Var\,[a_{4,yy}] &= 4.3e-6 \\
Var\,[a_{4,yz}] &= 7.0e-8 \\
Var\,[a_{4,zy}] &= 8.4e-8 \\
Var\,[a_{4,zz}] &= 4.5e-6
\end{aligned}
$$

$$F_4 = \begin{bmatrix} 10.9067 & -0.5633 \\ -0.2817 & 11.721 \end{bmatrix} V_4$$

$$
\begin{aligned}
Var\,[F_{4,y}] &= 0.0605 * V_{4,y}^2 + 0.0114 * V_{4,z}^2 + 118.96 * Var\,[V_{4,y}] \\
Var\,[F_{4,z}] &= 0.0014 * V_{4,y}^2 + 0.0854 * V_{4,z}^2 + 137.38 * Var\,[V_{4,z}]
\end{aligned}
$$

B.5   Loadcell 5

$$V_5 = \begin{bmatrix} 0.0809 & 0.00331 \\ -0.00325 & 0.0797 \end{bmatrix} F_5$$

$$
\begin{aligned}
Var\,[a_{5,yy}] &= 1.6e-6 \\
Var\,[a_{5,yz}] &= 1.4e-6 \\
Var\,[a_{5,zy}] &= 6.3e-7 \\
Var\,[a_{5,zz}] &= 8.1e-7
\end{aligned}
$$

$$F_5 = \begin{bmatrix} 12.304 & -0.50125 \\ 0.5032 & 12.5262 \end{bmatrix} V_5$$

$$
\begin{aligned}
Var\,[F_{5,y}] &= 0.0373 * V_{5,y}^2 + 0.0337 * V_{5,z}^2 + 152.3 * Var\,[V_{5,y}1] \\
Var\,[F_{5,z}] &= 0.0152 * V_{5,y}^2 + 0.0201 * V_{5,z}^2 + 156.9 * Var\,[V_{5,z}]
\end{aligned}
$$

B.6 Loadcell 6

$$V_6 = \begin{bmatrix} 0.0825 & 0.00543 \\ -0.0049 & 0.0806 \end{bmatrix} F_6$$

$$
\begin{aligned}
Var\left[a_{6,yy}\right] &= 1.2e - 6 \\
Var\left[a_{6,yz}\right] &= 4.6e - 8 \\
Var\left[a_{6,zy}\right] &= 1.2e - 8 \\
Var\left[a_{6,zz}\right] &= 3.6e - 6
\end{aligned}
$$

$$F_6 = \begin{bmatrix} 12.0729 & -0.8133 \\ 0.7340 & 12.3575 \end{bmatrix} V_6$$

$$
\begin{aligned}
Var\left[F_{6,y}\right] &= 0.026 * V_{6,y}^2 + 0.104 * V_{6,z}^2 + 145.75 * Var\left[V_{6,y}\right] \\
Var\left[F_{6,z}\right] &= 0.027 * V_{6,y}^2 + 0.085 * V_{6,z}^2 + 152.71 * Var\left[V_{6,z}\right]
\end{aligned}
$$

B.7 Loadcell 7

$$V_7 = \begin{bmatrix} 0.0749 & 0.0055 \\ 0.00463 & 0.0762 \end{bmatrix} F_7$$

$$
\begin{aligned}
Var\left[a_{7,yy}\right] &= 2.4e - 7 \\
Var\left[a_{7,zy}\right] &= 1.6e - 6 \\
Var\left[a_{7,zy}\right] &= 1.0e - 6 \\
Var\left[a_{7,zz}\right] &= 1.0e - 6
\end{aligned}
$$

$$F_7 = \begin{bmatrix} 13.411 & -0.968 \\ -0.8149 & 13.1822 \end{bmatrix} V_7$$

$$
\begin{aligned}
Var\left[F_{7,y}\right] &= 0.0076 * V_{7,y}^2 + 0.049 * V_{7,z}^2 + 179.85 * Var\left[V_{7,y}\right] \\
Var\left[F_{7,z}\right] &= 0.0307 * V_{7,y}^2 + 0.030 * V_{7,z}^2 + 173.77 * Var\left[V_{7,z}\right]
\end{aligned}
$$

B.8   Loadcell 8

$$V_8 = \begin{bmatrix} 0.0708 & 0.0052 \\ 0.0010 & 0.0783 \end{bmatrix} F_8$$

$$
\begin{aligned}
Var\,[a_{8,yy}] &= 3.6e-6 \\
Var\,[a_{8,yz}] &= 7.8e-8 \\
Var\,[a_{8,zy}] &= 1.4e-7 \\
Var\,[a_{8,zz}] &= 9.6e-6
\end{aligned}
$$

$$F_8 = \begin{bmatrix} 14.1376 & -0.9389 \\ -0.1806 & 12.7834 \end{bmatrix} V_8$$

$$
\begin{aligned}
Var\,[F_{8,y}] &= 0.143 * V_{8,y}^2 + 0.0253 * V_{8,z}^2 + 199.87 * Var\,[V_{8,y}] \\
Var\,[F_{8,z}] &= 0.046 * V_{8,y}^2 + 0.0255 * V_{8,z}^2 + 163.41 * Var\,[V_{8,z}]
\end{aligned}
$$

B.9   Loadcell A

$$V_A = \begin{bmatrix} 0.01419 & 0.000623 \\ 0.000768 & 0.01484 \end{bmatrix} F_A$$

$$
\begin{aligned}
Var\,[a_{8,yy}] &= 3.84e-9 \\
Var\,[a_{8,yz}] &= 8.8e-10 \\
Var\,[a_{8,zy}] &= 1.43e-9 \\
Var\,[a_{8,zz}] &= 1.67e-9
\end{aligned}
$$

$$F_A = \begin{bmatrix} 67.2144 & -2.8217 \\ -3.4785 & 67.5315 \end{bmatrix} V_A$$

$$
\begin{aligned}
Var\,[F_{A,y}] &= 0.0777 * V_{A,y}^2 + 0.0180 * V_{A,z}^2 + 4518 * Var\,[V_{A,y}] \\
Var\,[F_{A,z}] &= 0.0292 * V_{A,y}^2 + 0.0344 * V_{A,z}^2 + 4560 * Var\,[V_{A,z}]
\end{aligned}
$$

B.10   Loadcell B

$$V_B = \begin{bmatrix} 0.01400 & 0.00235 \\ 0.000977 & 0.01408 \end{bmatrix} F_B$$

$$
\begin{aligned}
Var\left[a_{B,yy}\right] &= 3.55e-9 \\
Var\left[a_{B,yz}\right] &= 6.03e-9 \\
Var\left[a_{B,zy}\right] &= 5.01e-10 \\
Var\left[a_{B,zz}\right] &= 3.82e-9
\end{aligned}
$$

$$F_B = \begin{bmatrix} 72.2703 & -12.062 \\ -5.0148 & 71.8597 \end{bmatrix} V_B$$

$$
\begin{aligned}
Var\left[F_{B,y}\right] &= 0.0924*V_{B,y}^2 + 0.155*V_{B,z}^2 + 5223*Var\left[V_{B,y}\right] \\
Var\left[F_{B,z}\right] &= 0.0129*V_{B,y}^2 + 0.097*V_{B,z}^2 + 5164*Var\left[V_{B,z}\right]
\end{aligned}
$$

B.11   Loadcell C

$$V_C = \begin{bmatrix} 0.01327 & 0.000769 \\ -0.000824 & 0.01362 \end{bmatrix} F_C$$

$$
\begin{aligned}
Var\left[a_{C,yy}\right] &= 2.88e-9 \\
Var\left[a_{C,yz}\right] &= 6.07e-9 \\
Var\left[a_{C,zy}\right] &= 1.33e-9 \\
Var\left[a_{C,zz}\right] &= 1.69e-9
\end{aligned}
$$

$$F_C = \begin{bmatrix} 75.0947 & -4.2399 \\ 4.5432 & 73.1649 \end{bmatrix} V_C$$

$$
\begin{aligned}
Var\left[F_{C,y}\right] &= 0.0929*V_{C,y}^2 + 0.186*V_{C,z}^2 + 5639*Var\left[V_{C,y}\right] \\
Var\left[F_{C,z}\right] &= 0.0407*V_{C,y}^2 + 0.049*V_{C,z}^2 + 5353*Var\left[V_{C,z}\right]
\end{aligned}
$$

Appendix C

DyPPiR repairs

Granlund [41] observed problems with the equipment as early as 2001. During the data reduction process, large oscillations prevented the author in obtaining low uncertainty force- and moment data. Unsuccessful attempts were made to remove the oscillation with a notch filter in the post-processing of data, but the noise turned out to vary in frequency with time of the motion. Attempts were made to understand the nature of the non-linearities of the system via a Simulink [56] model of the entire DyPPiR system. It had to be aborted due to the magnitude and complexity of the problem in introducing non-linear modules every-where in the system and via either manually varying the constants, or automatic parameter identification.

In the spring of 2007, it was found that the hydraulic fluid of the DyPPiR had not been changed, nor were there any records of the filter cartridges in the system being changed since the assembly of the system in 1989 by Ahn [3]. A fluid analysis revealed a heavy contamina-tion of copper particles ranging in size from $1\mu m$ to $100\mu m$. The use of an external filtering pump did bring the contamination level down significantly, but still not down to ASTM

levels permitted for continuous servovalve operation. According to the servovalve manufacturer Moog, the 79-series and 760-series servovalves in use in the DyPPiR system must be operated with a hydraulic fluid conforming to ASTM 4406:99 14/11 [18]. Because of the very elevated particle content in the fluid for a long time, wear on the servovalves was suspected and confirmed. All servovalves were subsequently overhauled by Moog. Only after several cycles of external filtering and repeated sludge removal from the hydraulic fluid reservior tank is the particle content down to the long term operational limits. Unfortunately, after two wind tunnel entries with the DyPPiR, the particle levels were back up again. The particles are belived to originate from the water/oil heat exchanger, which is needed to keep the hydraulic fluid at a constant temperature. New hydraulic line filters (Pall HC9601FDP) [15] with finer filter ratings have been installed to minimize the problem.

During a wind tunnel entry in May 2007, another problem with the pitch circuit was discovered. With a 0.6m sting mounted and the DyPPiR commanded to a fixed position, the pitch actuator shaft could be rotated approximately 1° without any significant resistance. The angle resolver on the actuator shaft recorded the change, so the problem was understood to be internal in the actuator or servovalves. Despite several motions with all internal sensor parameters on the pitch circuit recorded, the faults could not be isolated to either the actuator or the servovalves. Both units were sent in to the respective manufacturer for evaluation and repairs.

A problem with a leaking weld was discovered in the pitch actuator allowing hydraulic fluid to pass through the vane between the chambers. This problem is also believed to have caused the large non-constant frequency oscillations in data reported by Granlund in 2002[41]. Together with the pitch actuator, the roll actuator was also sent in for overhaul due to excessive internal leakage causing burst return hoses.

The pitch servovalves were also discovered to have internal wear and clogged filters due to the contaminated fluid. Because of this, the roll and plunge servovalves were also overhauled. Because of the construction of the servovalve system, the contaminated fluid is in constant flow inside the 760-series valves, causing wear on the nozzles. The 79-series servovalves can be seen as hydraulic amplifiers, driven by the 760-series servovalves. As long as the actuator is in a fixed position, there is no flow across the 79-series valves and therefore much less chance of wear.

During an entry in October 2007, loose wires on the backplane connection to the DyP-PiR control cards caused the plunge actuator to shake violently and destroy a model. After the problems were rectified and testing continued, it was discovered that the DyPPiR was severely lacking in dynamic performance to the point of being unusable. 0.3s long programmed pitch ramp motions took seveal seconds to execute for the hydraulic actuators. The rubber bladders in the pressure accumulator tanks were replaced since they had been continuously pressurized to 2000psi despite instructions on depressurizing after 1 month of non-use. Another test showed that the hydraulic pumps were not producing the rated pressure of 3000psi. Pump 1 and 2 were both down to 1500 psi which was less than the pressure in the bladders. An inspection of the system by Salem Hydraulics indicated rapid wear towards catastrophic failure of pump 1 and 2. Pump 2 also had a cloth rag blocking the inlet port. All three pumps have been overhauled.

An investigation of the plunge servovalves indicate a problem with the middle servo and spool. During inspection by Salem Hydraulics, the valve body was found to be scored and the LVDT pin bent. After repair and installation, all the hydraulical parts are believed to function correctly. During a two week entry in August 2008, several problems with the

electronic servocontrol cards are found. The pitch position resolver card produces a very non-sinusoidal carrier signals due to negligent design of the custom made board. In addition, the Least- and Second Least Significant Bits of the ADC chip resolver are swapped and most certainly did not contribute to position stability. All these issues have been corrected.

After examination of the hydraulic valve position data during maneuvers, it was revealed that the power spool valve that directs fluid to the pitch actuator opens a maximum of 1.5% during a dynamic maneuver. This becomes a problem, since the valve flow is very linear with spool position, as in Figure C.1 - except at very close to dead center of the spool, as in Figure C.2 according to Moog [19]. The uncertainty bounds are 50% to 200% of nominal valve gain in the near-zero region.
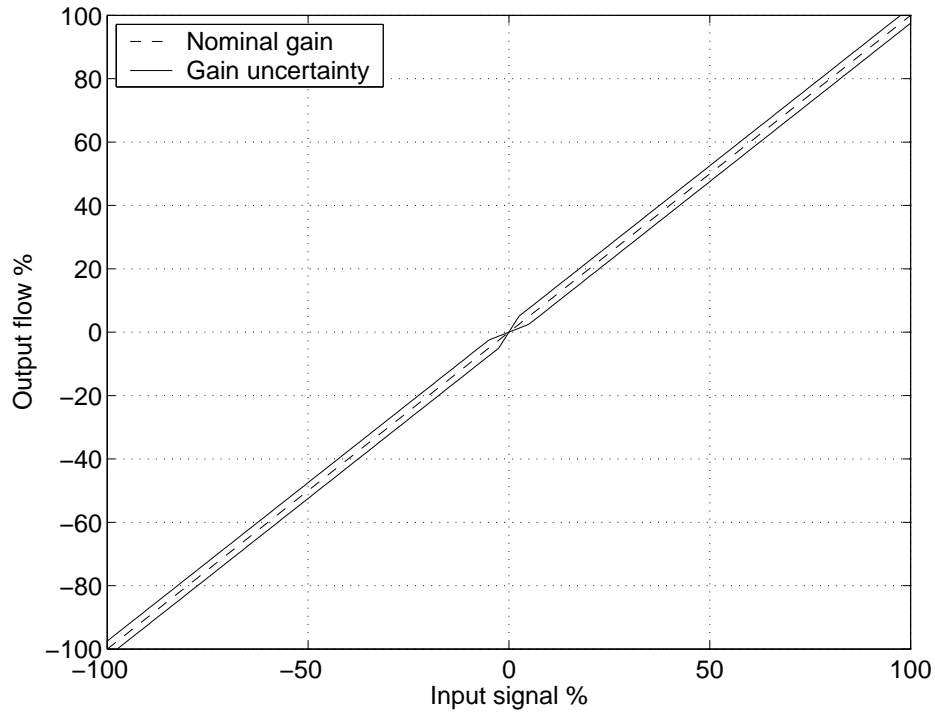
Figure C.1: Servovalve full range uncertainty characteristics

151
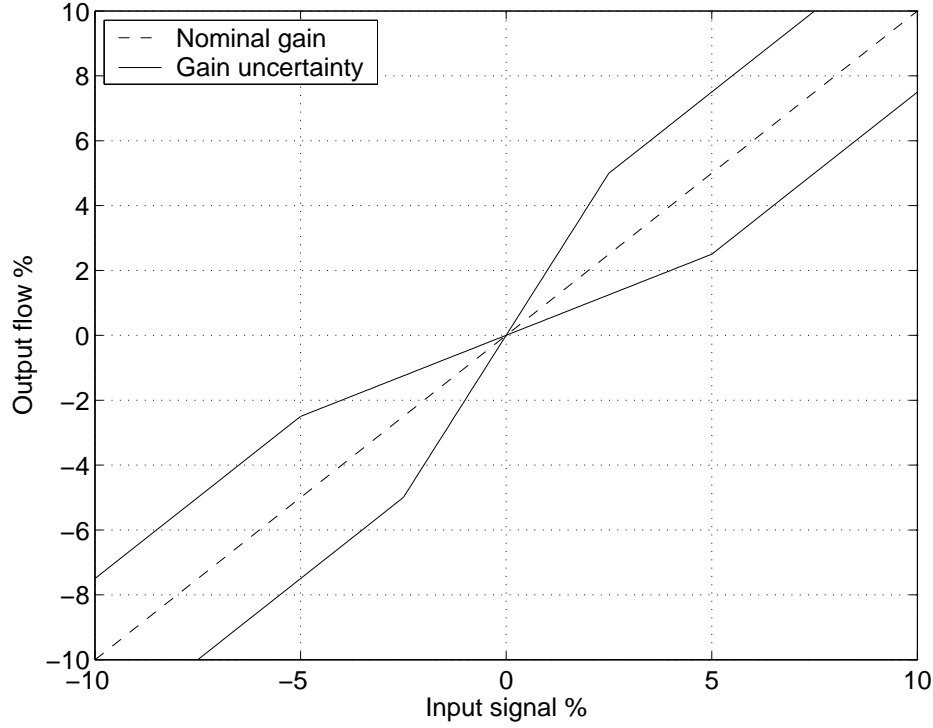
Figure C.2: Servovalve nonlinearity uncertainty region near zero

The last measure to compensate for this issue was to adjust the pressure on the hydraulic pump relief valves for the valves to open more. The pressure was set to 1400, 1800 and 2200 psi on pump #1, #2 and #3 respectively. In addition, the pressure accumulators were adjusted to 1100psi. Unfortunately, not even the lowest pressure produced a flowrate low enough for the pitch power valve to open enough to constantly be in the linear range. Lowering the pressure more would cause problems reliably controlling the plunge actuator. The remaining option is to use a smaller control valve for the pitch actuator.

The oscillations in data reported by Granlund [41] still remain, present only during maneuvers as low frequency oscillations. The oscillations increase in frequency with increasing maneuver motion velocity and have a lower frequency with lower hydraulic system pressure. With the pressure set at 2000psi, the second order 10Hz low pass filters in the loadcell am-

plifiers were capable of just barely remove enough noise to reduce the data. Unfortunately, with the aforementioned reduction in hydraulic system pressure to 1400psi, the oscillation frequency was lowered to a range where the loadcell amplifier filters modified to sixth order 5Hz low pass were again just barely capable of removing enough noise to extrat useful data.

The DyPPiR was designed to carry and maneuver a 50kg model and sting and reliably oscillate the model ±30° large angle amplitudes at 5Hz frequency. The pitch hydraulic circuit with a Moog D079-121A electrically controlled hydraulic primary servovalve, itself hydraulically operating a larger hydraulic powervalve that applies torque to a rotary hydraulic actuator. During the years the DyPPiR research evolved, the model mass was found to produce overwhelmingly large inertial noise to aerodynamic signals during dynamic testing. The mass of the sting and model has been reduced to a tenth of what was initially planned [3]. Since the hydraulically controlled available pitch torque never changed with the reduction in model mass, pitch sensitivity essentially increased tenfold with the present lightweight sting and models. The simplest and least expensive solution to reducing the sensitivity is to separate the D079-121A/760-557A combination servovalve unit and use the electrically controlled 760-557A servovalve directly mounted to the pitch actuator. According to Moog, at the rated pressure the 760-C557A produces one fifteenth of the flow rate at full valve openeing compared to with the whole D079-121A/760-557A combination unit. The control system will also be easier since the double, nested feedback loops - one outer, and one inner loop, will be reduced to a single feedback loop. Finally, since the valve spool is smaller with a smaller mass, the step response time will be decreased to 4ms from 12ms.

In addition to the aforementioned sensitivity modification and system simplification, the valve spool of the 760-servovalve will be oriented horizontally and not, as before, vertically and therefore not subjected to the plunge acceleration inertial forces.

References

[1] *Vectorworks Marine LLC.* http://www.vectorworksmarine.com, 2007.

[2] S. Ahn, , and R. Simpson. Cross Flow Separation on a Prolate Spheroid at Angle of Attack. *AIAA Paper 92-0428*, 1992.

[3] S. Ahn, K. Choi, , and R. Simpson. The Design and Development of a Dynamic Plunge-Pitch-Roll Model Mount. *AIAA Paper 89-0048*, 1989.

[4] A.J. Allen. Estimation of the Forces and Moments Acting on Inclined Bodies of Revolution of High Fineness Ratio. *NACA Research Memorandum A9I26*, 1949.

[5] A.J. Allen and E.W. Perkins. Characteristics of Flow over Inclined Bodies of Revolution. *NACA Research Memorandum A50L07*, 1951.

[6] Autodesk. *AutoCAD 2006.*

[7] R. Bensow. Large Eddy Simulation of the Flow Around a non-Body of Revolution Ellipsoidal Model. *AIAA Paper in progress*, 2009.

[8] Bondo. *Automotive Body Filler Product Data.* http://www.3m.com/US/auto_marine_aero/Bondo/catalog_item3aa7.html?itemNbr=268, 2005.

[9] Bondo. *UV Glazing and Spot Putty Product Data.* http://www.3m.com/US/auto_marine_aero/Bondo/catalog_item9cc2.html?itemNbr=757, 2005.

[10] G.H. Bryan. *Stability and Control.* Wiley, 1911.

[11] B. Chanetz and J. Délery. Experimental Analysis of Turbulent Separation on an Oblate Ellipsoid-Cylinder. *La Recherche Aerospatiale, English Ed.*, (3):59–77, 1988.

[12] M.S. Chang and L.P. Purtell. Three-dimensional Flow Separation and the Effect of Appendages. *16th Naval Hydrodynamics Symposium*, 1987.

[13] C. Chesnakas and R. Simpson. Detailed Investigation of the Three-Dimensional Cross-flow Separation About a 6:1 Prolate Spheroid. *AIAA Journal*, 35(6):990–999, 1997.

[14] K. Choi and R. Simpson. Some Mean Velocity, Turbulence and Unsteadiness Characteristics of the VPI& SU Stability Wind Tunnel. *VPI-AOE-161*, 1987.

[15] Pall Corporation. *Ultipor III Filter Elements Datasheet.* http://www.pall.com/datasheet_hydraulic_3103.asp, 2008.

[16] J. DeMoss. Drag Measurements on an Ellipsoidal Body. Master's thesis, Dept. of Aerospace and Ocean Engineering, Virginia Tech, Blacksburg, VA, 2007.

[17] Analog Devices. *Interactive Design Tools:Active Filter Synthesis.* http://www.analog.com/Analog_Root/static/techSupport/designTools/interactiveTools/filter/filter.html, 2008.

[18] Moog Industrial Controls Division. *79 Series Servovalves Technical Data.* http://www.moog.com/media/1/79series.pdf, 2007.

[19] Moog Industrial Controls Division. *Electrohydraulic Valve Applications.* http://www.moog.com/Media/1/technical.pdf, 2008.

[20] Dupli-Color. *Premium Filler Primer.* http://www.duplicolor.com/products/premium.html, 2005.

[21] L. Ericsson. Prediction of Slender Body Coning Characteristics. *AIAA Journal of Spacecraft and Rockets*, 28(1):43–49, 1991.

[22] N. Alin et.al. Large Eddy Simulation of the Transient Flow around a Submarine during Maneuver. *AIAA Paper 07-1454*, 2007.

[23] B. Etkin. *Dynamics of Atmospheric Flight*. Wiley, 1972.

[24] Y. Fan and F. Lutze. Identification of an Unsteady Aerodynamic Model at High Angles of Attack. *AIAA Paper 96-2407*, 1996.

[25] Y. Fan and F. Lutze. Unsteady Aerodynamic Tests and Data Reductions Using Digital Signal Processing Approach. *AIAA Paper 98-4454*, 1998.

[26] J. Feldman. DNTSRDC Revised Standard Submarine Equations of Motion. *DNTSRDC/SPD-0393-09*, 1979.

[27] J. Feldman. Straightline and Rotating Arm Captive-Model Experiments to Investigate the Stability and Control Characteristics of Submarines and Other Submerged Vehicles. *DTRC/SHD-0393-20*, 1979.

[28] J. Fussell and R. Simpson. Laminar Boundary Layer Calculations on a Submarine Body, Sail, and Stern Appendages, Using Integral Boundary Layer Equations. *VPI-AOE-303*, 2000.

[29] M. Gertler and G. Hagen. Standard Equations of Motion for Submarine Simulation. *NSRDC SR 0090101*, 1967.

[30] Fibre Glast. *3K, 2x2 Twill Weave Carbon Fiber Fabric Product Data*. http://www.fibreglast.com/documents/193.pdf, 2005.

[31] Fibre Glast. *4 Oz/Sq Yd. Fiberglass Surfacing Fabric Product Data.* http://www.fibreglast.com/documents/157.pdf, 2005.

[32] Fibre Glast. *Breather and Bleeder Cloth Product Data.* http://www.fibreglast.com/documents/180.pdf, 2005.

[33] Fibre Glast. *Epoxy Surface Coat Product Data.* http://www.fibreglast.com/documents/477.pdf, 2005.

[34] Fibre Glast. *Glass Microspheres Product Data.* http://www.fibreglast.com/documents/106.pdf, 2005.

[35] Fibre Glast. *Modeling Clay Product Data.* http://www.fibreglast.com/documents/252.pdf, 2005.

[36] Fibre Glast. *Nylon Release Film Product Data.* http://www.fibreglast.com/documents/182.pdf, 2005.

[37] Fibre Glast. *Polyethylene Bagging Film Product Data.* http://www.fibreglast.com/documents/178.pdf, 2005.

[38] Fibre Glast. *PVA Release Film Product Data.* http://www.fibreglast.com/documents/105.pdf, 2005.

[39] Fibre Glast. *Sealant Tape Product Data.* http://www.fibreglast.com/documents/181.pdf, 2005.

[40] M. Goman and A. Khrabrov. State-Space Representation of Aerodynamic Characteristics at High Angles of Attack. *AIAA Journal of Aircraft*, 31(5):1109–1115, 1994.

[41] K. Granlund. Methods for Obtaining Unsteady Force and Moment Data on a Submarine using the DyPPiR. Master's thesis, Dept. of Aeronautics , Royal Institute of Technology, Stockholm, Sweden, 2002.

[42] K. Granlund and R. Simpson. Modeling Unsteady Maneuvers of Slender Bodies. *AIAA Paper 07-6721*, 2004.

[43] K. Granlund and R. Simpson. Unsteady Force and Moment Data on a Maneuvering Undersea Vehicle. *AIAA Paper 04-0729*, 2004.

[44] D. Greenwell. Frequency Effects on Dynamic Stability Derivatives Obtained from Small-Amplitude Oscillatory Testing. *AIAA Journal of Aircraft*, 35(5):776–782, 1998.

[45] D. Greenwell. A Review of Unsteady Aerodynamic Modeling for Flight Dynamics of Maneuverable Aircraft. *AIAA Paper 04-5276*, 2004.

[46] Hexcel. *HexWeb HRH-10 Aramid Fiber/Phenolic Resin Honeycomb Product Data.* http://www.hexcel.com/Products/Downloads/HexwebHoneycombDataSheets, 2005.

[47] Hexcel. *HexWeb HRH-35 FlexCore Honeycomb Product Data.* http://www.hexcel.com/Products/Downloads/HexwebHoneycombDataSheets, 2005.

[48] J. P. Holman. *Experimental Methods for Engineers 7th edition.* McGraw Hill, 2000.

[49] S. Hosder and R. Simpson. An Experimental Investigation of Unsteady Flow Separation on a Maneuvering Axisymmetric Body. *Journal of Aircraft*, 44(4):1286–1295, 2007.

[50] National Instruments. *Labview.*

[51] Robert T. Jones. Effects on Sweepback on Boundary Layer and Separation. *NACA Technical Report 884*, 1947.

[52] K. Karamcheti. *Principles of Ideal-Fluid Aerodynamics.* Krieger, 1966.

[53] J. Larssen and W. Devenport. Acoustic Properties of the Virginia Tech Stability Wind Tunnel. *VPI-AOE-263*, 1999.

[54] F. Lutze. Experimental Determination of Pure Rotary Stability Derivatives using a Curved and Rolling Flow Wind Tunnel. *AIAA Paper 80-0309*, 1980.

[55] K. Makovec. The Use of PMARC for Pressure Coefficient and Vorticity Calculations on 688 and DARPA2 Submarines. *Internal document*, 1998.

[56] The Mathworks. *Simulink*.

[57] W.J. McCroskey. Some Current Research in Unsteady Fluid Dynamics. *Journal of Fluids Engineering*, 99:8–38, 1977.

[58] M. Mendenhall and D. Lesieutre. Prediction of Vortex Shedding from Circular and Noncircular Bodies in Subsonic Flow. *NASA Contractor Report 4037*, 1987.

[59] M. Mendenhall and S. Perkins. Prediction of Vortex-Induced Fluid Mechanics of Maneuvering Submarines. *AIAA Paper 93-0638*, 1993.

[60] Microsoft. *Windows Media Video 9 Series Codecs*. http://www.microsoft.com/windows/windowsmedia/forpros/codecs/video.aspx, 2009.

[61] M. Munk. The Aerodynamic Forces on Airship Hulls. *NACA Technical Report 184*, 1924.

[62] M. Munk. Remarks on the Pressure Distribution over the Surface of an Ellipsoid, Moving Translationally Through a Perfect Fluid. *NACA Technical Note 196*, 1924.

[63] Robert C. Nelson and Alain Pelletier. The Unsteady Aerodynamics of Slender Wings and Aircraft Undergoing Large Amplitude Maneuvers. *Progress in Aerospace Sciences*, 39:185–248, 2003.

[64] B. Pamadi, P. Murphy, V. Klein, and J. Brandon. Prediction of Unsteady Aerodynamic Coefficients at High Angles of Attack. *AIAA Paper 01-4077*, 2001.

[65] 3M Industrial Products. *Spray Adhesive 6070 for Styrofoam.* http://solutions.3m.com/wps/portal/3M/en_US/Products/ProdServ/, 2005.

[66] B. Racine and E. Paterson. CFD-Based Method for Simulation of Marine-Vehicle Maneuvering. *AIAA Paper 05-4904*, 2005.

[67] S.H. Rhee and T. Hino. Numerical Simulation of Unsteady Turbulent Flow Around Maneuvering Prolate Spheroid. *AIAA Journal*, 40(10):2017–2026, 2002.

[68] Robert F. Roddy. Investigation of the Stability and Control of the DARPA Suboff Model (DTRC Model 5470) from Captive-Model Experiments. *DTRC/SHD-1298-08*, 1990.

[69] R.P. Sallen and E.P. Key. A Practical Method of Designing Active Filters. *IRE Transactions on Circuit Theory*, pages 74–85, 1955.

[70] R. Schmitt and B. Chanetz. Experimental Investigation of Three-Dimensional Separation on an Ellipsoid-Cylinder Body at Incidence. *AIAA Paper 85-1686*, 1985.

[71] National Semiconductor. *LM741 Operational Amplifier Datasheet.* http://www.national.com/ds/LM/LM741.pdf, 2008.

[72] K. Sibilski. Problems of Manoeuvering at Post-Critical Angles of Attack – Continuation and Bifurcation Methods Approach. *AIAA Paper 03-0395*, 2003.

[73] R. Simpson. Some Experience with the Dynamic-Plunge-Pitch-Roll (dyppir) Mount in Unsteady Aeridynamics Research. *AIAA Paper 02-0170*, 2002.

[74] A.M. Skow. An Anlysis of the Su-27 Flight Demonstration at the 1989 Paris Airshow. *SAE Technical Paper 901001*, 1990.

[75] L.H. Smith and R.H. Nunn. Aerodynamic Characteristics of an Axisymmetric Body Undergoing a Uniform Pitching Motion. *AIAA Paper 75-0803*, 1975.

[76] West System. *105 Epoxy Resin and 206 Epoxy Hardener Product Data.* http://www.westsystem.com, 2005.

[77] Virginia Tech Department of Aerospace and Ocean Engineering. *Stability Tunnel.* http://www.aoe.vt.edu/research/facilities/stab/tunnel_descrip.php, 2009.

[78] M. Tobak. On the use of the Indicial Function Concept in the Analysis of Unsteady Motions of Wings and Wing-Tail Combinations. *NACA Report 1188*, 1954.

[79] M. Tobak and L. Schiff. Generalized Formulation of Nonlinear Pitch-Yaw-Roll Coupling. *AIAA Journal*, 13(3):323–332, 1975.

[80] R. Upson and W. Klikoff. Application of Practical Hydrodynamics to Airship Design. *NACA Techical Report 405*, 1931.

[81] Vishay. *Vishay 2310 Signal Conditioning Amplifier Product Data.* http://www.vishay.com/brands/measurements_group/guide/inst/2300/2310.htm, 2005.

[82] T. Wetzel and K. Granlund. *Dynamic Plunge Pitch Roll (DyPPiR) Model Mount Manual.* Internal report.

[83] T. Wetzel and R. Simpson. Unsteady Crossflow Separation Location Measurements on a Maneuvering 6:1 Prolate Spheroid. *AIAA Journal*, 36(11):2063–2071, 1998.

[84] T. Wetzel, R. Simpson, and C. Chesnakas. Measurement of Three-Dimensional Cross Flow Separation. *AIAA Journal*, 36(4):557–564, 1998.

[85] C. Whitfield. Steady and Unsteady Force and Moment Data on a DARPA2 Submarine. Master's thesis, Dept. of Aerospace and Ocean Engineering, Virginia Tech, Blacksburg, VA, 1999.

[86] K. Willet. Design, Development and Implementation of a Low Cost Slotted Wall Test Section and Race Car Model for use in Dynamic Wind Tunnel Testing(unfinished). Master's thesis, Department of Aerospace and Ocean Engineering, Virginia Tech, Blacksburg, VA.